An investigation of cavitation initiation and length of the two-phase region in a converging-diverging nozzle

by

Abdulmalik Mohammad Alkotami

B.S., Kansas State University, 2012
M.S., Kansas State University, 2014

AN ABSTRACT OF A DISSERTATION

submitted in partial fulfillment of the requirements for the degree

DOCTOR OF PHILOSOPHY

Alan Levin Department of Mechanical & Nuclear Engineering
Carl R. Ice College of Engineering

KANSAS STATE UNIVERSITY
Manhattan, Kansas

2022

Abstract

A traditional refrigeration cycle has four main system components which are an evaporator, a compressor, a condenser, and an expansion valve. Different types of refrigerants are used in most cooling cycles. The main objective of this project was to develop a water-based cooling system by investigating the cavitation/flash phenomena for the flow through converging-diverging nozzles. Although, cavitation can be harmful in some engineering applications and causes damage to pumps, refrigeration expansion valves, and capillary tubes, on the other hand, it can be managed and used in a beneficial way. Cavitation in a flowing fluid can cause a reduction in temperature, which can result in energy being absorbed and hence, demonstrating a cooling potential. Cavitation/flash can occur when the static pressure of the fluid falls below the vapor pressure, into a metastable liquid state. This phenomenon has been shown in previous experimental work to occur in water flowing through a converging-diverging nozzle, where the cross-sectional area is constricted at the throat causing the velocity to increase and the pressure to decrease below the saturation pressure.

The research presented in this dissertation is focused on developing a complete theoretical model and evaluation techniques to predict the results of the cavitation phenomena in a converging-diverging nozzle. The conservation equations and the laws of thermodynamics are presented to understand the fundamental thermodynamics phenomena and to develop predictive models relevant to the cavitation process. The developed models were used to predict pressure distributions, the onset of flash/cavitation, the condensation shock location, and the length of the two-phase region for water within a converging-diverging nozzle. The predicted results were shown to compare well with the previous experimental work; in particular, with the length of the two-phase region. The length of the two-phase region is defined as the distance from the flash inception point to the location where the condensation shock formed in the diverging section of the nozzle. The length of the two-phase region is also used as a measure for the heat absorption area in the nozzle. The larger the area of heat absorption, the higher the cooling potential is likely to be for the system. Experimental results using water have shown only small temperature drops due to a cavitation process in converging-diverging nozzles, mainly due to the physical properties of water. However,

the models developed should also apply to cavitation with other fluids. Hence, this analysis can form the basis for future evaluation and potential optimization of the nozzle geometry, and the identification of alternative fluids (properties), necessary to achieve maximum cooling potential for fluids flowing through converging-diverging nozzles.

An investigation of cavitation initiation and length of the two-phase region in a converging-diverging nozzle

by

Abdulmalik Mohammad Alkotami

B.S., Kansas State University, 2012
M.S., Kansas State University, 2014

A DISSERTATION

submitted in partial fulfillment of the requirements for the degree

DOCTOR OF PHILOSOPHY

Alan Levin Department of Mechanical & Nuclear Engineering
Carl R. Ice College of Engineering

KANSAS STATE UNIVERSITY
Manhattan, Kansas

2022

Approved by:

Major Professor
Dr. Mohammad Hosni

Copyright

Abstract

A traditional refrigeration cycle has four main system components which are an evaporator, a compressor, a condenser, and an expansion valve. Different types of refrigerants are used in most cooling cycles. The main objective of this project was to develop a water-based cooling system by investigating the cavitation/flash phenomena for the flow through converging-diverging nozzles. Although, cavitation can be harmful in some engineering applications and causes damage to pumps, refrigeration expansion valves, and capillary tubes, on the other hand, it can be managed and used in a beneficial way. Cavitation in a flowing fluid can cause a reduction in temperature, which can result in energy being absorbed and hence, demonstrating a cooling potential. Cavitation/flash can occur when the static pressure of the fluid falls below the vapor pressure, into a metastable liquid state. This phenomenon has been shown in previous experimental work to occur in water flowing through a converging-diverging nozzle, where the cross-sectional area is constricted at the throat causing the velocity to increase and the pressure to decrease below the saturation pressure.

The research presented in this dissertation is focused on developing a complete theoretical model and evaluation techniques to predict the results of the cavitation phenomena in a converging-diverging nozzle. The conservation equations and the laws of thermodynamics are presented to understand the fundamental thermodynamics phenomena and to develop predictive models relevant to the cavitation process. The developed models were used to predict pressure distributions, the onset of flash/cavitation, the condensation shock location, and the length of the two-phase region for water within a converging-diverging nozzle. The predicted results were shown to compare well with the previous experimental work; in particular, with the length of the two-phase region. The length of the two-phase region is defined as the distance from the flash inception point to the location where the condensation shock formed in the diverging section of the nozzle. The length of the two-phase region is also used as a measure for the heat absorption area in the nozzle. The larger the area of heat absorption, the higher the cooling potential is likely to be for the system. Experimental results using water have shown only small temperature drops due to a cavitation process in converging-diverging nozzles, mainly due to the physical properties of water. However,

the models developed should also apply to cavitation with other fluids. Hence, this analysis can form the basis for future evaluation and potential optimization of the nozzle geometry, and the identification of alternative fluids (properties), necessary to achieve maximum cooling potential for fluids flowing through converging-diverging nozzles.

Table of Contents

List of Figures

List of Tables

Acknowledgements

I would like to express my sincere appreciation to each one of my committee members for their persistent guidance, continuous support, and patience during my Ph.D. journey. I would first like to express my sincere gratitude to my major supervisor Dr. Hosni for the huge encouragements and advice when I needed it the most. I am deeply grateful to Dr. Hosni for his unwavering support and belief in me personally and professionally. I would like to extend my sincere gratitude to Dr. Beck for the insightful feedback and suggestions which pushed me to sharpen my knowledge and thinking to bring the work to a higher level. I have learnt a lot from his assistance at every stage of the research project. I would like to offer my special thanks Dr. Sorensen and Dr. Eckels for being on my supervisory committee. I am very grateful for their insightful comments and patience throughout my journey. Their suggestions were influential in shaping my experiment methods and critiquing my results. I would like to extend my sincere thanks to Mr. Don Tomasi, an expert in the industry, for providing the assistance and push we needed to keep the research project going. Finally, I would like to express my gratitude and thanks to all my family members for their help, encouragement, and patience. Without their exceptional understanding and encouragement in the past years, it would be impossible for me to complete my study, specially being busy and away from them most of my time. I am deeply grateful to my parents for motivating and encouraging me to purse higher educations. I would like to thank them for all the moral support and spiritual encouragement when I needed it the most. Thank you all for making my dream come true and for making it possible.

Chapter 1 - Introduction

Understanding how a simple refrigeration cycle works is helpful in the development of a non-vapor compression cooling system. From the second law of thermodynamics, heat always flows from an object at higher temperature to a lower temperature. Heat transfer occurs when there is a temperature difference within a medium or between two media. The research in this thesis focuses on the investigation and the possibility of developing a water-based cooling and refrigeration system using cavitation within a converging-diverging nozzle. Using water as the refrigerant (working fluid) in a system has many advantages. Water as a refrigerant is inexpensive compared to other working fluids. It is also environmentally neutral and safe to be used at any location.

In a simple vapor-compression refrigeration cycle, Figure 1.1, a compressor circulates the working fluid throughout the system; it compresses the cold low-pressure vapor into hot high-pressure vapor. The compressor pushes the hot vapor through the condenser to reject heat and sends the liquid to the expansion valve, and subsequently to the evaporator to provide cooling as it completes a cycle through the absorption of energy as heat. The expansion valve controls the flow of the working fluid to the evaporator; it also lowers the pressure and therefore lowers the temperature. Warm air passes through the evaporator that contains the cold fluid, the cold fluid in the evaporator absorbs the heat from air, and the cold air is delivered to the controlled indoor environment.

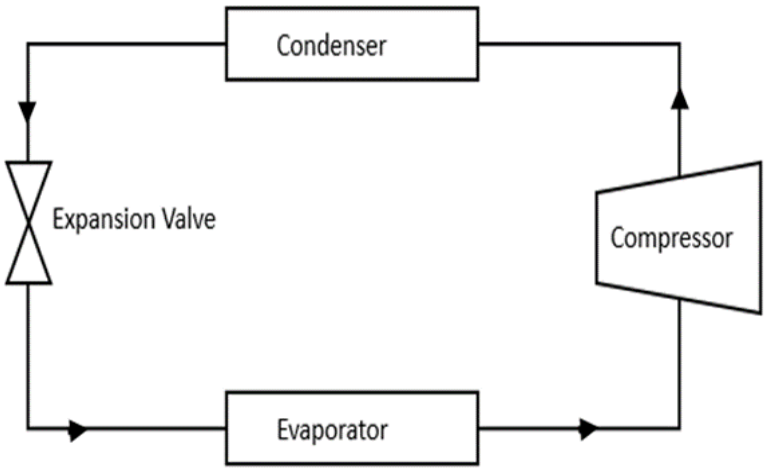

Figure 1.1 Components of a simple refrigeration/ air-conditioning system.

Implementing a converging-diverging nozzle in the system can be used to take advantage of the heat absorption area associated with the length of the cavitation region in the diverging section. Figure 1.2 shows a refrigeration cycle using a converging-diverging nozzle. In a steady flow system, while ignoring the friction and separation effects, the velocity of the fluid entering the nozzle increases as the flow approaches the throat, which has the minimum cross-sectional area. The "Bernoulli effect" causes the pressure to decrease until it reaches a minimum at the throat, or a short distance after the throat, causing cavitation to occur at this location where a two-phase flow starts to develop. The two-phase working fluid moves at low velocities then accelerates downstream of the throat of the nozzle. The pressure drop that occurs in the system causes cavitation, which causes a temperature drop in the fluid. The temperature drop is used to absorb heat from the surroundings. The region of low temperature and pressure is coincident with the length of the two-phase region. This region is used as a measure of heat absorption and can be used to investigate the potential to develop a practical cooling system based on the converging-diverging nozzle.

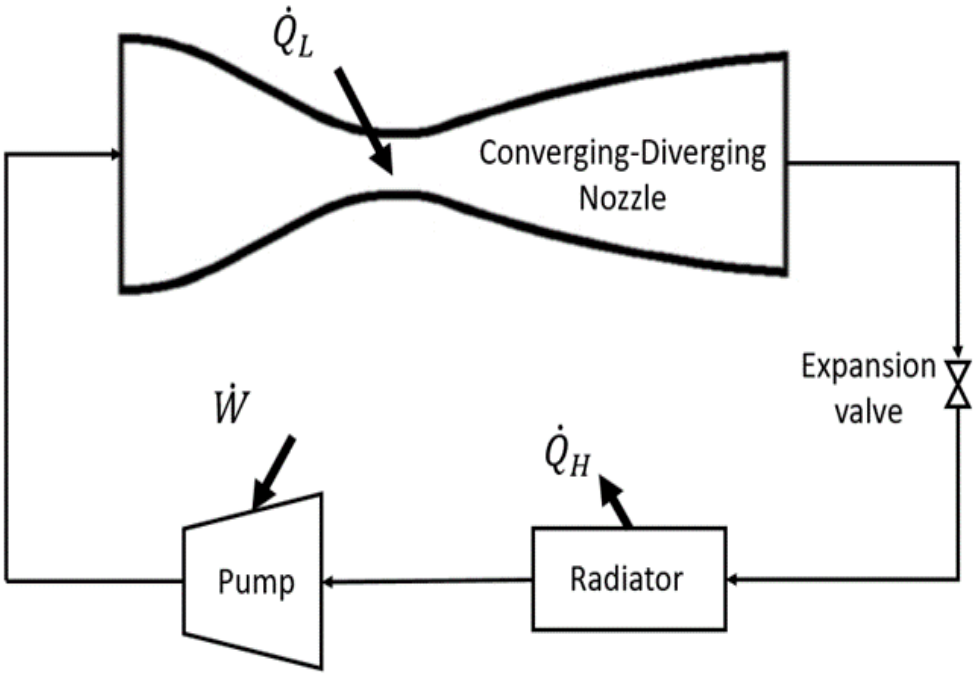

Figure 1.2 Components of a refrigeration cycle using a converging-diverging nozzle

Cavitation can be a common problem in many devices such as pumps, control valves, and heat exchangers. It can cause serious wear and damage as well as a reduction in the device lifetime [2]. Figure 1.3 shows the difference between the cavitation and boiling process lines on a pressure versus temperature phase diagram. Cavitation occurs when the static pressure of the fluid drops below the vapor pressure, while keeping the temperature constant, i.e., the process moves along the constant temperature process line. Boiling occurs when the fluid temperature elevates above the vapor temperature, while keeping the pressure constant, i.e., the process moves along the constant pressure process line. Previous research showed the visualization of a two-phase flow moving at low velocities then accelerating downstream of the throat of a converging-diverging nozzle. The pressure drop that occurs in the system causes cavitation, which causes a temperature drop in the fluid. The temperature drop can therefore be used to absorb heat from the surroundings. This dissertation documents the cavitation occurring in a converging-diverging nozzle. The main objective of the project is to develop a complete model and associated prediction techniques for the cavitation within a nozzle. This includes the inception and the length of the two-phase region, and the condensation shock within the converging-diverging nozzle.

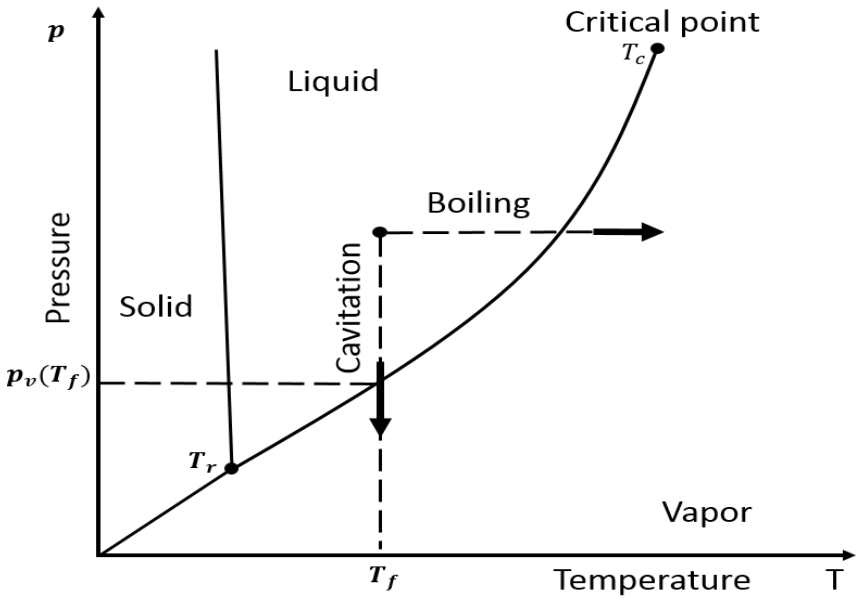

Figure 1.3 Phase diagram of a substance showing cavitation and boiling

1.1 Literature Review

Cavitation

Brennen [2], studied the physics of nucleation in impure or contaminated engineering environments. The study was divided into two different engineering processes: cavitation and boiling.

Cavitation can be described as the nucleation process of changing from liquid to gas at a constant temperature; the change is due to a pressure drop which falls below the saturated vapor pressure. On the other hand, boiling is the nucleation process of changing from liquid to gas at a constant pressure; the change is due to a temperature increase which rises above the saturated vapor/liquid temperature. Although, the basic mechanism of the two processes are similar, a uniform change in pressure in a liquid is more often easier than a uniform change of temperature. Studies have focused on what happens in a given flow if the pressure decreases or the velocity increases so that the pressure in the flow falls below the vapor pressure. A relationship called the cavitation number was introduced by Brennen as a non-dimensional cavitation parameter [2]. The cavitation number is considered to be a measure of the development of cavitation in two-phase flow. It is defined as follows:

$$\sigma = \frac{P_\infty - P_v\,(T_\infty)}{\frac{1}{2}\rho_l U_\infty^2} \tag{1.1}$$

The values U_∞ , T_∞ , and P_∞ are the velocity, temperature, and the pressure of the fluid, P_v is the vapor pressure and ρ_l is the density. Every flow condition has a value of cavitation number even if the flow does not cavitate. If the value of the cavitation number is large, single-phase liquid flow is developed. If the value of the cavitation number decreases, cavitation and nucleation start to form at a value called the incipient cavitation number. When the cavitation number increases to a value higher than the incipient cavitation number, cavitation will vanish. Cavitation will have the same behavior as long as the flow has the same cavitation number value. Previous research by Wilms [7] has shown the visualization of different types of cavitation in a converging-diverging nozzle flow under different nozzle geometries and different

test conditions. The geometry can play a huge role in influencing the resulting velocity and void fraction, which affects the cavitation development. Cavitation takes on several forms, including traveling bubble cavitation, swirl cavitation, shear cavitation, and attached wall cavitation [7].

Nozzle Flows

The converging-diverging nozzle flow is considered one of the most important engineering applications. The behavior of this application depends on the fluid type, the conditions of the fluid and the geometry of the converging and diverging sections of the nozzle. There are three different types of flow considered in a converging-diverging nozzle: single-phase, cavitating, and flashing flow. If the flow enters the nozzle as a subcooled liquid and remain liquid as it exits the nozzle, then it is considered a single-phase flow type. If the flow enters the nozzle as subcooled liquid and a phase change occurs and the pressure recovery is above the vapor pressure, then it is a cavitating flow. On the other hand, if the flow continues to be a two-phase mixture or a single-phase vapor as it exits the nozzle then it is a flashing flow. The pressure distribution for a given flow in a nozzle in terms of pressure versus distance is shown in Figure 1.4 for six different cases of backpressures. A horizontal dashed-line of constant pressure identifies the saturation pressure.

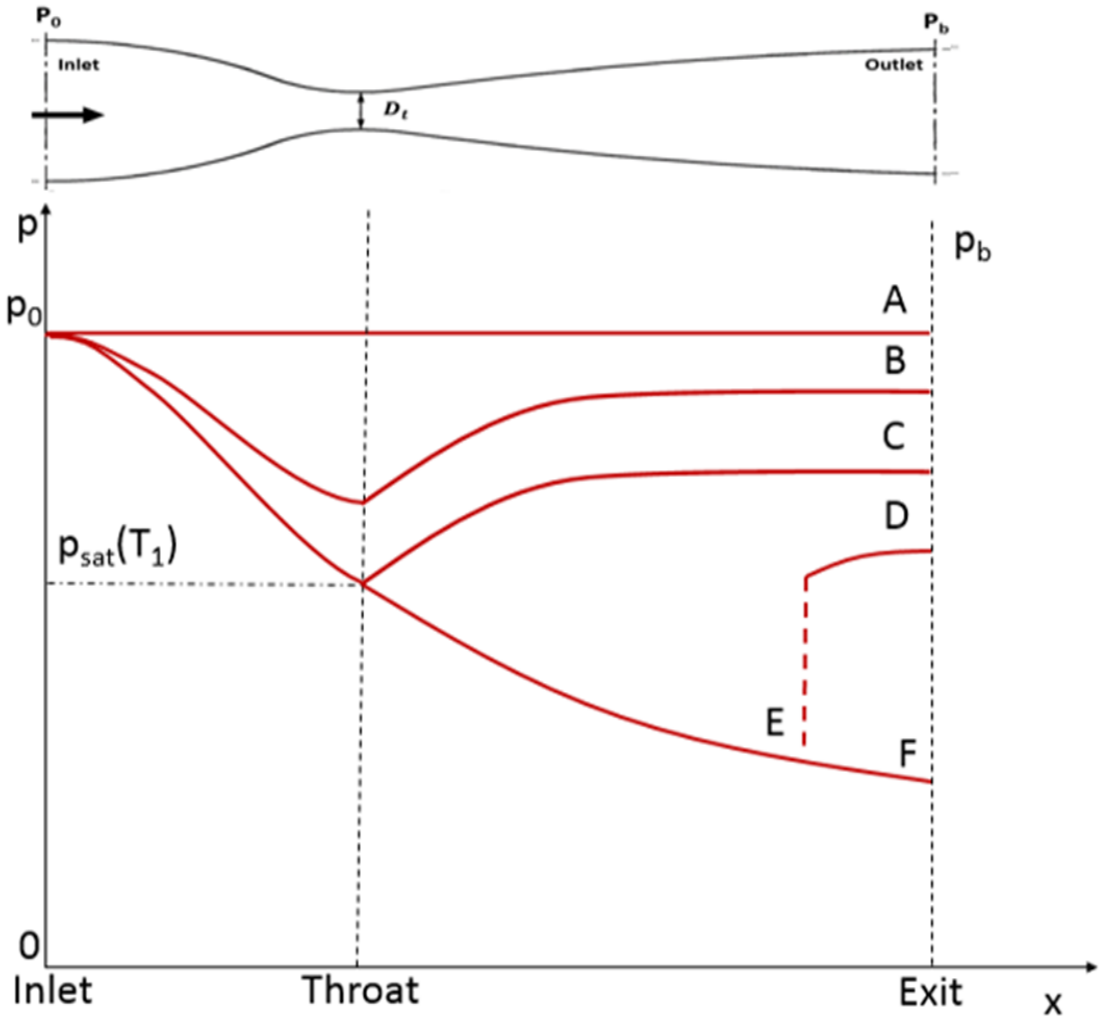

Figure 1.4 Pressure distribution in a converging-diverging nozzle for various back pressures

The flow in the converging-diverging nozzle for given inlet conditions can be controlled by the backpressure. Consider a fluid entering the nozzle at low velocity at nearly the stagnation pressure, as shown in Figure 1.4. Case (A) shows no flow throughout the nozzle when $P_0 = P_b = P_A$. This is because there was no pressure difference between inlet and exit of the nozzle since the flow is driven by the pressure difference. If the backpressure was slightly lowered as shown in case (B), a subsonic flow throughout the nozzle is observed, where velocity increases in the converging section as it reaches a maximum at the throat, and then velocity starts to decrease downstream of the throat in the diverging section. The corresponding local pressure will decrease to a minimum value at the throat then increases downstream of the throat. Sonic velocities can be achieved when the throat pressure is the same as the saturation

pressure which occurs in case (C), $P_b = P_c$. In this case the flow rate will reach its maximum value in the nozzle, which means no matter how much we lower the backpressure, the flow rate will not change. In this case, the nozzle is said to be chocked, or the flow has reached choked conditions in the nozzle. Case (D) shows that the velocity keeps increasing to supersonic velocity and pressure decreases below the saturation pressure. Then, a condensation shock occurs at some point in the diverging section. This shock will move downstream of the throat as the backpressure is lowered, which can get to a point where it shocks right at the exit of the nozzle. This is shown for case (E) where the flow is supersonic throughout the diverging section of the nozzle. Finally, case (F) shows no shock forming within the nozzle as the flow exits. The behaviors seen in Figure 1.4 have similarities to compressible gas flow in a converging-diverging nozzle, the differences relate to the phase change that occurs when cavitation takes place.

Two-phase flow is an example of multiphase flow that occurs in converging-diverging nozzles for cases D, E, and F in Figure 1.4. It refers to the flow of two different phases with common interfaces in a channel. Each phase has its own mass fraction of liquid and gas, its own properties, as well as its own temperature if the flow is not in equilibrium within the nozzle. The main focus in this work will be on liquid-gas flow, which is perhaps the most important form of two-phase flow. These flows exhibit different flow patterns (Figure 1.5) in vertical flows, such as bubbly flow where the liquid phase is continuous with developing bubbles with different shapes and sizes along the flow, slug flow where huge bullet shaped bubbles are formed within the liquid, annular flow where liquid flow along the walls and gas flows in the center of the tube containing some liquid drops in the gas flow, churn flow characterized by an unstable gas phase in large diameter tubes and smoother transiting in smaller diameter tubes, and mist flow where the liquid forms droplets in the gas flow with higher velocities and flow rates. Similar flow patterns may exist in a horizontal flow configuration as well.

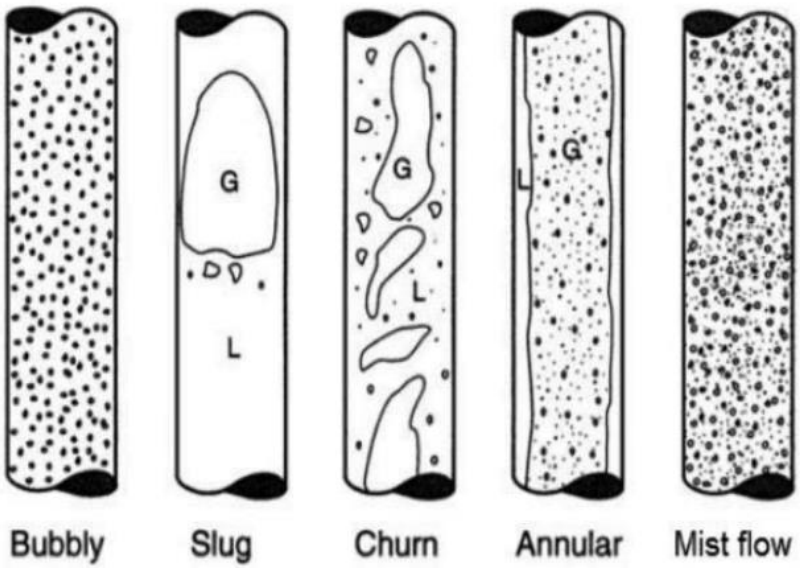

Figure 1.5 Flow patterns in vertical upward flow [16]

Two-Phase Flow Models

There is a wide range of models that have been developed for two-phase flow systems. These include the homogenous equilibrium model, the separated flow model, the multi-fluid model, and the drift flux model. Experimental data and empirical models have been discussed by Awad for circular pipes [8]. The models are important for the design of the experiments and to predict the design parameters. In this research, we will focus on the homogenous equilibrium model and separated flow model.

The Homogenous Equilibrium Model (HEM) is perhaps the simplest formulation compared with the other two-phase models. The HEM simply assumes that the temperature and pressure at any given location of liquid and gas phases are the same and assumes saturation conditions, which means the phases are in thermal equilibrium. It also assumes both liquid and gas phases are traveling with the same velocity, referred to as the no-slip condition, which means the phases are in mechanical equilibrium. Because of the assumptions made for the HEM, it is also considered the least accurate model [9]. The velocity for the liquid and gas phases can be expressed as a function of mass flow rate $\dot{m}$, density ρ, flow quality Q, and void fraction α as follows:

$$V_f = \frac{\dot{m}\,(1-Q)}{\rho_f\,(1-\alpha)} \tag{1.2}$$

$$V_g = \frac{\dot{m}\,Q}{\rho_g \alpha} \tag{1.3}$$

By equating these two velocities, an expression for the void fraction can be formed in terms of quality and densities:

$$\alpha = \frac{1}{1+\frac{1-Q}{Q}\left(\frac{\rho_g}{\rho_f}\right)} \tag{1.4}$$

Different forms or variations of the HEM have been used for various engineering applications to analyze flow in different channels, including the current study of cavitation. Other applications include the study of flow patterns in convergent-divergent nozzles of diesel injectors [9], an improved model in pipe flows [10], and numerical simulation of capillary tubes [11]. Stewart and Wendroff [12] reviewed the application of HEM model for various engineering applications and advised to check the model against more accurate theoretical models. (*1.2*)

Another two-phase flow model is the separated flow model, known as the non-homogenous equilibrium model, or the slip-flow model. A common assumption in the model states that the phases are in thermal equilibrium where both pressure and temperature of the phases at any given location are the same. This is similar to the HEM; however, it provides an improvement to the HEM by applying the slip factor associated with the gas and liquid phases, which is defined as the ratio of gas velocity to the liquid velocity. Incorporation of slip between phases allows for different gas and liquid velocities with different flow properties. Different expressions and correlations of the slip ratio have been developed depending on the specific application assumed in the modeling. A simple expression for the slip ratio is defined as follows:

$$S = \frac{V_g}{V_f} \tag{1.5}$$

Equation (1.4) can subsequently be modified to include the slip ratio as follows:

$$\alpha = \frac{1}{1+\frac{1-Q}{Q}\left(\frac{\rho_g}{\rho_f}\right)S} \tag{1.6}$$

The model seen in Equation (1.6) was used in the work of Lockhart and Martinelli [13]. It is a less accurate model when applied to all flow patterns, but has the advantage of simplicity. The model can be easily developed by assuming that the velocity is different for each phase and applying the conservation equations (continuity, momentum, and energy) for the combined flow. The conservation equations can be developed for each phase separately instead of simply assuming the velocities to be different [13].

Speed of Sound Models

In a cavitating two-phase fluid flowing through a converging-diverging nozzle, as the downstream backpressure is lowered, the velocity of the fluid will initially increase to a maximum value near or downstream of the throat. This maximum throat velocity will be referred to as the sonic velocity. In fact, well downstream of the throat, the resulting two-phase fluid velocity can exceed the speed of sound for a two-phase mixture. Once sonic conditions are reached at the throat, if the backpressure drops any further, the velocity at the throat will not be affected.

The speed of sound in a two-phase flow is more complex than that for single-phase flow. For a single-phase flow, the speed of sound was derived by Wallis [14] as a function of pressure and density where c is the speed of sound, and is given by:

$$c = \left(\frac{\partial P}{\partial \rho}\right)_s^{\frac{1}{2}} \tag{1.7}$$

where this single-phase equation is evaluated with the assumptions of mechanical and thermodynamic equilibrium. The subscript "s" in Equation (1.7) denotes that this derivative is evaluated at constant entropy.

For two-phase flow, different models have been developed to evaluate the speed of sound. Some models assume a two–phase flow in mechanical and thermodynamic equilibrium within a converging-diverging nozzle, ignoring the exchange of mass between the two phases. Wallis [14] has developed such a model for the speed of sound given by:

$$\frac{1}{\rho c^2} = \frac{\alpha}{\rho_g c_g^2} + \frac{1-\alpha}{\rho_f c_f^2} \tag{1.8}$$

where ρ is the mixture density, c_g and c_f are the single-phase vapor and liquid sound speeds, and ρ_g and ρ_f are the single-phase vapor and liquid densities. Franc [15] has developed a model for the speed of sound accounting for the phase change and using the latent heat to reflect the degree of thermal exchange between the phases of the gas and liquid; the expression is given by

$$\frac{1}{\rho c^2} = \frac{\alpha}{\rho_g c_g^2} + \frac{1-\alpha}{\rho_f c_f^2} + \frac{(1-\alpha)\rho_f C_{pl} T}{(\rho_g L)^2} \tag{1.9}$$

where L is the latent heat. This dissertation will be using Equation (1.9) to calculate the speed of sound for the evaluation of the flow in the converging-diverging nozzle under study.

Pressure Drop Models

The discussed two-phase flow models in converging-diverging nozzles depend on important physical parameters including the pressure drop where losses occur in the flow due to friction, gravitational effects, and acceleration. The heat transfer coefficient is also important in the application of these models to the sizing of heat exchangers. The research on the two-phase flow pressure drop started in the 1940's, and then data has been collected from testing various

horizontal and vertical two-phase systems in attempt to develop general models to predict the pressure drop [17]. It is a major consideration in evaluating the operation of condensers and evaporators in engineering refrigeration applications. An overview of single-phase pressure drop characteristics will be presented next, followed by a brief discussion of the frictional pressure drop models applicable in two-phase flow.

Single-phase pressure drop models are used in the development of two-phase pressure drop models associated with a variety of flow regimes; they utilize some form of friction factor as a function of Reynolds number. In smooth pipes, a laminar flow will occur when the Reynolds number is less than 2300 where the resistance of the flow is independent of the wall roughness. The friction factor for laminar flow in different duct geometries can be evaluated from a solution to the Navier-Stokes equations. For pressure drop in pipe or tube flow, the associated Moody (or Darcy) friction factor is defined by:

$$f_D = \frac{-D_h\left(\frac{dP}{dz}\right)}{\frac{\rho U_m^2}{2}} \tag{1.10}$$

where U_m is the mean (or average) velocity and $D_h$is the hydraulic diameter defined as:

$$D_h = \frac{4A}{p} \tag{1.11}$$

where A is the cross-sectional area and p is the wetted perimeter. For a fully developed laminar tube flow, the Darcy friction factor is given by:

$$f_D = \frac{64}{Re_D} \tag{1.12}$$

where Re_D is the Reynolds number based on the diameter D. Turbulent tube flow occurs when the Reynolds number is significantly above 2300. For smooth tubes, the frictions factor is well

represented by the Blasius relation [30], and can be expressed in terms of the Darcy friction factor given by:

$$f_D = \frac{0.3164}{Re_D^{\frac{1}{4}}} \tag{1.13}$$

This equation is valid for all single-phase turbulent flows with Reynolds number $\leq 10^5$. After determining the friction factor for the type of flow, rearranging Equation (1.10) and integrated over the length L, the frictional pressure drop for the single-phase flow can be calculated using the following expression:

$$\Delta P = \frac{2 f_D G^2 L}{\rho D_h} \tag{1.14}$$

where G is the mass flux defined as the mass flow rate divided by the cross-sectional area and *L* is the length of the associated single-phase region.

A majority of the research that was done in the area of two-phase flow pressure drop correlation development included large diameter tubes; a very limited amount of work was done on small diameter tubes or channels. The correlations can be classified based on the cross-sectional area, flow rates of the fluid, and the flow patterns. This research will utilize three different two-phase frictional drop correlations which are the homogeneous equilibrium model (HEM) [10], the Lockhart-Martinelli model [13], and the Friedel model [20].

The homogenous equilibrium model (HEM) [10] assumes that both phases have the same velocity. The two-phase flow is then treated as single-phase flow with a common gas-liquid mixture density given by:

$$\rho = \left(\frac{Q}{\rho_g} + \frac{1-Q}{\rho_f}\right)^{-1} \tag{1.15}$$

As with single-phase flow, the friction factor for this mixture flow depends on Reynolds number as indicated below.

$$f = \begin{cases} \frac{64}{Re}, & Re < 2000 \\ \frac{0.3164}{Re^{\frac{1}{4}}}, & 2000 \leq Re < 20000 \\ \frac{0.168}{Re^{0.2}}, & Re \geq 20000 \end{cases} \tag{1.16}$$

Since the assumption in separated flow is to have different velocities for the gas and liquid phase, the two-phase frictional pressure drop multiplier was developed to account for the single-phase results in modeling by Lockhart and Martinelli [10]. The correlation was developed by considering one of the phases to exist throughout the tube and uses the corresponding mass flux to calculate the Reynolds number. It's based on experimental pressure drop data collected from different testing including air, water, and various oils. The correlation proposed different two-phase friction multipliers, one for each separate phase, which depend on the ratio of liquid to gas phase pressure gradient also known as the Lockhart-Martinelli parameter (X). The Lockhart and Martinelli correlation is given by:

$$\left(\frac{dP}{dz}\right)_{tp} = \emptyset_L^2 \left(\frac{dP}{dz}\right)_L = \emptyset_G^2 \left(\frac{dP}{dz}\right)_G \tag{1.17}$$

$$\left(\frac{dP}{dz}\right)_L = \frac{2f_L G^2 (1-Q)^2}{\rho_L D} \tag{1.18}$$

$$\left(\frac{dP}{dz}\right)_G = \frac{2f_G G^2 Q^2}{\rho_G D} \tag{1.19}$$

$$\emptyset_L^2 = 1 + \frac{C}{X} + \frac{1}{X^2} \ , \ \ \emptyset_G^2 = 1 + CX + X^2 \tag{1.20}$$

$$X^2 = \frac{\left(\frac{dP}{dz}\right)_L}{\left(\frac{dP}{dz}\right)_G} \tag{1.21}$$

where G is the total mass flux and the constant C was introduced by Chisholm [19] as the Chisholm parameter which depends on the separate liquid and gas Reynolds numbers to identify the viscous laminar (V) and turbulent (T) regimes as follows:

$$C = \begin{cases} 5, & for\ Re_L < 1500\ and\ Re_G < 1500 \quad (V-V\ case) \\ 10, & for\ Re_L > 1500\ and\ Re_G < 1500 \quad (T-V\ \ case) \\ 12, & for\ Re_L < 1500\ and\ Re_G > 1500 \quad (V-T\ \ case) \\ 20, & for\ Re_L > 1500\ and\ Re_G > 1500 \quad (T-T\ \ case) \end{cases} \tag{1.22}$$

The Friedel model [20] was developed based on a large database for both vertical and horizontal flow orientations in pipes. The liquid only two-phase multiplier ($\emptyset_{LO}$)is expressed as a function of vapor mass quality (Q) and gas only or liquid only friction factors (f) defined by subscripts GO and LO, respectively. The total mass flux is used as all liquid or all gas, respectively. The Froude number (Fr) was used to account for gravitational effect and the Weber number (We) to account for surface tension effects. Both numbers are expressed in terms of the homogenous mixture density, ρ_h. The Friedel model is presented as a liquid-only two-phase multiplier for the frictional pressure drop, and takes the following form:

$$\left(\frac{dP}{dz}\right)_{tp} = \emptyset_{Lo}^2 \left(\frac{dP}{dz}\right)_{L0} = \emptyset_{Lo}^2 \left(\frac{2fG^2}{\rho_f D}\right) \tag{1.23}$$

$$\emptyset_{Lo}^2 = (1-Q)^2 + Q^2 \left(\frac{\rho_L}{\rho_G}\right)\left(\frac{f_{GO}}{f_{LO}}\right) +$$

$$+ 3.24Q^{0.78}\,(1-Q)^{0.224} \left(\frac{\rho_L}{\rho_G}\right)^{0.91} \left(\frac{\mu_G}{\mu_L}\right)^{0.19} \left(1-\frac{\mu_G}{\mu_L}\right)^{0.7} Fr_{tp}^{-0.045} We_{tp}^{-0.035} \tag{1.24}$$

$$Fr_{tp} = \frac{G^2}{gD\rho_h^2} \quad , \quad We_{tp} = \frac{G^2 D}{\sigma \rho_h^2} \tag{1.25}$$

A number of two-phase correlations for pressure drop, including the ones discussed earlier, have been compared in a study done by Dalkilic et al. [21]. The study compared multiple pressure drop models with experimental results of pressure drop from R600a in a horizontal smooth copper tube and R134a in a vertical smooth copper tube both under annual flow conditions. The study considered different tests conditions, and their results showed that the annular flow models were not affected by the orientation of the tube, either vertical or horizontal, as both predicted good results for the comparison between experimental and two-phase pressure drop. Filip et al. [22] compared seven different two-phase pressure drop models with experimental results for the condensation of R600a and R717 in horizontal tubes. Different tests were done applying various test conditions including different mass flow rates. The overall behavior of the models was studied, and the results showed the importance of vapor mass quality. While most of the two-phase flow pressure drop research has been focused on flow through constant area ducts, little experimental research has been conducted on variable area ducts (or nozzles).

Flash "Cavitation" Inception

The cooling potential of a converging-diverging nozzles using a blow down system was studied by Ahmed [23] in an effort to analyze the cavitation phenomenon. The work focused on understanding the relationship between the pressure drop and cavitation inception in a converging-diverging glass nozzle by varying the temperature of the fluid. Also, understanding the relationship between the cavitation and boundary layer separation was investigated by using inserts in the nozzles. By lowering the backpressure of the nozzle, the flow rate increased until the choked conditions, which results in the flow rate through the nozzle remaining constant even if the backpressure is reduced beyond a certain limit. It was observed that cavitation was initiated at a given backpressure when the flow rate was about 90-95% of the maximum achievable flow rate in the nozzle. Using the experimentally measured flow rates and inlet pressures, Ahmed created Table 1-1, which provides an estimate of the throat pressure under steady state conditions for different temperatures.

Table 1-1 Steady state calculated throat pressure [23]

Temperature	Saturation Pressure (kPa)	Choked Flowrate (mL/s)	Calculated Throat Pressure (kPa)	P_{sat}-P_{throat} (kPa)
25°C	3.2	34.8	-23.2	26.4
50°C	12.3	33.7	-14.4	26.7
70°C	31.2	30.5	4.7	26.5
22°C (Lower P_i)	2.6	32.0	-24.8	27.4

Negative pressure calculated at the throat of the nozzle indicates that the liquid most likely was under tension before it underwent cavitation. The table results suggest that the difference between the saturation pressure and the throat pressure was approximately constant for the three different temperatures. Ahmed visualized the position of the cavitation inception in the converging-diverging nozzle using a high-speed camera. In most of the research, cavitation inception usually occurred at the throat where the pressure was the lowest; however, results showed that at steady state conditions, the cavitation inception position sometimes occurs downstream of the throat. The presence of the "Vena contracta" effect causes the pressure to continue to decrease and the flow rate to continue to increase downstream of the throat in the diverging section of the nozzle. This minimum throat condition appears to be where cavitation initiates, corresponding to an effective minimum cross-section. Ahmed's research, as depicted in Figure 1.6, shows the cavitation onset for different fluid temperatures and constant backpressure, and indicates that the cavitation onset was at approximately the same location for all three different fluid temperatures, downstream of the throat.

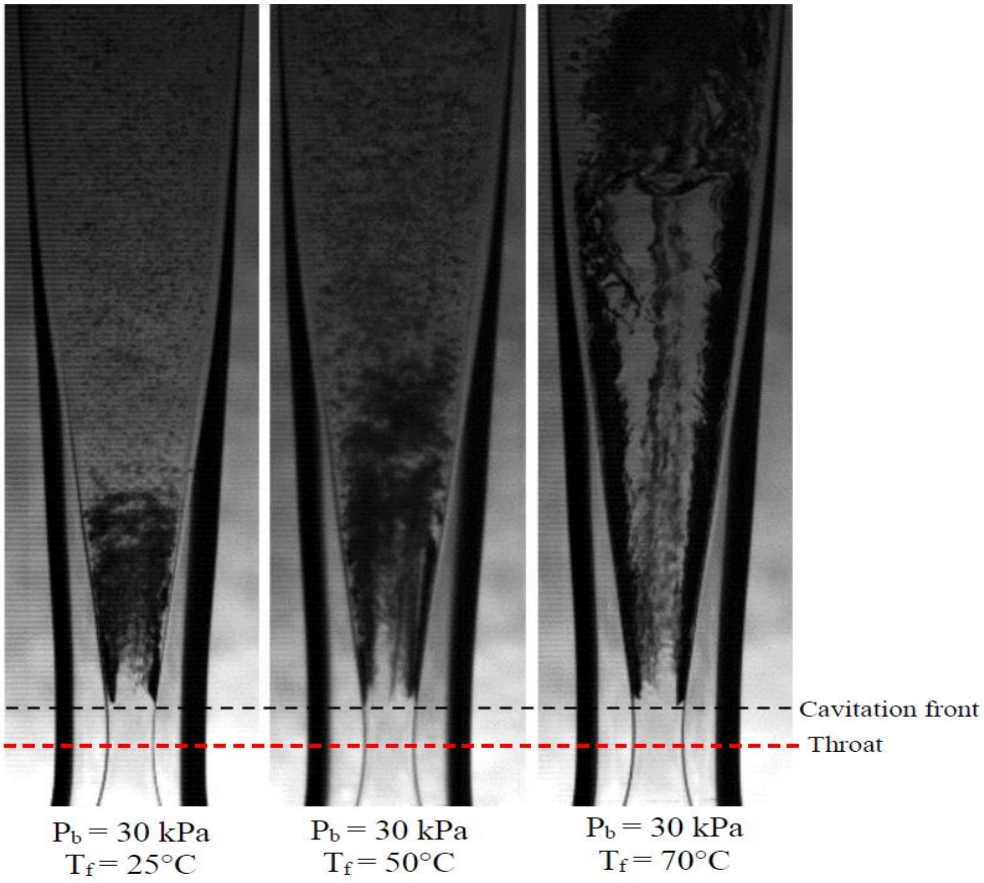

Figure 1.6 Cavitation at different temperatures and constant backpressure [23]

Gallman [24] extended the work that was done by Ahmed in an attempt to improve understanding of the cavitation phenomenon through measurements of the pressure distribution for a two-phase flow in a transparent 3D printed converging-diverging nozzle. The plastic nozzle used in the experiments was made to match the geometry of the converging-diverging glass nozzle that was used in the experiments by Ahmed. Results were taken for an inlet temperature of 20℃ and three different backpressures of 43.2 kPa, 30.5 kPa, and 15.17 kPa absolute pressure. The minimum pressure in the nozzle occurred just a little downstream of the throat due to the "Vena contracta" effect. The cavitation initiation was visualized to occur at the throat where the pressure tap was located, indicating that the hole likely acted as the source of a nucleation site. Table 1-2, created by Gallman, shows the results of the pressure measurements for the tested backpressures.

Table 1-2 Two-phase flow pressure data for each steady-state test in the clear plastic nozzle [24]

Location	43.2 kPa Back Pressure	30.5 kPa Back Pressure	15.17 kPa Back Pressure
0	99.4 (mean)	102.7 (mean)	103.4 (mean)
	99.3, 99.4, 99.5	102.0, 103.0, 103.0	103.4, 103.4, 103.3
0.347	97.5 (mean)	100.0 (mean)	100.1 (mean)
	97.6, 97.3, 97.6	100.0, 100.0, 100.0	100.1, 100.2, 100.1
0.440	74.3 (mean)	76.2 (mean)	81.9 (mean)
	74.4, 74.1, 74.4	76.0, 76.2, 76.5	79.0, 83.4, 83.3
0.534	33.2 (mean)	31.3 (mean)	39.9 (mean)
	34.8, 33.2, 31.6	32.8, 30.6, 30.9	38.4, 41.4, 39.9
0.650	20.4 (mean)	18.9 (mean)	17.1 (mean)
	19.3, 20.5, 21.4	21.1, 17.5, 18.2	17.2, 16.9, 17.2
0.767	39.2 (mean)	35.5 (mean)	30.9 (mean)
	41.9, 38.1, 37.7	35.5, 34.9, 36.3	29.8, 32.0, 31.0
0.883	51.9 (mean)	35.1 (mean)	34.3 (mean)
	52.3, 52.5, 50.8	34.9, 34.1, 36.2	37.3, 33.1, 32.4
1	50.1 (mean)	33.6 (mean)	21.2 (mean)
	50.7, 49.8, 49.7	34.8, 32.4, 33.7	21.3, 21.2, 21.1

Although, limited experimental work has been associated with measuring and visualizing cavitation flash inception, this topic is important to the current research, which attempts to predict the static flashing inception in a converging-diverging nozzle at given operating conditions. Alamgir and Lienhard [25] developed a correlation based on data from different sources which relates the static pressure undershoot at the inception point to the depressurization rate at the inlet temperature. This correlation was used to determine the flashing inception point for both pipe and nozzle during the depressurization of water for non-flowing systems. The pressure undershoot is the difference between the saturation pressure and the superheated pressure that occurs when a fluid that has a high pressure and a high temperature is depressurized to a superheated state and reaches a pressure below the saturation pressure. The correlation for the static flash inception line, pressure undershoot as a function of local properties, was given by:

$$\Delta P_{Fio} = P_{sat} - P_{Fi} = 0.253 \frac{\sigma^{\frac{3}{2}}}{\sqrt{kT_c}} \frac{T_R^{13.73} \sqrt{1+14 \sum'^{0.8}}}{\left[1-\frac{v_f}{v_g}\right]} \quad (1.26)$$

where P_{sat} is the saturation pressure at the inlet temperature in Pa, P_{Fi} is the pressure at the flashing inception in Pa, k is Boltzmann's constant in J/K, σ is the surface tension in N/m, T_R is the reduced temperature and T_c is the critical temperature in K, v_f and v_g are the specific volumes of saturated liquid and saturated vapor at the inlet temperature in m^3/kg, and $\sum'$ is the depressurization rate in Mbar/s. The correlation for the static undershoot was developed with the following ranges for both the reduced inlet temperature and the depressurization rate given by:

$$0.515 \leq T_R \leq 0.935$$

and

$$0.004\ Mbar/s \leq \sum' \leq 1.803\ Mbar/s$$

Results showed that the pressure undershoot was constant for depressurization rates lower than 0.004 Mbar/s and increased as the depressurization rate increased above this value. The flashing inception superheats were at temperatures of 50°C or higher.

The flashing inception work by Alamgir and Lienhard for non-flowing systems was extended in an effort to calculate the flashing inception in flowing systems by Abuaf [36]. It's seen that the major difference between the static flash inception correlation and the new correlation by Abuaf is due to the presence of turbulent pressure fluctuations in a moving fluid. This finding characterizes the flashing inception correlation as a function of inlet temperature, depressurization rate, and turbulent pressure fluctuations of the fluid. Abuaf [36] presented an equation for the flashing inception for liquids flowing steadily in a nozzle by combining the static flashing inception correlation and the turbulent pressure fluctuations, which accounts for the turbulence effects and the area ratio, as follows:

$$\Delta P_{Fi} = \Delta P_{Fio} - 27\left(\frac{\overline{u'^2}}{U^2}\right)\frac{G^2}{2\rho_l}\left(\frac{A_z}{A_{in}}\right)^{1.4} \tag{1.27}$$

where U is the mean velocity of the flow, $\frac{\overline{u'^2}}{U^2}$ is the square of the turbulent velocity fluctuation which depends on the Reynolds number, G is the total mass flux, A_z is the cross-sectional area at any location z, and A_{in} is the cross-sectional area at the inlet. The equation shows that with increasing mass flux the flashing inception undershoot will decrease in magnitude. Wu et al. [27] proposed the decompression rate for a particle of fluid flowing in a nozzle by considering a Lagrangian approach to extend the static experiments to flowing systems, yielding

$$\Sigma' = \frac{dP}{dt} = \left.\frac{\partial P}{\partial t}\right]_z + U\left.\frac{\partial P}{\partial z}\right]_t \tag{1.28}$$

where $\left.\frac{\partial P}{\partial t}\right]_z$ represents the static depressurization rate, and $U\left.\frac{\partial P}{\partial z}\right]_t$ represents the convective (dynamic) depressurization rate. Wu et al. research [27] used published data by Brown [28] for different subcooled inlet conditions in converging-diverging nozzles flows with flashing occurring in the nozzle. The pressure distribution in the converging-diverging nozzle is shown in Figure 1.7 for two different runs with inlet temperatures of 270℃ and 286℃. An equation for the local depressurization rate using Bernoulli's equation and mass conservation, relating the depressurization rate to the rate of nozzle area change with respect to position, was introduced as follows:

$$\Sigma' = \frac{dP}{dt} = \frac{dP}{dz} * \frac{dz}{dt} = \frac{\dot{m}^3}{\rho^2 A^4} * \frac{dA}{dz} \tag{1.29}$$

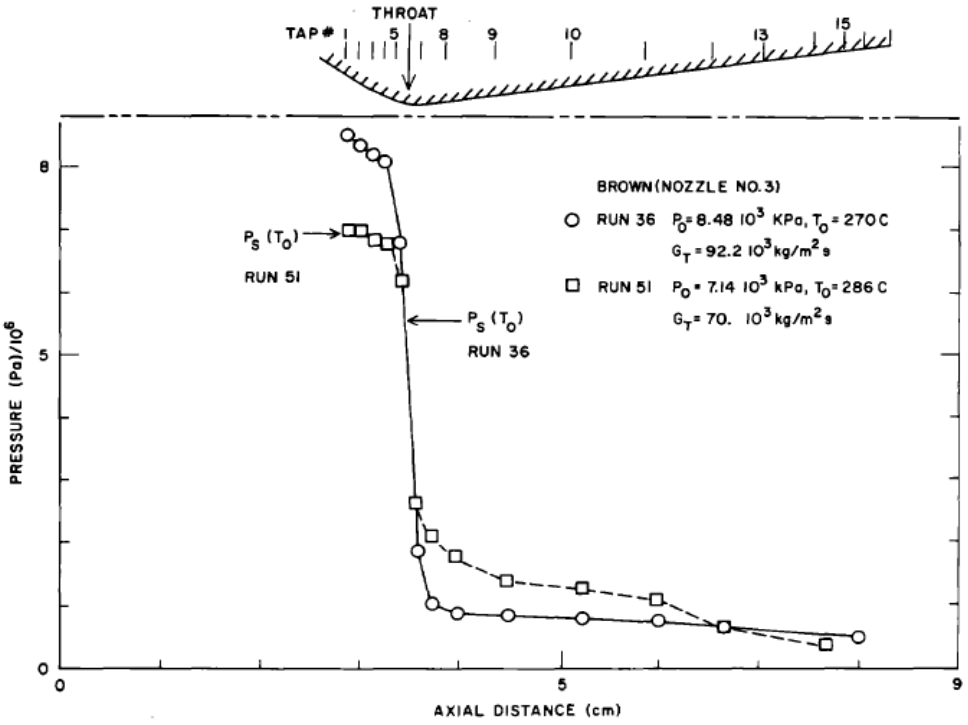

Figure 1.7 Pressure distributions for two experiments (Run 36, 51) under 18.3 and 50℃ subcooled inlet conditions [28]

Figure 1.8 shows the static pressure undershoot at flashing onset as a function of the depressurization rate [27]. Also, using Brown's experimental data and Equation (1.28), the experimental superheats are represented as the dashed line in Figure 1.8. The solid curve represents the static flashing inception for each run. The subcooled fluid conditions are indicated for taps at a condition where $P_{sat} - P \leq 0$. The superheated fluid conditions represent the region between the solid curve where $P_{sat} - P = 0$ and the horizontal axis. For (Run 36), the figure shows results that the fluid at tap 3, 4, and 5 is subcooled. The condition between tap 5 and the throat (tap 6) crosses the inception line, where flashing was predicted to occur. For (Run 51), the figure shows results that the fluid at tap 1 and 2 is subcooled, but pressure tap 3, 4, and 5 is superheated. Flashing again occurred between tap 5 and 6.

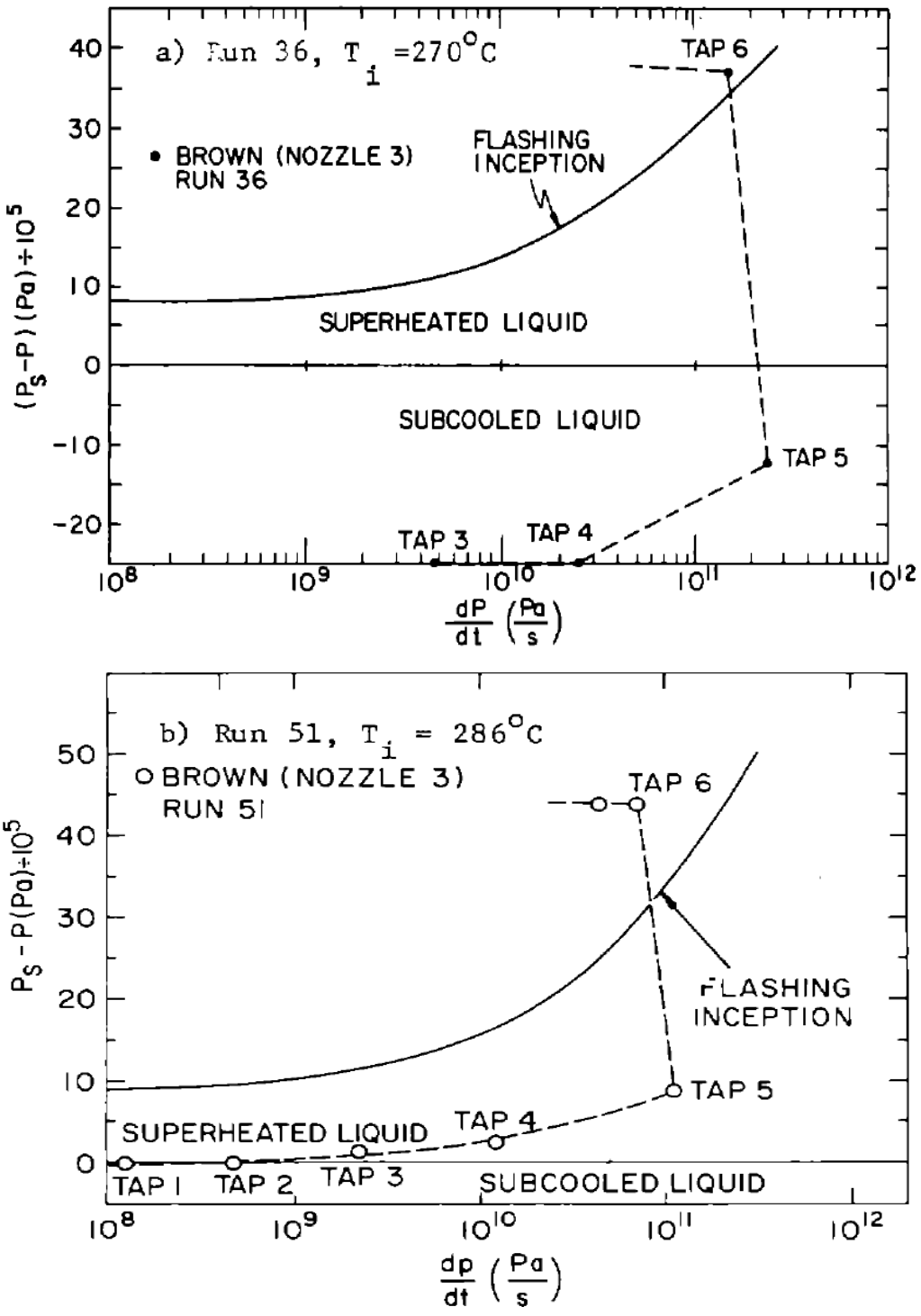

Figure 1.8 Comparison of the flashing inception predicted by Alamgir and Lienhard [25] (solid line) with the locus of the liquid depressurization history (circles connected by dashed line) in Brown's nozzle for two different runs [28] [27]

Davis [3] conducted research focused on the development of cavitation where a transparent planar venturi nozzle was used in a blow-down system facility. The system includes two tanks used as liquid reservoirs; the fluid was pumped down to the needed pressure by using a vacuum pump. The nozzle was designed with a 5^{th} order polynomial shape; inlet and exit diameters were 19 mm, and the throat diameter was 1.58 mm. A high-speed camera was used to acquire the flow visualization [3]. Figure 1.9 shows the flow going from left to right in a water test with a pressure downstream of 20 kPa. Figure 1.10 shows pressure measurements for water along the nozzle centerline versus position, and the data shown has been normalized by the inlet pressure. The nozzle geometry is also shown in the figure for reference, where the throat is at the relative nozzle length position $x/L = 0.3$. Four cases were introduced in Figure 1.10 by the backpressure and inlet pressure ratios of 0.2, 0.3, 0.55, and 0.75. The backpressures of the four cases are 60 kPa, 40 kPa, 20 kPa, and 15 kPa, respectively. From the figure, the pressure profiles for 60 kPa and 40 kPa backpressure are single-phase throughout the nozzle, which means cavitation did not occur in the nozzle. The next two cases showed that, as the pressure decreases, cavitation occurs in the nozzle close to the throat. After cavitation, the flow will be in the supersonic region until it reaches a shock for both cases at $x/L = 0.45$ for case 3 and $x/L = 0.6$ for case 4. This can be seen in case E in Figure 1.4. The position of the shock in the nozzle can be controlled with either decreasing or increasing the backpressure. Void fractions were measured as well, and bubbles started to develop at $x/L \approx 0.25$, followed by an abrupt change in void distribution at $x/L \approx 0.6$.

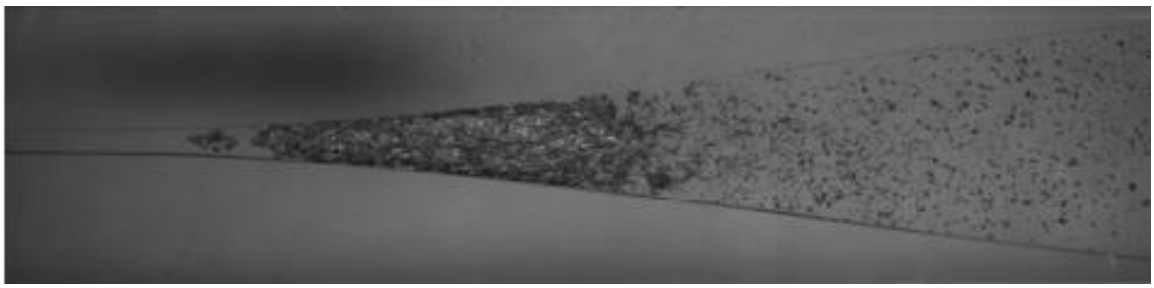

Figure 1.9 Capture of water cavitation mixture, Davis [3]

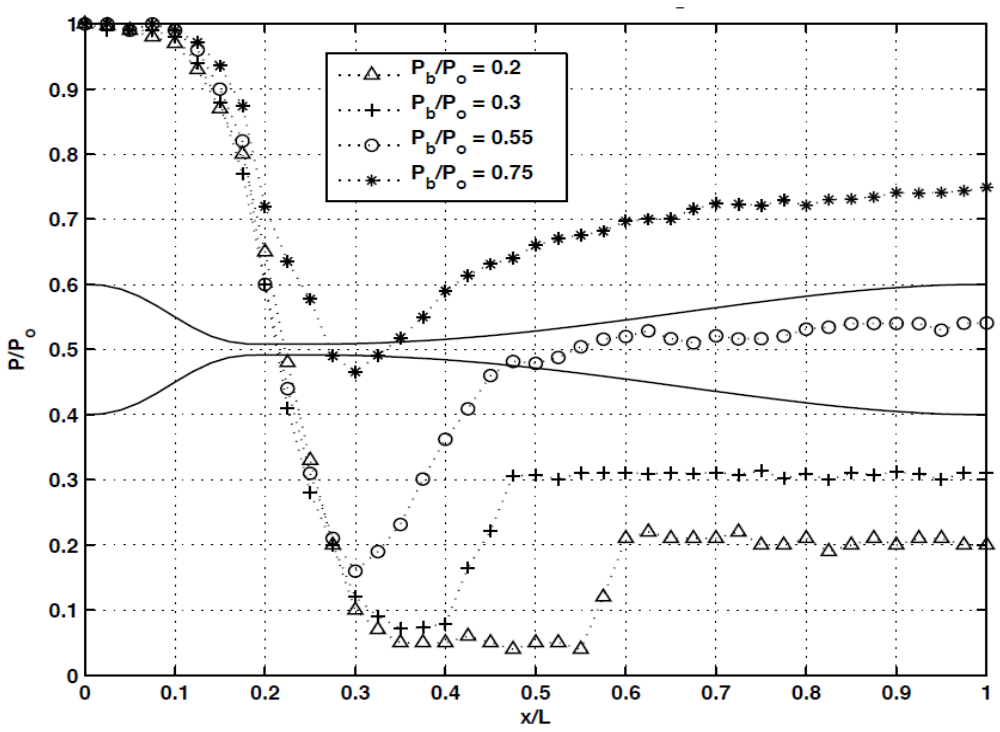

Figure 1.10 Axial pressure distribution in water, Davis [3]

Length of Two-Phase Region (Condensation Shock)

Soyama [29] analyzed the length of the cavitation region for water flowing through a venture tube with respect to the upstream pressure, which is the injection pressure, and the downstream pressure which is the pressure at the throat of the tube. The fluid was pressurized using a diaphragm pump and injected into the system. The diaphragm pump controlled the upstream pressure, and the downstream pressure was controlled by a valve. Figure 1.11 shows the dependence of the cavitating region on different upstream pressures at a constant downstream pressure. Similarly, Figure 1.12 shows the dependence of the cavitating region on different downstream pressures at a constant upstream pressure. Two different types of experiments were done employing a flow visualization technique using a high-speed camera. The length of the cavitation region is shown by varying the upstream pressure at constant downstream pressure in Figure 1.11. In Figure 1.12, the length of cavitation region is exhibited by varying the downstream pressure at constant upstream pressure. Results from the figures show that increasing the upstream pressure at constant downstream pressure, caused the length

of the cavitation region to increase. This was due to an increase in the pressure difference, which resulted in a decrease in the cavitation number from Equation (*1.1*). On the other hand, increasing the downstream pressure at constant upstream pressure, caused the length of cavitation region to decrease due to a decrease in the pressure difference.

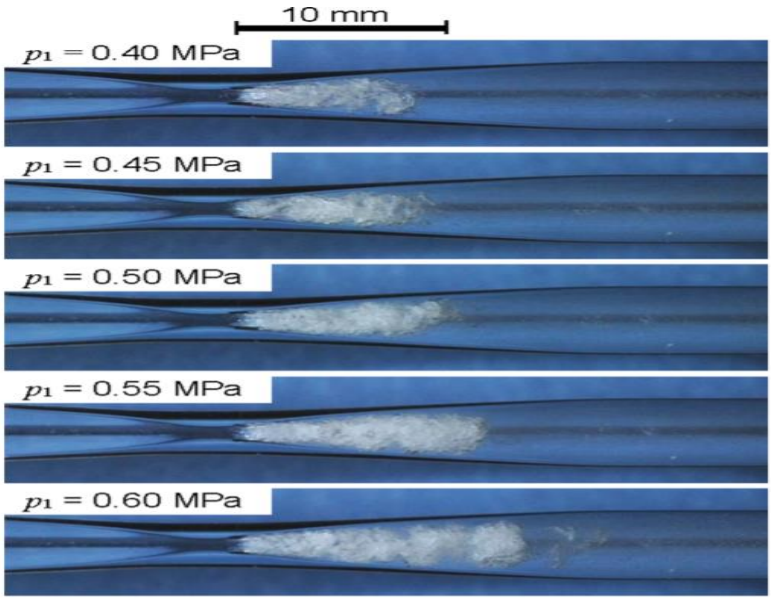

Figure 1.11 Cavitating region as a function of upstream pressure at constant downstream pressure P_2 = 0.12 MPa. Reproduced from Soyama [29] with the permission of AIP Publishing

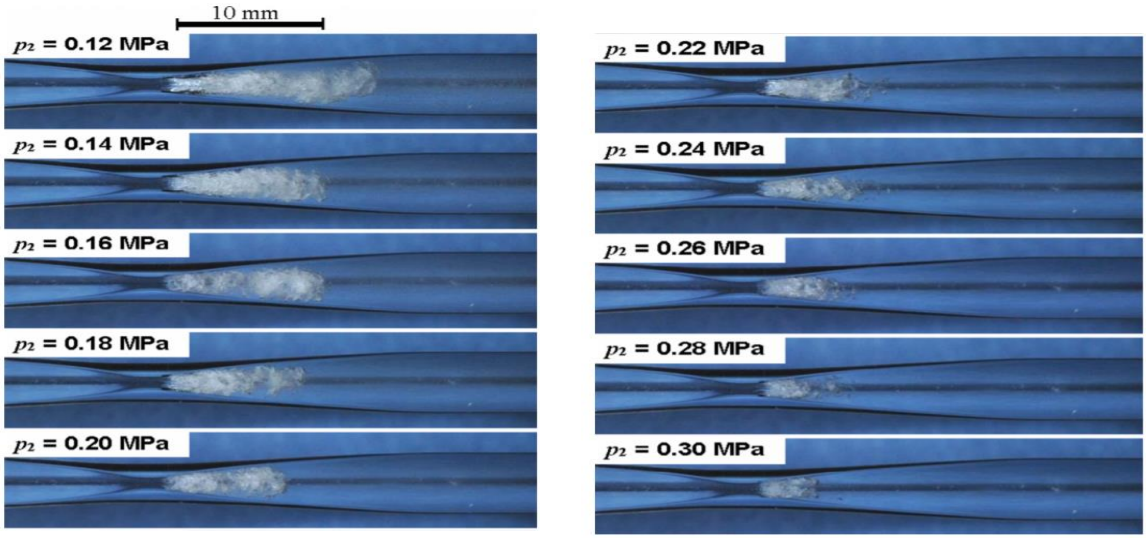

Figure 1.12 Cavitating region as a function of downstream pressure at constant upstream pressure P_1 = 0.6 MPa. Reproduced from Soyama [29] with the permission of AIP Publishing

Ahmed [23] measured the cavitation length (the length of two-phase flow region) in a glass converging-diverging nozzle while varying the backpressures for different water inlet temperatures of 25°C, 50°C, and 70°C. A high-speed camera was used to capture visualization of the cavitation region in the nozzle. As mentioned earlier, varying the backpressures in the downstream reservoir did not affect the location of the cavitation onset, as it was always observed to occur at the same location. Flow visualization and quantitative measurements showed an increase in the length of cavitation region as a result of a decrease in the backpressure. For sufficiently high backpressure, the cavitating two-phase flow always condensed back to single-phase liquid within the diffuser section of the nozzle; however, for much lower values of backpressures, the flow continued to be two-phase mixture throughout the diverging section to the exit of the nozzle. Figure 1.13 summarize the results of the length of two-phase region in terms of absolute backpressure in the nozzle for three different water temperatures. A linearly increasing trend line is shown in the figure for the length of the cavitation region with increasing backpressure. The intersection of the trend line with the horizontal axis indicates the absolute value of the backpressure where the cavitation initiated within the nozzle.

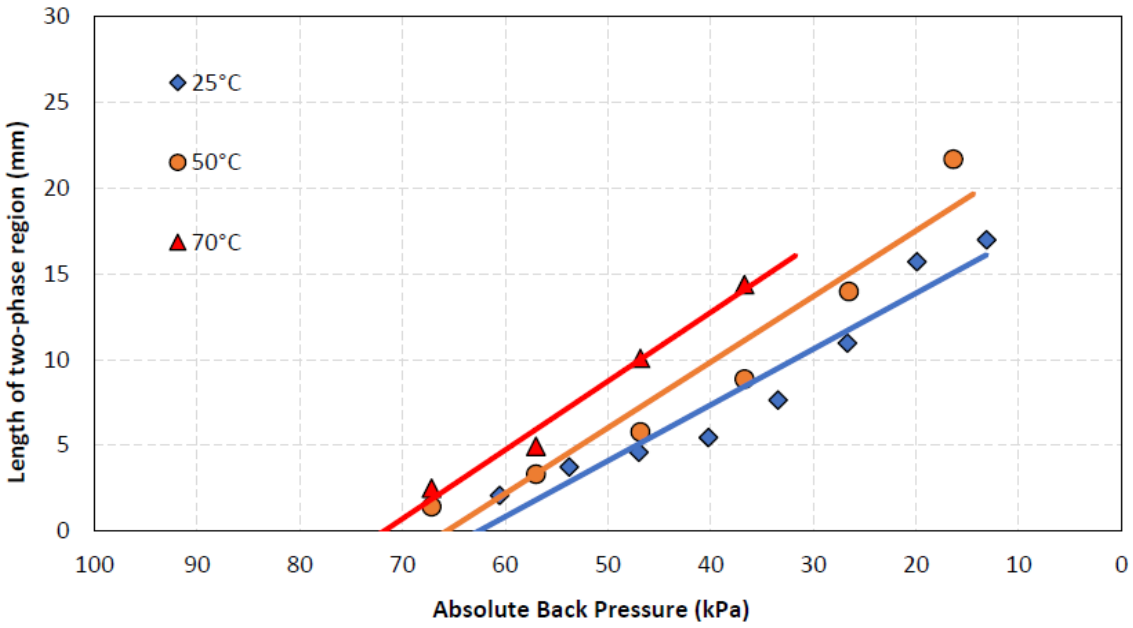

Figure 1.13 Variation of cavitation length with temperature and backpressure, Ahmed [23]

In a study by Nakagawa, et. al [4] with CO2 as an alternative refrigerant in a converging-diverging nozzle, condensation shocks were observed. A modified simple vapor compression cycle was used as the refrigeration cycle, and the compressor power input was 1.3 kW. A rectangular converging-diverging nozzle was used, and the length of the diverging section was 8.38 mm. A shorter length nozzle was observed to give a higher outlet pressure, whereas, a longer length nozzle resulted in lower outlet pressure [4]. Figure 1.14 shows results for short nozzles, the biggest backpressure range was 3.6-5.9 MPa. As the inlet temperature increased, the backpressure increased causing the condensation shock amplitude to increase. Two types of condensation shocks were discovered while testing the short nozzles. The first type was the pseudo condensation shock with a slow increase in pressure, as seen in the first plot of each section in Figure 1.14. A second type was a dispersed condensation shock with gradual increase in pressure, as seen in the last two plots of each section in Figure 1.14 [4].

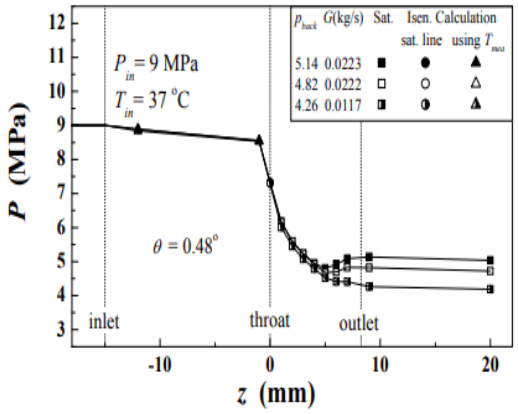

(a) Inlet at 9 MPa and 37 °C: Phase change started from saturated liquid.

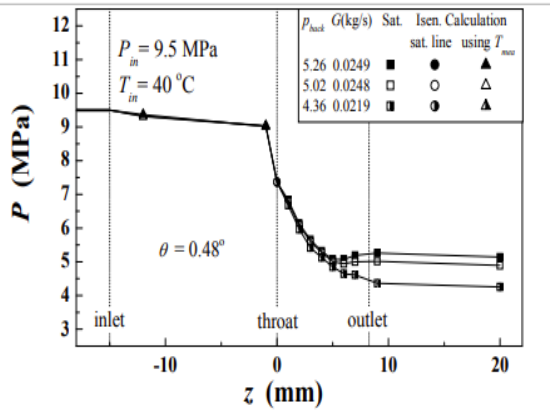

(a) Inlet at 9.5 MPa and 40 °C: Phase change started from saturated liquid.

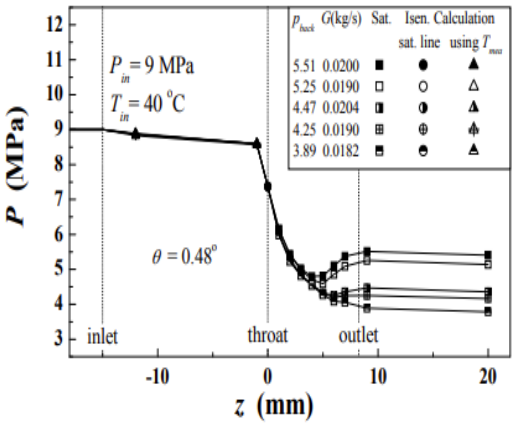

(b) Inlet at 9 MPa and 40 °C: Phase change started from saturated vapor.

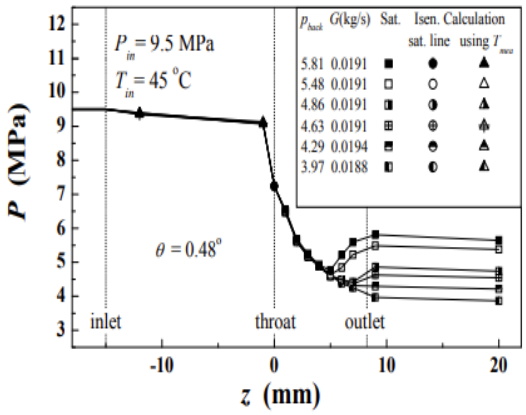

(b) Inlet at 9.5 MPa and 45 °C: Phase change started from saturated vapor.

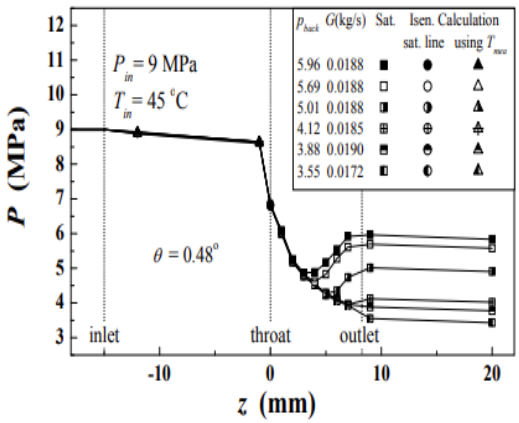

(c) Inlet at 9 MPa and 45 °C: Phase change started from saturated vapor.

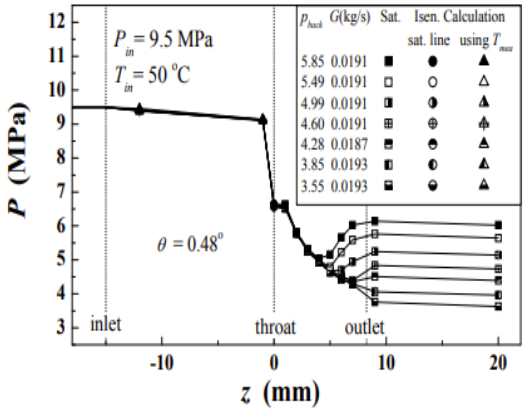

(c) Inlet at 9.5 MPa and 50 °C: Phase change started from saturated vapor.

Figure 1.14 condensation shocks at inlet pressures and various temperatures; a. 9 MPa and b. 9.5 MPa [4]

1.2 Research Objectives

The project was originally initiated with the goal of developing a water-based cooling and refrigeration system. Understanding cavitation in a water flowing system through converging-diverging glass nozzles was one of the initial objectives of the project. This dissertation develops a complete model and evaluation techniques to predict the results of the cavitation phenomena in a converging-diverging nozzle geometry, and the effects of cavitation developing on the flow. The model focuses on the prediction of the flash inception in the nozzle, the length of two- phase region when the cavitation occurs, and the location of the condensation shock before the flow exits the nozzle. The research also focusses on the fundamental knowledge of the conservation equations to evaluate the frictional pressure drop for a comparison between a smooth pipe and a diffuser, the pressure drops after the cavitation inception, and the location of the condensation shock (shock wave). The results provide an understanding of the flow, both before and after the cavitation occurring in the nozzle which will be useful to improve (or at least evaluate) the cooling capacity in the converging-diverging nozzles experiments. Two items which summarize the key research topic objectives of this project are the investigation of the cavitation phenomena itself, and the development of quantitative results for comparison with experiment. It appears that the work presented here represents the first time that the full range of cavitation phenomena taking place within a converging-diverging nozzle has been analyzed in a manner similar to the single-phase compressible gas flow converging-diverging nozzle counterpart.

1.2.1 Cavitation Phenomena

Cavitation is an important phenomenon that occurs in many flow devices such as pumps, control valves, and heat exchangers. As was discussed earlier in the literature review, cavitation can be classified as traveling bubble cavitation, vortex cavitation, cloud cavitation, and attached or sheet cavitation. The location of cavitation inception and bubble collapse in a nozzle plays a major role in establishing the length of the cavitation region, which is a measure of the area available for heat absorption and consequently relates to the ultimate cooling capacity of the nozzle.

1.2.2 Quantitative Results

The analysis presented here utilizes water flow in a converging-diverging nozzle to investigate the fundamental physics associated with the different flow processes that take place in general with a nozzle undergoing cavitation.

Chapter 2 - Fundamental Knowledge

This chapter focuses on the understanding of fundamental thermodynamics phenomena and the development of practical knowledge relevant to the cavitation process. In the next chapter, the equations of conservation of mass, momentum, and energy will be applied to the different regions within a converging-diverging nozzle in order to develop a complete model of the two-phase flow and cavitation phenomena throughout the nozzle. It is important to start with a general formulation of the conservation equations in this chapter for a given system to be applied in Chapter 3 to the nozzle; each section of the nozzle will have different assumptions made. An analysis of the homogenous equilibrium model, where two-phase phenomena take place, is also discussed in this chapter and will be applied to the nozzle in Chapter 3.

2.1 Conservation Equations

The conservation of mass, momentum, and energy principles will be developed in this section for a general control volume. Figure 2.1 shows a control volume of a variable cross-sectional area associated with a circular duct. For the development of governing equations, the single-phase liquid fluid flow in the variable circular duct is assumed to be incompressible up to the initiation of cavitation. The fluid flows along the z-axis from the left to the right. A slice of the circular duct is defined as the control volume and assumed to be stationary. For development of the conservation equations, mean values of various properties across the circular duct at each z-location are used. The mass, momentum, and energy equations are developed below

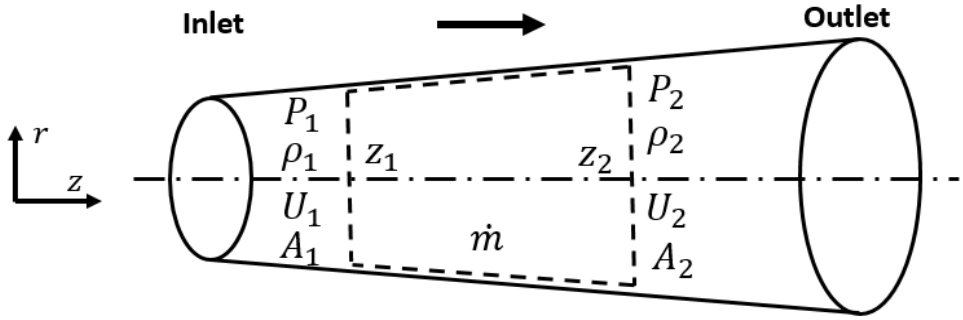

Figure 2.1 Control volume of a circular duct with variable cross-sectional area.

2.1.1 Conservation of Mass

A system is defined as a collection of unchanging contents, so the conservation of mass principle for a system is simply stated as [30]:

Time rate of change of the system mass = 0

or

$$\frac{dM}{dt}_{system} = 0 \tag{2.1}$$

where M is the system mass and t is the time. The principle of conservation of mass for a control volume states that the net rate of mass flow entering the control surface equals the time rate of change of the mass within the control volume. Applying Equation (2.1) to the control volume shown in Figure 2.1, the conservation of mass for a control volume that is surrounded by a control surface is given in a general form by the following:

$$\frac{dM}{dt}_{system} = \frac{d}{dt}\left(\iiint \rho \, dv\right)_{cv} + \left(\iint \rho \left(\vec{U} \cdot \hat{n}\right) dA\right)_{cs} \tag{2.2}$$

where ρ is density, *v* is volume, $\hat{n}$ is an outward unit normal vector, and $\vec{U}$ is velocity vector. The first term on the right-hand side of Equation (2.2) is the mass accumulation rate in the control volume and the second term is net rate at which mass leaves the surface of the control volume. For steady flow, the mass in the control volume will not change; therefore

$$\frac{d}{dt}\left(\iiint \rho \, dv\right)_{cv} = 0$$

Thus,

$$\left(\iint \rho \, (\vec{U} \cdot \hat{n}) \, dA\right)_{cs} = 0 \tag{2.3}$$

With the assumption of one-dimensional flow with uniform velocities across any cross-section in Figure 2.1, Equation (2.3) results in

$$\left(\iint \rho \left(\vec{U} \cdot \hat{n}\right) dA\right)_{cs} = (\rho UA)_{out} - (\rho UA)_{in} = 0 \qquad (2.4)$$

or

$$(\rho UA)_{out} - (\rho UA)_{in} = 0 \qquad (2.5)$$

A simple relationship for the conservation of mass in steady, one dimensional, single-phase flow, having one inlet and one outlet, results in the inlet mass flow rate equal to the outlet mass flow,

$$\dot{m}_{out} = \dot{m}_{in} \qquad (2.6)$$

or

$$(\rho UA)_{out} = (\rho UA)_{in} \qquad (2.7)$$

For the inlet and outlet cross sectional areas shown in the schematic diagram in Figure 2.1, Equation (2.7) is written as,

$$(\rho UA)_2 = (\rho UA)_1 \qquad (2.8)$$

where the notations 1 and 2 refers to the inlet and the outlet sections. If the density is assumed to remain constant, i.e. incompressible fluid, the equation simplifies finally to

$$(UA)_2 = (UA)_1 \qquad (2.9)$$

2.1.2 Conservation of Momentum

The momentum principle is a representation of Newton's second law, which states that the sum of all external forces acting on a control mass equals the time rate of change of the linear momentum of the system (control mass). Forces on a system can be due to surface forces such as pressure and viscous forces, or due to body forces, (namely, gravitational forces). The principle states that if an object loses momentum, it will be gained by another object, resulting in the total amount being constant unless friction is involved. Newton's second law for a system (control mass) takes the following form:

$$\sum \vec{F} = \frac{d\vec{P}}{dt}_{system} = m\ \frac{d\vec{U}_{cm}}{dt} \tag{2.10}$$

where $\vec{P}$ is the total momentum in the system, m is the total inertial mass, and $\vec{U}_{cm}$ is center of mass velocity. The resultant forces acting on the system are the surface forces and body forces shown as

$$\vec{F} = \vec{F}_{surface} + \vec{F}_{body} \tag{2.11}$$

Equation (2.10) is easy to apply to a system of particles, but for the case of fluid flowing in a system, it requires modification to account for momentum entering and leaving a specified control volume. The axial component of the linear momentum principle applied to a given control volume, can be expressed as follows:

$$\left(\iiint \vec{f}_{body}\ dv\right)_{cv} + \left(\iint \vec{f}_{surface}\ dA\right)_{cs} = \frac{d}{dt}\left(\iiint \rho \cdot \vec{U}\ dv\right)_{cv} + \left(\iint \vec{U}\ \rho\left(\vec{U} \cdot \hat{n}\right) dA\right)_{cs} \tag{2.12}$$

The left-hand side of Equation (2.12) represents the sum of body forces (gravity) and surface forces (pressure and shear) acting on the CV and are defined as,

$$\left(\iiint \vec{f}_{body}\, dv\right)_{cv} = \left(\iiint \vec{g}\, \rho\, dv\right)_{cv} \tag{2.13}$$

$$\left(\iint \vec{f}_{surface}\, dA\right)_{cs} = \left(\iint P\, d\vec{A}\right)_{cs} + \left(\iint \vec{\tau}\, dA\right)_{cs} \tag{2.14}$$

The first term on the right-hand side of Equation (2.12) represent the instantaneous rate of momentum storage within the CV, and the second term represent the net rate at which momentum leaves the CV. Assuming one-dimensional, uniform velocity, steady flow, and ignoring gravitational forces and shear forces, Equation (2.12) reduces to

$$\left(\iint \vec{f}_{surface}\, dA\right)_{cs} = \left(\iint \vec{U}\, \rho\, \left(\vec{U} \cdot \hat{n}\right) dA\right)_{cs} \tag{2.15}$$

The right-hand term in (2.15) is simplified as

$$\left(\iint \vec{U}\, \rho\, \left(\vec{U} \cdot \hat{n}\right) dA\right)_{cs} = U_2(\rho U A)_2 - U_1(\rho U A)_1 \tag{2.16}$$

Neglecting friction, the axial component of force from the left hand-side of Equation (2.15) is expressed by

$$\left(\iint \vec{f}_{surface}\, dA\right)_{cs} = P_1 A_1 - P_2 A_2 + \int_{z_1}^{z_2} P \left(\frac{dA}{dz}\right) dz \tag{2.17}$$

where the notations 1 and 2 refers to the inlet and the outlet sections. Combining Equations (2.16) and (2.17) into (2.15), yields the basic conservation of momentum equation for a control volume

$$U_2(\rho U A)_2 - U_1(\rho U A)_1 = P_1 A_1 - P_2 A_2 + \int_{z_1}^{z_2} P \left(\frac{dA}{dz}\right) dz \tag{2.18}$$

2.1.3 Conservation of Energy

The principle of the conservation of energy represents the first law of thermodynamics, which states that for a closed system (fixed mass) the rate of change of total energy of the system equals the net rate of energy entering the system as heat minus the net rate of energy leaving the system as work. In equation form, it is given as:

$$\frac{dE}{dt} = \dot{Q}_{cv} - \dot{W}_{cv} \tag{2.19}$$

where E is the total energy of the system, $\dot{Q}_{cv}$ is the heat rate, and $\dot{W}_{cv}$ is the work per unit time (power). For a general open system, the conservation of energy is given as,

$$\frac{d}{dt}\left(\iiint e\,\rho\,dv\right)_{cv} + \left(\iint \left(\frac{P}{\rho} + e\right)\rho\left(\vec{U}\cdot\hat{n}\right)dA\right)_{cs} = \dot{Q}_{cv} - \dot{W}_{cv} \tag{2.20}$$

where

$$e = \left(u + \frac{1}{2}U^2 + gz\right) \tag{2.21}$$

In Equation (2.20), e is the total energy per unit mass, u is the internal energy per unit mass, $\frac{1}{2}U^2$ represents kinetic energy per unit mass, gz represents potential energy per unit mass, $\dot{Q}_{cv}$ is the net rate at which energy is added to the system as heat, $\dot{W}_{cv}$ is the net rate at which work is done by the system, and g is the gravitational acceleration. Total energy (E) equals the sum of the internal energy, the kinetic energy, and potential energy. For steady-state steady flow conditions, the time rate of energy storage drops out and Equation (2.20) is simplified to

$$\left(\iint \left(\frac{P}{\rho} + e\right)\rho\left(\vec{U}\cdot\hat{n}\right)dA\right)_{cs} = \dot{Q}_{cv} - \dot{W}_{cv} \tag{2.22}$$

In order to simplify the above equation, the flow work per unit mass ($\mathrm{P}v$) and the internal energy per unit mass (u) are often combined by introducing the thermodynamic property enthalpy. The enthalpy per unit mass is given as

$$h = Pv + u \tag{2.23}$$

Using Equation (2.23) and (2.21) to modify the expression for $\frac{P}{\rho} + e$ in Equation (2.22), results in,

$$\left(\iint \left(h + \frac{1}{2}U^2 + gz\right) \rho \left(\vec{U} \cdot \hat{n}\right) dA\right)_{cs} = \dot{Q}_{cv} - \dot{W}_{cv} \tag{2.24}$$

For a steady flow with uniform velocities and the assumption that the system has adiabatic walls and there is no work (by friction), Equation (2.24) simplifies to

$$(\rho UA)_2\left(h_2 + \frac{1}{2}U_2^2 + gz_2\right) - (\rho UA)_1\left(h_1 + \frac{1}{2}U_1^2 + gz_1\right) = 0 \tag{2.25}$$

Since ρUA represents the mass flow rate ($\dot{m}$), and in steady flow conditions mass flow rates at the inlet and outlet are equal, Equation (2.25) simplifies further to

$$\left(h_2 + \frac{1}{2}U_2^2 + gz_2\right) = \left(h_1 + \frac{1}{2}U_1^2 + gz_1\right) \tag{2.26}$$

2.2 Homogeneous Equilibrium Model (HEM)

The conservation equations were derived for single-phase flow in the previous section. There are different models to describe the characteristics of the two-phase flow in nozzles. One of these models, the homogenous equilibrium model (HEM), will be used to develop an integral form of the conservation equations applied to the control volume shown in Figure 2.1. The mass, momentum, and energy equations can be modified from the previous section using the homogenous equilibrium model with two main assumptions. The first assumption states that the flow is in thermal equilibrium, where the temperature and pressure of the liquid and gas phases are the same at any given location and assumed to be at saturation conditions. The second assumption states that the flow is in mechanical equilibrium where both liquid and gas phases are traveling with the same velocity. In the HEM, the flow quality (Q) and the void fraction (α) of the fluid are defined as

$$Q = \frac{\dot{m}_g}{\dot{m}} = \frac{\dot{m} - \dot{m}_f}{\dot{m}} = 1 - \frac{\dot{m}_f}{\dot{m}} \tag{2.27}$$

$$\alpha = \frac{A_g}{A} = 1 - \frac{A_f}{A} \tag{2.28}$$

where A is the total cross-sectional area and the notations g and f refers to the separate gas and the liquid states. The gas and liquid densities can be related to the mixture density (ρ) in terms of quality (Q) or void fraction (α) as follows:

$$\rho = \left(\frac{Q}{\rho_g} + \frac{1-Q}{\rho_f}\right)^{-1} = \rho_f(1-\alpha) + \rho_g\alpha \tag{2.29}$$

Including the separate gas and liquid phases in the conservation of mass represented by Equation (2.6) and (2.8), yields

$$\dot{m}_{2,g} + \dot{m}_{2,f} = \dot{m}_{1,g} + \dot{m}_{1,f} \tag{2.30}$$

which, in terms of the separate phase velocities, can also be represented as

$$(\rho UA)_{2,g} + (\rho UA)_{2,f} = (\rho UA)_{1,g} + (\rho UA)_{1,f} \tag{2.31}$$

Using the mechanical equilibrium (no slip) assumption, i.e., both liquid and gas phases flow at the same speed, $U_g = U_f = U$, and assuming two-phase flow conditions are present at both inlet and outlet, Equation (2.31) reduces to

$$U_2\left[(\rho A)_{2,g} + (\rho A)_{2,f}\right] = U_1\left[(\rho A)_{1,g} + (\rho A)_{1,f}\right] \tag{2.32}$$

Dividing by the total cross-sectional area (A) and introducing the expression for mixture density shown in Equation (2.29) involving the void fraction into Equation (2.32), yields

$$U_2\left[\rho_{2,g}\alpha + \rho_{2,f}(1-\alpha)\right] = U_1\left[\rho_{1,g}\alpha + \rho_{1,f}(1-\alpha)\right] \tag{2.33}$$

The conservation of energy equation can be modified by substituting the definition of quality from Equation (2.27) into Equation (2.25) where the mass flow rate is constant, yielding,

$$h_{2,g}Q_2 + h_{2,f}(1-Q_2) + \frac{1}{2}U_2^2 + gz_2 = h_{1,g}Q_1 + h_{1,f}(1-Q_1) + \tfrac{1}{2}U_1^2 + gz_1 \tag{2.34}$$

The HEM will be used in the nozzle analysis in the next chapter. It will be applied to different sections in the nozzle throughout the analysis.

2.2.1 Two-Phase Flow Model

As mentioned earlier in the first chapter, the term two-phase flow refers to the two different phases of fluid flow with common interfaces in a channel or duct. Each phase has its own mass fraction for liquid and gas, and its own thermodynamic properties at a prescribed temperature. Two-phase flow occurs in the diverging section of the converging-diverging nozzle under investigation as part of the current research. Figure 2.1 shows a control volume in a diverging section of a nozzle. A simple analysis of the two-phase flow is implemented for the given control volume, using the mass, momentum, and energy equations as well as the second law of thermodynamics, to obtain expressions for the variation of pressure and velocity as a function of the variation of area within the nozzle. For analysis of the two-phase equation, assumptions include one dimensional, steady state, and adiabatic compressible flow throughout the diverging section of the nozzle.

The differential formulations are very important in explaining the expected behavior of the pressure in the diverging section of a nozzle. Applying the conservation of mass to the control volume in the diverging section of the nozzle shown in Figure 2.1 and identifying the limits with respect to axial locations as z and $z + \Delta z$, yields

$$\lim_{\Delta z \to 0} \left(\frac{(\rho UA)_z - (\rho UA)_{z+\Delta z}}{\Delta z} \right) = -\frac{d}{dz}(\rho UA) = 0 \tag{2.35}$$

Differentiating Equation (2.35), dividing all terms by ρUA, and rearranging yields

$$\frac{d\rho}{\rho} + \frac{dA}{A} + \frac{dU}{U} = 0 \tag{2.36}$$

where ρ is the mixture density, A is the total cross-sectional area, and U is the mixture velocity. Equation (2.36) shows the differential form of the conservation of mass derived for constant mass flow rate. Applying the momentum principle from Equation (2.18) to the fluid between z

and $z + \Delta z$, dividing by Δz in the diverging section, and assuming only pressure forces acting on the walls, yields

$$\frac{P_z A_z - P_{z+\Delta z} A_{z+\Delta z}}{\Delta z} + \frac{1}{\Delta z}\int_z^{z+\Delta z} P\, dA = \frac{\dot{m}\,(U_{z+\Delta z} - U_z)}{\Delta z} \tag{2.37}$$

The second term on the left-hand side of the Equation (2.37) can be simplified in the limit as Δz → 0 using the mean value theorem, which states

$$\frac{1}{\Delta z}\int_z^{z+\Delta z} f(z)dz = f(z) \tag{2.38}$$

Therefore, in the limit as Δz → 0,

$$\frac{1}{\Delta z}\int_z^{z+\Delta z} P\, dA = \frac{1}{\Delta z}\int_z^{z+\Delta z} \frac{P dA}{dz} dz = P\frac{dA}{dz} \tag{2.39}$$

Substituting Equation (2.39) into (2.37) and taking the limit as $\Delta z \rightarrow 0$, yields the following differential expression:

$$-\frac{d}{dz}(PA) + P\,\frac{dA}{dz} = \rho U A \frac{dU}{dz} \tag{2.40}$$

Differentiating the first term in Equation (2.40), simplifying, and dividing by the area, yields

$$-\frac{dP}{dz} = \rho U \frac{dU}{dz} \tag{2.41}$$

Next, the conservation of energy is applied to a similar control volume in the diverging section to find a relation for the enthalpy changes in the flowing stream. Assuming one-dimensional steady state, adiabatic flow, with no gravitational effects for the control volume, and subscripts 1 and 2 refer to z and $z + \Delta z$, Equation (2.26) becomes

$$\left(h+\frac{1}{2}U^2\right)_z = \left(h+\frac{1}{2}U^2\right)_{z+\Delta z} \tag{2.42}$$

Dividing Equation (2.42) by Δz and rearranging takes the form

$$\frac{h_z - h_{z+\Delta z}}{\Delta z} + \frac{\frac{1}{2}(U_z)^2 - \frac{1}{2}(U_{z+\Delta z})^2}{\Delta z} = 0 \tag{2.43}$$

Taking the limit as $\Delta z \rightarrow 0$ yields the following differential expression:

$$\frac{d}{dz}\left(h+\frac{U^2}{2}\right) = 0 \tag{2.44}$$

By integrating Equation (2.44) with respect to z and evaluating the constant of integration at the stagnation point, yields

$$h+\frac{U^2}{2} = h_0 \tag{2.45}$$

where h_0 is the stagnation enthalpy. In differential form, Equation (2.45) can be written as

$$dh = -U\,dU \tag{2.46}$$

To find an expression for $\frac{dU}{U}$ and $\frac{dA}{A}$ in Equation (2.36), start by differentiating Equation (2.23), resulting in

$$dh = Pdv + vdP + du \tag{2.47}$$

Recall from the Maxwell relations,

$$du = Tds - Pdv \tag{2.48}$$

Substituting Equation (2.48) in (2.47) and assuming that the flow is reversible and adiabatic (isentropic), the entropy increase in the fluid in the direction of the flow due to fluid friction in adiabatic flow approaches zero; therefore, Equation (2.47) becomes

$$dh = \ vdP = \frac{dP}{\rho} \tag{2.49}$$

Substituting Equation (2.49) into (2.46)and dividing by U^2, yields an expression for $\frac{dU}{U}$

$$\frac{dU}{U} = -\frac{1}{U^2}\frac{dP}{\rho} \tag{2.50}$$

Finally, substituting Equation (2.50) into (2.36), yields

$$\frac{dA}{A} = \frac{1}{U^2}\frac{dP}{\rho} - \frac{d\rho}{\rho} \tag{2.51}$$

Equation (2.51) can be rearranged since the flow is isentropic, yielding

$$\frac{dA}{A} = \frac{dP}{\rho}\left(\frac{1}{U^2} - \left(\frac{d\rho}{dP}\right)_s\right) \tag{2.52}$$

The speed of sound, as derived by Wallis [14] as a function of pressure and density, is given by

$$c = \left(\frac{\partial p}{\partial \rho}\right)_s^{\frac{1}{2}} \tag{2.53}$$

Therefore, substituting Equation (2.53) into (2.52), yields the following expression for $\frac{dA}{A}$ in terms of velocity and speed of sound

$$\frac{dA}{A} = \frac{dP}{\rho}\left(\frac{1}{U^2} - \frac{1}{c^2}\right) \tag{2.54}$$

The relationship in compressible flow known as the Mach number will now be introduced into Equation (2.54). The Mach number is defined as the ratio of the local speed of the fluid to the local speed of the sound and may be expressed as

$$M = \frac{U}{c} \tag{2.55}$$

where c is the local speed of sound in the flowing fluid. Combining Equation (2.54) and (2.55) results in the following expressions for the pressure variation in the diverging section with respect to distance and area:

$$\frac{dP}{dA} = \frac{\rho U^2}{A[1-M^2]} \tag{2.56}$$

and

$$\frac{dP}{dz} = \frac{\rho U^2}{A[1-M^2]} \quad \frac{dA}{dz} \tag{2.57}$$

where U is the velocity, ρ is the mixture density, and A is the area at any given value of distance z away from the throat in the diverging section. Substituting Equation (2.57) into (2.41) yields the following expressions for the velocity variation in the diverging section with respect to distance and area:

$$\frac{dU}{dA} = -\frac{U}{A[1-M^2]} \tag{2.58}$$

Or equivalently,

$$\frac{dU}{dz} = -\frac{U}{A[1-M^2]}\ \frac{dA}{dz} \tag{2.59}$$

In the next chapter, the expressions represented by Equations (2.56) - (2.59) will be used in describing the physics of the pressure distribution in a one-dimensional analysis of cavitating two-phase flow in the diverging section of a nozzle. The characteristics of the flow are controlled by the Mach number (M). In a two-phase flow in the diverging section of the nozzle, if the Mach number is less than one, a subsonic flow develops and the pressure increases with respect to area or distance. On the other hand, if the Mach number is greater than one, a supersonic flow develops and the pressure decreases with respect to area or distance. This behavior is similar to that of single-phase compressible flow discussed by Munson et al [30].

Chapter 3 - Model and Techniques

The modeling of water flow through a converging-diverging nozzle will be discussed in this chapter. Numerical models will be used to evaluate water flow through different sections of the nozzle as part of developing a complete model for the fluid flow in the converging-diverging nozzle. This model will predict the pressure distribution throughout the nozzle including single-phase in the converging section, two-phase in the diverging section, and when the cavitation phenomena occurs.

Figure 3.1 shows a schematic diagram of water flow through a converging-diverging nozzle. The flow has a finite inlet velocity where P_0 is the stagnation pressure, representing the pressure in a large upstream reservoir. Water enters the nozzle at a constant mass flow rate, $\dot{m}$, with an inlet pressure slightly lower than the stagnation pressure, P_{in}, and flows from the left to the right exiting with an outlet pressure, P_{out}. Figure 3.2 shows the pressure distribution as a function of cross-sectional area throughout the converging-diverging nozzle. Due to the pressure difference between the inlet and outlet, the fully liquid water flow accelerates in the converging section of the nozzle with decreasing pressure until it reaches the throat, achieving the maximum speed and minimum pressure at a location downstream of the throat due to the "Vena Contracta" effect. Figure 3.2 shows that four different cases may occur after the pressure in the nozzle reaches a minimum at the minimum "Vena Contracta" area. In the lowest flow case, Case 0, the pressure increases downstream of the throat throughout the diverging section, the fluid exits as single-phase liquid, and the outlet pressure ideally approaches the same value as backpressure in the absence of significant friction effects. Note that the outlet pressure will be somewhat lower than the backpressure, which signifies the pressure in a downstream reservoir, since there is a finite outlet velocity. Case 1 shows the limiting case for single-phase pressure distribution, where the flow is completely subsonic throughout the nozzle. As the backpressure is lowered further, and if the pressure at the Vena Contracta reduces sufficiently, cavitation and two-phase flow will initiate just downstream of the throat. Depending on the Mach number of the two-phase fluid flow just after initiation of cavitation, the flow will either go subsonic, as in case 2, or supersonic, as in case 3. In case 2, a subsonic two-phase condition

occurs, corresponding to a Mach number less than one, and the flow decelerates and continuously condenses back to liquid with increasing pressure in the diverging section, subsequently exiting the nozzle at a pressure lower than the inlet pressure. In the third case, a supersonic flow is shown to take place if the backpressure is lowered enough, and the flow will continue to accelerate in the diverging section with decreasing pressure until a condensation shock occurs, where there is a sudden jump in pressure and the flow decelerates to subsonic speed and condenses back to liquid throughout the remainder of the diverging section. If the backpressure is lowered even more, the supersonic region may extend throughout the diverging section of the nozzle without experiencing a condensation shock. Each case will be explained in detail later in this chapter.

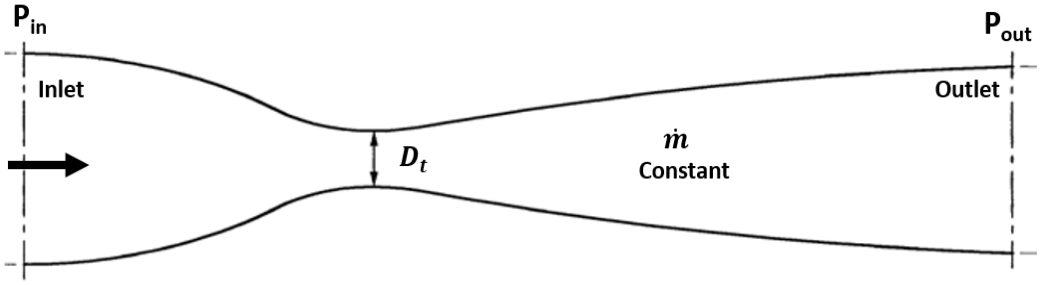

Figure 3.1 Overview of water flow through a converging-diverging nozzle.

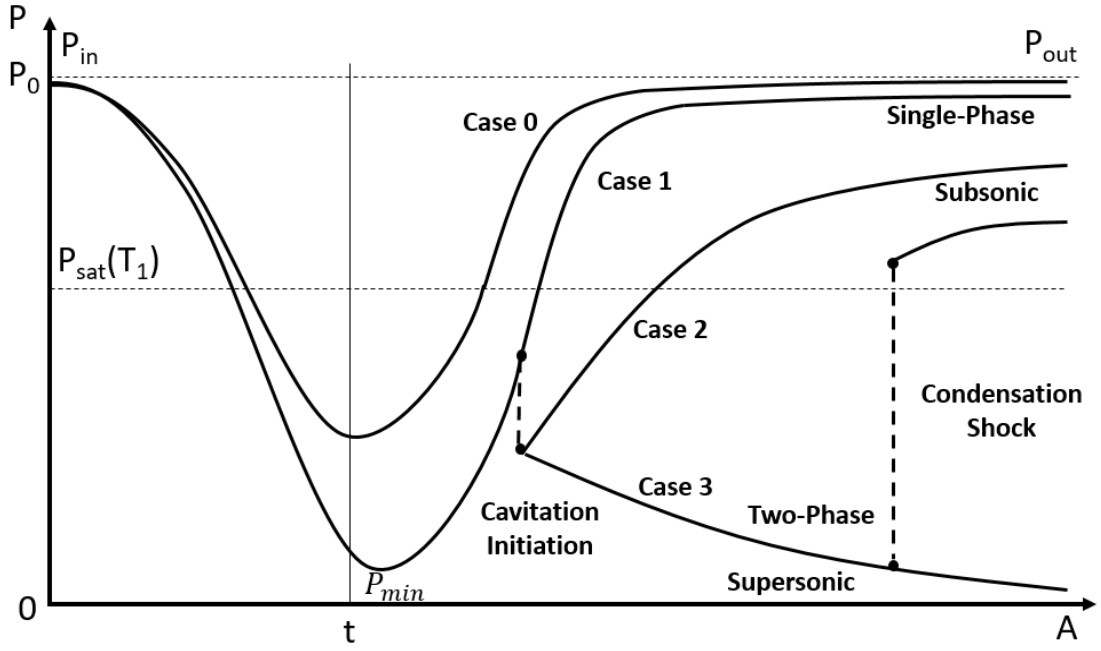

Figure 3.2 Overview of pressure distribution as a function of area for a water flow in a converging diverging nozzle

This chapter will introduce the nozzle configuration used in the model, the single-phase model, the flash inception model, predictions where cavitation initiates, the flash cavitation wave showing the behavior of the flow after the flash in the supersonic region, and modeling of the length of the two-phase region along with the location of the condensation shock.

3.1 Nozzle Configuration

The geometry of the nozzle used in this research was modeled after the geometry of the nozzle used by Ahmed [23]. The model geometry was described by implementing two 5th order polynomial fits to the dimensions of the glass nozzle used in the associated experimental set up by Ahmed [23]. This consisted of separating the nozzle radius distribution into two sections, a 5th order converging section and a 5th order diverging section, to create the desired shape of the geometry of the glass nozzle.

The resulting converging-diverging nozzle has both an inlet and an outlet diameter of 9.3 mm, a converging section with a length of 25 mm up to the throat, a diverging section with a length of 73 mm to the outlet of the nozzle, and a nozzle throat with a diameter of 1.7 mm. Figure 3.3 shows the nozzle geometry in terms of the radius as a function of axial distance, z, in millimeters. The converging section size is depicted along the negative z-axis, where z_{in} is located at - 25 mm, the diverging section is shown along the positive z-axis, where z_{out} is located at 73 mm, and the throat is located at a z location of 0 mm. This nozzle geometry will be used for all modeling of the cavitation analysis associated with this research project.

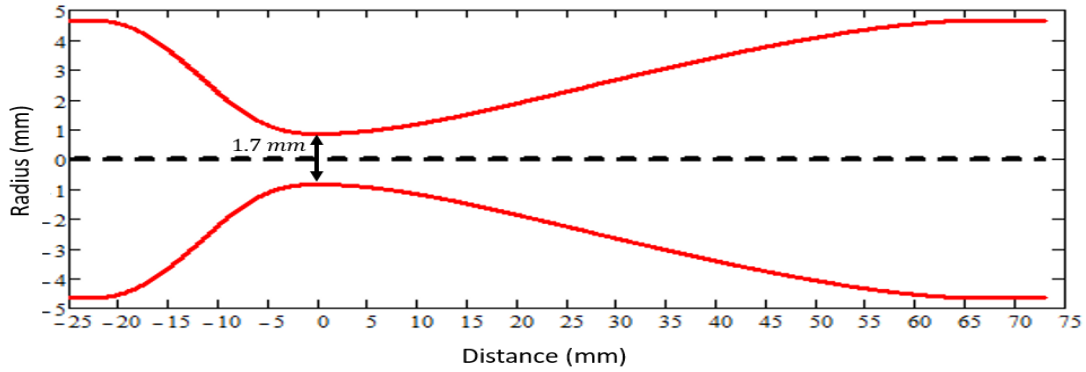

Figure 3.3 Nozzle geometry in terms of radius (mm) as function of distance (mm)

3.1.1 Pressure Evaluation (Single-Phase)

The first step in the nozzle flow modeling is estimating the pressure behavior associated with single-phase flow. Evaluating the pressure distribution as a function of axial distance or cross-sectional area is one of the most important aspects in this research. For simplicity, a single-phase, one-dimensional, water flow through the converging-diverging nozzle is investigated, while ignoring gravitational effects. The mechanical energy balance is used to evaluate the pressure distribution throughout the nozzle. The pressure distribution is calculated for two cases, 1) excluding frictional losses (frictionless) and 2) including single-phase frictional losses. The energy balance is expressed as a function of distance (z) in the nozzle with the properties evaluated at temperature (T). The energy balance is used to solve for the single-phase condition throughout converging-diverging nozzle for both frictionless and the frictional cases. Starting with the energy balance applied between the inlet denoted by the symbol "in" and at any z location within the nozzle, yields

$$P_{in} + \frac{1}{2}\rho_f U_{in}^2 = P_z + \frac{1}{2}\rho_f U_z^2 + \rho_f g H \tag{3.1}$$

where P_{in} and $U_{in}$are the inlet pressure and velocity, P_z and U_z are the pressure and velocity at a location z in the nozzle, $\rho_f$is the liquid density at the given temperature, U is the local mean velocity, g is the gravitational acceleration, and H is the head loss associated with the frictional case. The last term in Equation (3.1) is defined as the frictional pressure drop given by

$$\rho_f g H = \Delta P_{friction}(z,T) = \int_{z_{in}}^{z} \frac{1}{2}\frac{\rho_f(T)\, U_z^2 f_D}{D_z}\, dz \tag{3.2}$$

where $\Delta P_{friction}(z,T)$ is the pressure drop in the nozzle due to friction and z_{in} is the axial position of the nozzle inlet. For simplicity, the pressure drop is approximated by the integration of frictional pipe flow pressure drop. Here f_D is the Darcy friction factor in terms of Reynold's number (Re) for fully developed turbulent flow given by Equation (1.12), U_z is the local average velocity and D_z is the local diameter at any z location in the nozzle. Using the conservation of mass from Chapter 2 given in Equation (2.7), the mean velocity, U_m , can be written as

$$U_m = \frac{\dot{m}}{\rho_f A} \tag{3.3}$$

Substituting U_m from Equation (3.3) into Equation (3.1), and using the mass flux expression, $G = \frac{\dot{m}}{A}$, one obtains equations for pressure at any location throughout the nozzle for both the frictionless and frictional cases as follows:

$$P(z,T) = P_{in} + \frac{G_{in}^2}{2\rho_f(T)} - \frac{G_z^2}{2\rho_f(T)} \tag{3.4}$$

$$P_{friction}(z,T) = P_{in} + \frac{G_{in}^2}{2\rho_f(T)} - \frac{G_z^2}{2\rho_f(T)} + \Delta P_{friction}(z,T) \tag{3.5}$$

where G_{in} is the inlet mass flux and G_z is the local mass flux at a location z in the nozzle. Equation (3.4) and Equation (3.5) are for the frictionless and frictional cases, respectively.

The simple model developed for calculating the single-phase pressure distribution, represented by Equation (3.4) and Equation (3.5), can be validated by comparing it to previous single-phase water flow experimental data. Steady-state experimental pressure data was measured by Gallman [24] for water flowing through a converging-diverging nozzle. Note that the model does not account for two-phase frictional pressure drop effects, separation, and the "Vena Contracta" effect. Therefore, it only provides an estimate of the single-phase flow through the converging-diverging nozzle for comparison with the experimental pressure data. Pressure data for water conditions with an inlet temperature of 20℃ and a backpressure of 43.2 kPa are given in Table 1-2 for 8 pressure taps. The nozzle geometry was modeled from 5th order polynomials for the converging and diverging sections of the nozzle shown in Figure 3.3. Figure 3.5 shows the comparison of the calculated single-phase pressure distribution for the frictionless and frictional cases and the measured data by Gallman [24] for a temperature of 20℃. The solid vertical line in Figure 3.5 indicates the location of the throat in the nozzle, and the corresponding pressure tap location. The calculated model shows good predictions of the pressure distribution for the single-phase flow in the converging section of the nozzle up to the throat at location 0, tap 4. The model prediction in the diverging section of the nozzle was not

as accurate as expected because two-phase flow, not accounted for in the prediction model, was observed by Gallman [24] to initiate somewhat downstream of the throat.

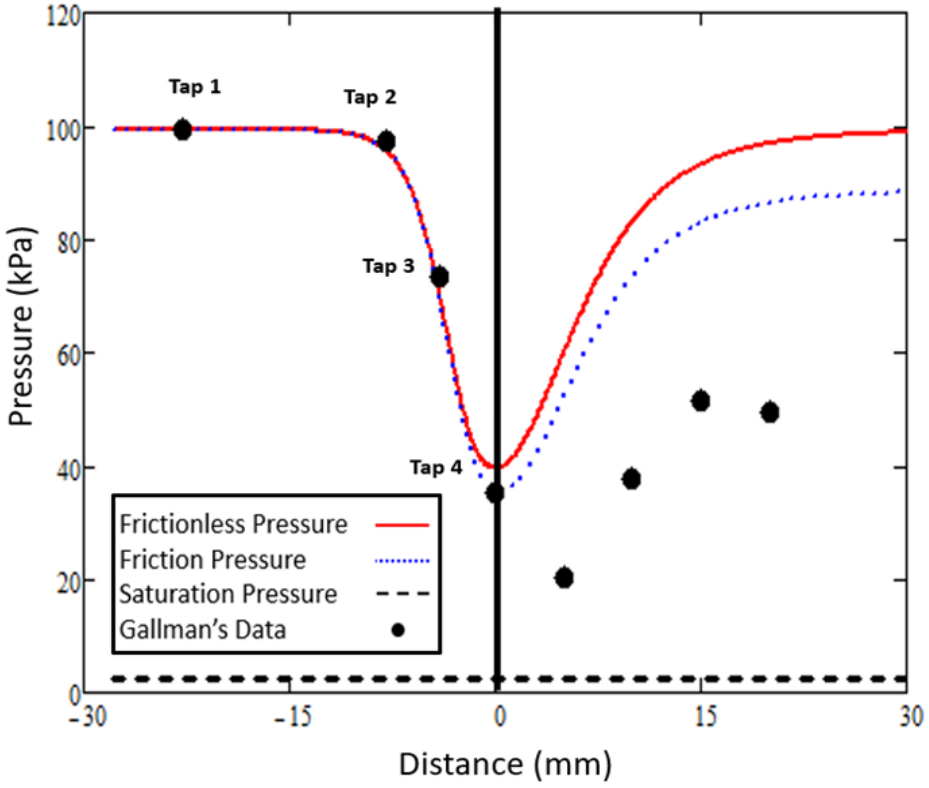

Figure 3.4 Comparisons of the single-phase calculated pressure distribution and the measured data by Gallman [24] for a temperature of 20℃

After validating the single-phase pressure distribution prediction model with the experimental data given by Gallman [24], it was used to predict the pressure distribution for other nozzles under similar conditions. Note that in the diverging section this model represents an extrapolation of the single-phase model, and therefore is not expected to accurately predict in the two-phase flow region downstream of the throat.

The single-phase pressure distribution prediction models were used for Ahmed's data [23]. This data consisted of experimental tests using water flowing in a glass converging-diverging nozzle for different temperatures of 70 ℃, 50 ℃, and 25 ℃. Table 1-1 shows the water inlet pressure and mass flow rate for the three different temperatures. The glass nozzle did not have any pressure taps. Therefore, in the absence of direct measurements, the pressure

distribution models for frictionless and frictional flows were applied to the experimental tests conditions of Ahmad [23] to predict the pressure distribution through the converging-diverging nozzle. The cross-sectional area at any location can be calculated using the mass flow rate and the nozzle geometry shown in Figure 3.3. Using Equation (3.4) and Equation (3.5), and the given and calculated parameters, the different pressure distributions were calculated and compared for water associated with single-phase liquid flow in the converging-diverging nozzle. The comparison of water results for the throat pressure and the outlet pressure are shown for the frictionless and frictional cases in Table 3-1 and Table 3-2, respectively. Each Table shows the given parameters (including the fluid temperature, the mass flow rate, and the inlet pressure), and the calculated parameters (including throat pressure and the outlet pressure determined using Equation (3.4) and Equation (3.5)). The outlet pressures were calculated at the exit of the diverging section of the nozzle. Also, comparison of both frictional and frictionless cases for the three different temperatures of 70 ℃, 50 ℃, and 25 ℃ are shown in Figure 3.5, Figure 3.6, and Figure 3.7, respectively.

Table 3-1 Calculated single-phase water data in a converging-diverging nozzle for the frictionless case for three different temperatures

Given				Calculated		
Fluid Temperature	**Saturation Pressure**	**Inlet Pressure**	**Mass Flowrate**	**Throat Pressure**	**Outlet Pressure**	$P_{sat} - P_{throat}$
(℃)	(kPa)	(kPa)	(kg/s)	(kPa)	(kPa)	(kPa)
25	3.17	102	0.0349	-17.4	102	20.5
50	12.4	102	0.0336	-9.43	102	21.8
70	31.2	102	0.0306	9.16	102	22

Table 3-2 Calculated single-phase water data in a converging-diverging nozzle for the frictional case for three different temperatures

Given				Calculated		
Fluid Temperature	**Saturation Pressure**	**Inlet Pressure**	**Mass Flowrate**	**Throat Pressure**	**Outlet Pressure**	$P_{sat} - P_{throat}$
(℃)	(kPa)	(kPa)	(kg/s)	(kPa)	(kPa)	(kPa)
25	3.17	102	0.0349	-23.1	83.2	26.3
50	12.4	102	0.0336	-14.3	86.2	26.7
70	31.2	102	0.0306	4.74	89.5	26.5

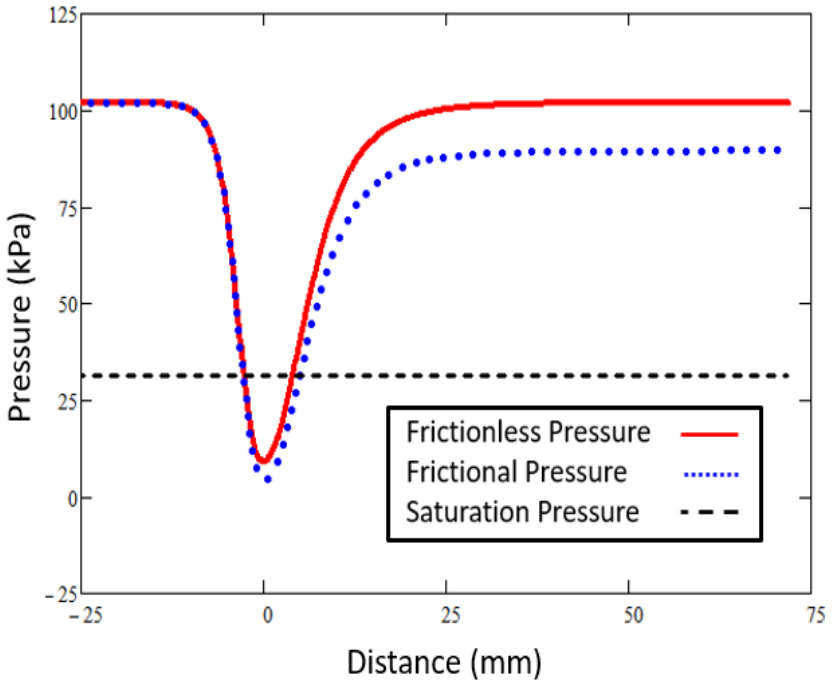

Figure 3.5 Single-phase pressure distribution for water flowing through converging-diverging nozzle at 70 ℃

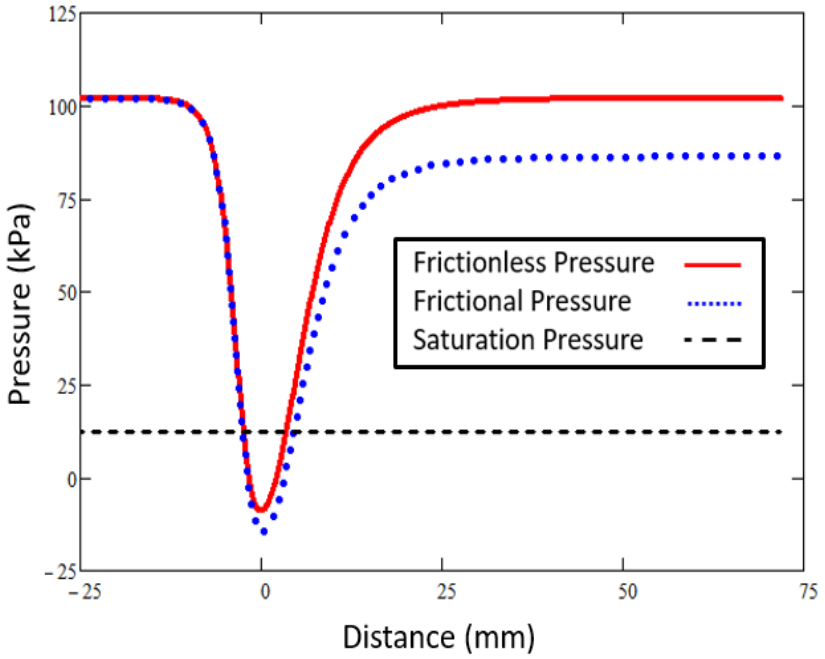

Figure 3.6 Single-phase pressure distribution for water flowing through converging-diverging nozzle at 50 ℃

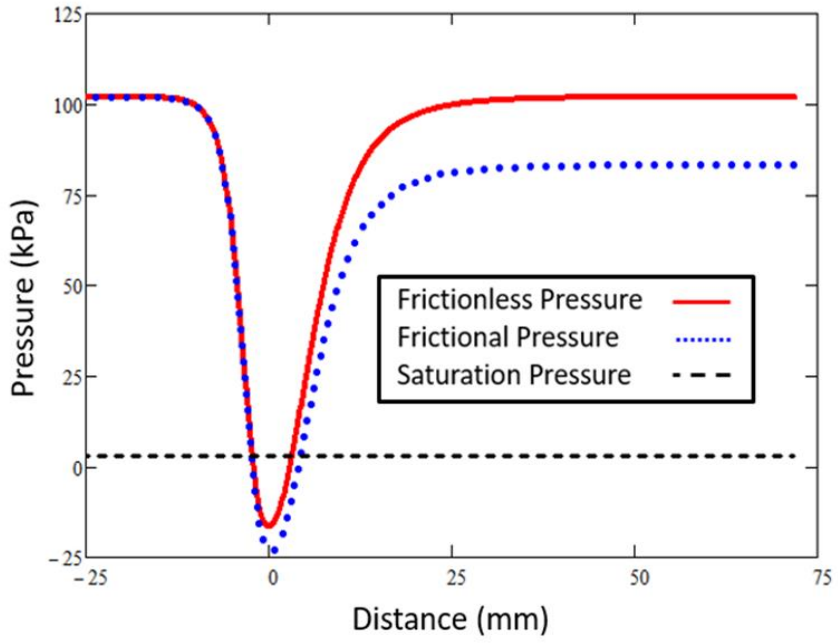

Figure 3.7 Single-phase pressure distribution for water flowing through converging-diverging nozzle at 25 ℃

In the frictionless case, the outlet pressure approaches the same value as the inlet pressure; however, for the frictional case, the outlet pressure is at a lower value than the inlet pressure due to pressure drop (i.e., head loss) caused by friction. Also, the pressure distribution for the 50 ℃ and 25 ℃ cases is seen to drop to negative values below the corresponding saturation pressure as the fluid approaches the throat. Then, downstream it increases above the saturation pressure and subsequently reaches the exit pressure. These calculated negative pressures suggest that the flow is under tension around 2 mm upstream of the throat, and the fluid continues to be in tension (negative absolute pressure) up to 3 mm downstream of the throat for both 50 ℃ and 25 ℃ temperatures. The pressure distribution is seen to cross the saturation pressure at approximately the same distance from the throat, regardless of the temperature. This corresponds to about 4.4 mm downstream of the throat for all three temperature cases. This estimation does not include the "Vena Contracta" effect. As shown in both Table 3-1 and Table 3-2, the difference between the saturation pressure and the calculated throat pressure has an approximately constant value of about 22 kPa for all temperatures in the frictionless case, and an approximately constant value of 26.5 kPa for all temperatures in the frictional case; i.e., for the case where frictional effects are taken into account.

3.2 Flash Inception Analysis

The main goal of this section is to present the analysis to predict the flash inception point for a given flow conditions. When the single-phase liquid is decompressed and put under sufficient tension near the throat of the nozzle, the fluid has been observed to produce an audible "snap," and vaporizes, "flashing" into a two-phase mixture [27]. Understanding this phase transition from single-phase liquid to a two-phase mixture is necessary to explain the physical process that occurs in the diverging section of a converging-diverging nozzle. Predicting this point of flash and its onset conditions will be the first step in determining subsequent behavior of the two-phase flow in the diverging section of the converging-diverging nozzle. Figure 3.8 shows an overview of the pressure distribution behavior in the nozzle up to the flash inception point. The pressure distribution is calculated, as mentioned earlier, using the single-phase pressure drop up to the point of the flash. After the flash initiation, the flow develops into two-phase flow, which requires a two-phase pressure drop model for calculations. This will be explained in detail in the next section of this chapter.

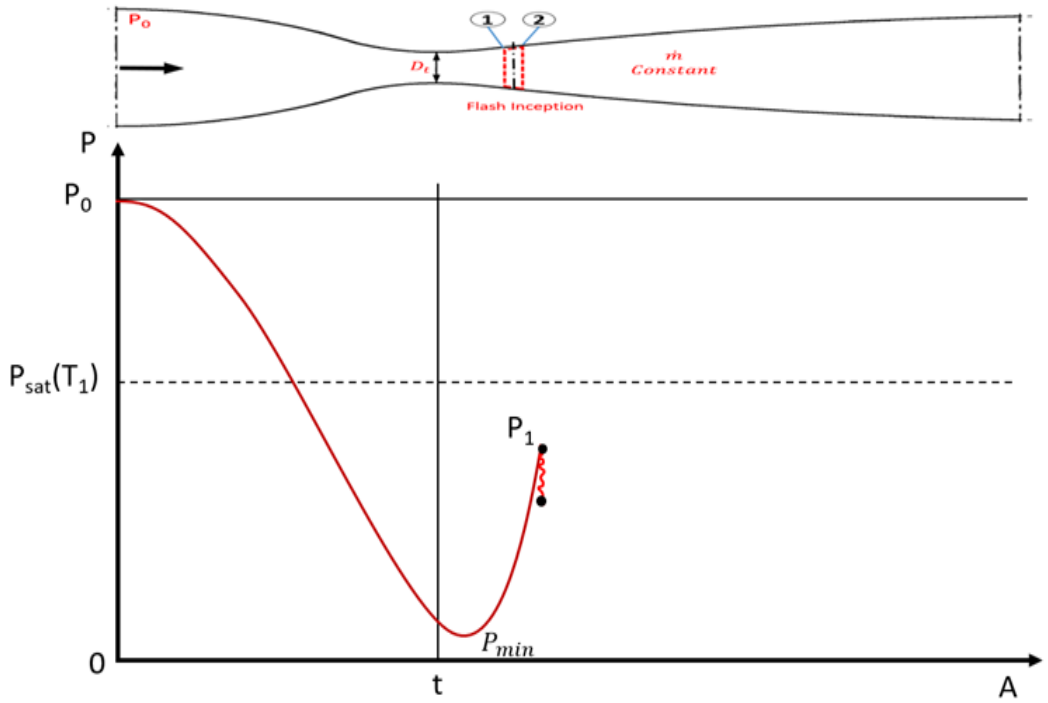

Figure 3.8 Overview of pressure vs. area depicting the flash inception point

The upcoming section 3.2.1 will introduce the importance of calculating the depressurization rate used in the analysis of the "dynamic flash inception line" for steady flows through pipes and nozzles and the analysis of the "modified dynamic flash inception line" for steady flow through converging-diverging nozzles.

3.2.1 Rate of Depressurization

The depressurization rate is very important for the calculation of the flash inception lines. It is defined as the rate of change of pressure with respect to time. The depressurization rate[1] is introduced using a Lagrangian frame of reference experienced by a fluid particle flowing through the converging-diverging nozzle. Depending on the inlet conditions, for a steady flow or a transient flow, the rate of depressurization can be evaluated using Equation (1.28). We start evaluating the rate of change of pressure with respect to time by assuming initially a subcooled water entering the converging-diverging nozzle. The rate of pressure change with respect to time will increase as the area decreases when the fluid is moving in the converging section of the nozzle up to the throat. The rate of depressurization in the converging section up of a nozzle to near the throat can be calculated using Equation (3.6)

$$\frac{dP}{dt} = \frac{\dot{m}^3}{\rho_f^2 A^4}\frac{dA}{dz} \tag{3.6}$$

Having an accurate estimation of the rate of change of pressure with respect to distance is also very important in this evaluation. As the flow approaches the throat, $\frac{dP}{dz}$ is almost zero; however, a small distance away from the throat there is a significant steepness in the slope given by $\frac{dP}{dz}$. In terms of $\frac{dP}{dz}$, the equation for $\frac{dP}{dt}$ can thus be written as,

[1] In flowing flows the total depressurization rate is really the substantial derivative, $\frac{DP}{Dt} = \frac{\partial P}{\partial t}\Big]_z + U\frac{\partial P}{\partial z}\Big]_t$

$$\frac{dP}{dt} = \frac{dP}{dz}\frac{dz}{dt} \tag{3.7}$$

where,

$$\frac{dz}{dt} = \frac{\dot{m}}{\rho_f A} \tag{3.8}$$

Then, an approximation is made that the value of $\frac{dP}{dz}$ can be estimated by $\frac{\Delta P}{\Delta z}$ and calculated using numerical differentiation approximations such as the backward difference method, forward difference method, and three-point endpoint formula, respectively, as shown below

$$\frac{dP}{dz} = \frac{P_z - P_{z-\Delta z}}{\Delta z} \tag{3.9}$$

$$\frac{dP}{dz} = \frac{P_{z+\Delta z} - P_z}{\Delta z} \tag{3.10}$$

$$\frac{dP}{dz} = \frac{1}{2\Delta z}\left[3\,P_z - 4P_{z+\Delta z} + P_{z+2\Delta z}\right] \tag{3.11}$$

Where P represents the pressure, and z is a location in the nozzle and Δz is the change in the location between two corresponding pressures.

The upcoming sections 3.2.2 and 3.2.3 will introduce a “dynamic flash inception line” analysis and a “modified dynamic flash inception line” analysis for steady flow through converging-diverging nozzles.

3.2.2 Dynamic Flash Inception Line

The static flash inception line correlation given by Equation (1.26), as discussed earlier in Chapter 1, is a function of the inlet temperature and the depressurization rate. The equation is applicable to the case of fluids under static, non-flowing conditions. Understanding the implications of this equation will be important in applying the dynamic form of the equation to the conditions in the converging-diverging nozzle. The dynamic flash inception line analysis proposed herein will use the static inception line equation incorporating flow and the convective depressurization rate, yielding the resultant $\frac{dP}{dt}$. The equation is utilized to predict the pressure undershoot using the water inlet conditions for the given converging-diverging nozzle configuration. The pressure undershoot is defined as the difference between the saturation pressure and the local pressure and is a function of the depressurization rate.

A marching solution method will be utilized for evaluating the dynamic flash inception line starting from the water conditions at the inlet of the nozzle. Then, each subsequent step is evaluated using a distance increment of 0.5 mm up to the throat. The surface tension is assumed to be constant throughout the calculations. The results are shown as a plot of pressure undershoot as a function of depressurization rate. Then, the rate of depressurization for the experimental conditions is evaluated using Equation (1.28) in order to determine if the experimental data points cross above (or exceed) the flash inception line. A crossing above the threshold indicates the onset of cavitation and the flash inception predicted by the dynamic flash inception line.

3.2.3 Modified Dynamic Flash Inception Line

The modified dynamic flash inception line was introduced by Abuaf [36] combining the static flash inception correlation, Equation (1.26), and the turbulent pressure fluctuations, Equation (1.27). The modified dynamic flash inception line will be used in this research to predict the location and the conditions of the flash inception in the converging-diverging nozzle in which the analysis incorporates the turbulent pressure fluctuations, the turbulence intensity and the area ratio effects. From previous research by Jones

[26], it was shown that the depressurization rates for the static, non-flowing, experiments had considerably lower values than the depressurization rates for the dynamic, flowing, experiments. In addition to accounting for the fluid temperature and depressurization rate, the correlation given in Equation (3.12) includes the turbulence effect of the fluid and the area ratio. Addition of these two turbulence related parameters signifies the difference between a dynamic flash inception line correlation versus the modified dynamic flash inception line correlation. Applying the turbulent pressure fluctuations to Equation (1.26) will give a better prediction of the flash inception point. In the non-flowing systems, turbulence effects are absent since there is no fluid movement occurring like that in the converging-diverging nozzle. The pressure undershoot ΔP_{Fi} associated with the modified dynamic inception line is defined by

$$\Delta P_{Fi} = 0.253 \frac{\sigma^{\frac{3}{2}}}{\sqrt{kT_c}} \frac{T_R^{13.73} \sqrt{1+14\ \sum'^{0.8}}}{\left[1-\frac{v_f}{v_g}\right]} - 27(\varepsilon^2) \frac{G^2}{2\rho_f} \left(\frac{A_z}{A_{in}}\right)^{1.4} \tag{3.12}$$

where ε is the turbulence intensity, which mostly depends on the order of magnitude of the Reynolds number and surface roughness, T_c is the critical temperature, T_R is the reduced inlet temperature, A_z is the cross-sectional area at any z location, and A_{in} is the cross-sectional area at the inlet. The first term on the right hand-side of Equation (3.12) is the static inception line, given from Equation (1.26) and the second term includes the effect of turbulence intensity and the nozzle area ratio. The results are shown in Chapter 4 as calculated pressure undershoot as a function of depressurization rate, along with the experimental data points provided by Gallman [24] and Ahmed [23].

3.3 Flash "Cavitation wave"

The flash cavitation wave analysis focuses on the evaluation and conditions of the converging-diverging nozzle once the flash inception is predicted from the previous section. Pressure distributions in the two-phase region as a function of area and distance will show the physics of what occurs inside the nozzle. If the water flowing through the converging-diverging nozzle does not experience the cavitation phenomena, the fluid will continue to be single-phase liquid all the way to the exit of the nozzle. If wall friction occurs, the pressure at the exit will also be lower than the inlet pressure. Previous work [23] showed that in subcooled liquid flowing through a converging-diverging nozzle, the lowest pressure (hence, the cavitation inception flash) will occur at the throat if the flow separation and friction effects are ignored. Considering the flow separation and the associated "Vena Contracta" effect, the lowest pressure can extend downstream of the throat in the nozzle, which will affect the location of the flash inception. If flash inception occurs, two-phase mixture will continue through the diverging section.

Figure 3.9 shows an overview of the pressure distribution as a function of area in the converging-diverging nozzle for the flow after the flash occurs downstream of the throat. Two main flow fields and conditions in the diverging section of the nozzle can occur after the flash inception and will be predicted from the differential analysis developed in Chapter 2; a subsonic flow field, and a supersonic flow field both depending on the value of Mach number. Subsonic conditions refer to the flow field when the Mach number is less than one. After the flow cavitates in the diverging section to a Mach number less than one, it decelerates and causes a pressure increase past the saturation pressure, causing the flow to reach subcooled conditions at the exit of the nozzle. The second condition is the supersonic condition which is referred to the flow field when the Mach number is greater than one. After the flash, if the Mach number is supersonic, the flow will keep accelerating in the diverging section of the nozzle causing the pressure to continue dropping as the area is increasing. The flash wave analysis will focus on the supersonic case and will be explained in details

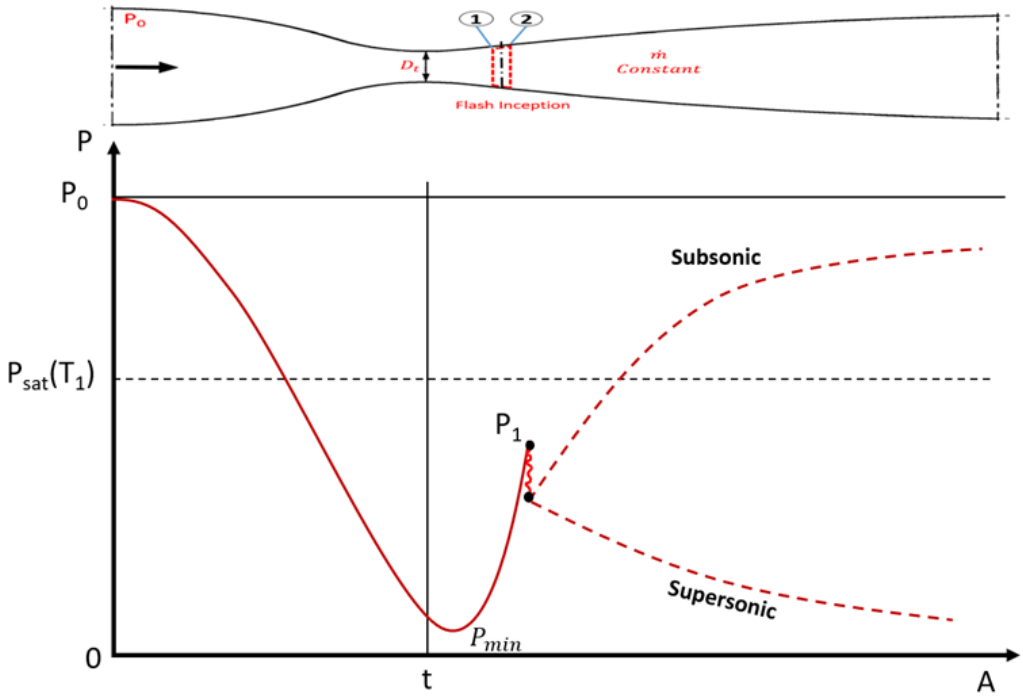

Figure 3.9 Overview of pressure as a function of area for the cavitation wave analysis in the converging-diverging nozzle.

The current section will introduce a step by step marching procedure for the evaluation of the flash wave analysis in the diverging section of the nozzle. This procedure will be detailed in the next section. The results will show the pressure distribution as a function of area in the converging-diverging nozzle. It will provide useful data to complete the evaluation flow through the nozzle.

3.3.1 Marching Procedure and Assumptions

A step-by-step marching procedure will be implemented considering a small area of control volume downstream of the throat of the converging-diverging nozzle, as shown in Figure 3.10. The marching algorithm will be developed by applying the mass, momentum, and energy conservation equations and the second law of thermodynamics to a control volume as the fluid particle moves from z to $z + \Delta z$ location in the nozzle. The number of marching points will be specified before running the program, depending on length of the diverging section of the nozzle. The more marching points used, the higher the resolution of the analysis results. The input parameters for the current marching procedure will be the results and conditions of the flash inception evaluation from section 3.2. As discussed earlier in the literature review, different models for the two-phase pressure drop, the speed of sound, and the friction factor are available for use in the calculations. By comparing the results of the marching solution with experimental data for the different models, the best model that more accurately predicts the experimental data will be identified and discussed.

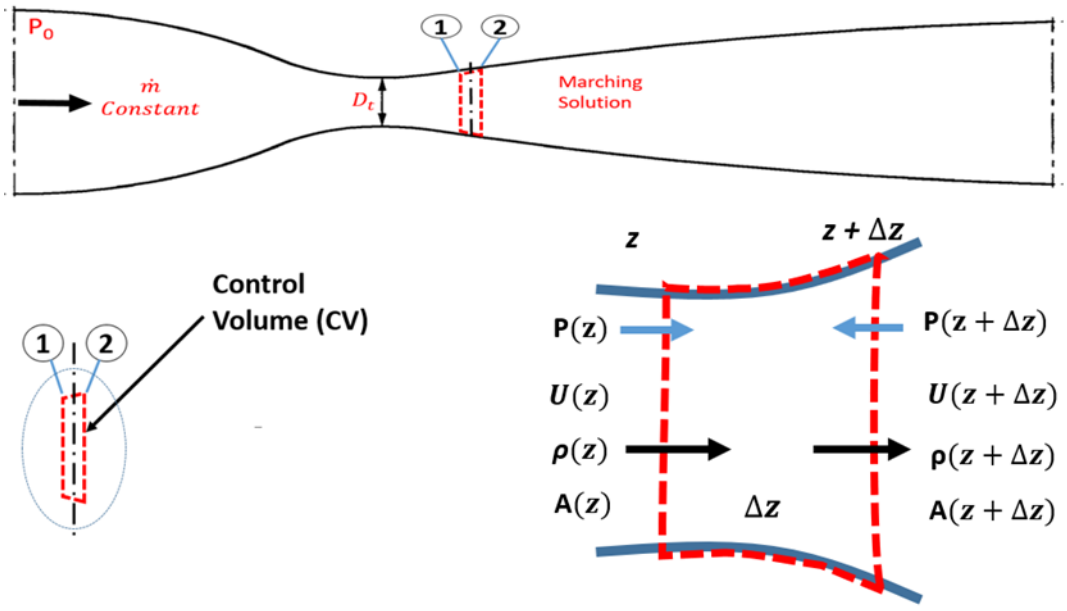

Figure 3.10 Control volume for the marching procedure for the flash wave analysis

Key assumptions are made before starting the marching procedure for the fluid flowing through the converging-diverging nozzle. Starting with a specified values of inlet pressure and inlet temperature, subcooled water is assumed to be entering the converging-diverging nozzle at a steady-state condition. The mass flow rate exiting the nozzle is assumed to be the same as the mass flow rate entering the nozzle, i.e., the mass flow rate remains constant. The assumption of constant mass flow rate and incompressible fluid results in the mean velocity being the highest at the location of the minimum area; i.e., at the throat. Introducing wall friction and flow separation in the nozzle will drive the highest velocity to be downstream of the throat due to the "Vena contracta" effect. Upstream of the flash, the flow is assumed to be isentropic, reversible and adiabatic, with a metastable liquid having constant density (incompressible). Fluid properties are assumed uniform at each cross-sectional area of the nozzle but vary with each location z. If subsonic conditions occur after the flash inception, subcooled conditions are assumed the mechanical energy balance given by Equation (3.5)is used to calculate the pressure distribution through the diverging section of the nozzle. On the other hand, if supersonic conditions occur after the flash inception, the homogenous equilibrium model (HEM) is used downstream of the flash for the flow. The HEM is used to calculate the flow properties and the pressure distribution in the nozzle using the governing equations derived in Chapter 2 given by Equations (2.31) and (2.33). Comparisons of the previously mentioned two-phase frictional pressure drop models, Friedel and Lockhart and Martinelli, local speed of sound relations by Wallis and Franc, and the friction factors relationship for pipe and diffuser flows will be shown in the next chapter.

Equation (3.13) shows a solving block for the parameters evaluated at the flash, which will be used at the beginning of the marching grid analysis in the diverging section of the nozzle. The pressure and specific volume calculated at the point of the flash using the flash inception analysis are used as the input parameters into the solving block. The cross-sectional area, where the flash inception occurs, is also calculated and entered into the program as well as the value of the constant mass flow rate used in the experimental data. The flow proprieties that are calculated in the program are saturation pressure (T_{sat}), density (ρ), velocity (U), void fraction (α), quality (Q), entropy (s_i), speed of sound (a), Mach number (M), mass flux (G), and the enthalpy (h). The saturation thermodynamics properties of water are denoted by the symbol

f and g for liquid and gas, respectively. Tables from the National Institute of Standards and Technology (NIST) webbook [31] were downloaded and implemented in the associated Mathcad program to calculate saturation values for water.

$$f(P,v) = \left| \begin{array}{c} T \leftarrow T_{sat}(P) \\ \rho \leftarrow \frac{1}{v} \\ U \leftarrow \frac{\dot{m}}{\rho\, A} \\ \alpha \leftarrow \frac{\rho - \rho_f(T)}{\rho_g(T) - \rho_f(T)} \\ Q \leftarrow \frac{\rho_g(T)*\alpha}{\rho_f(T)*(1-\alpha) + \rho_g(T)*\alpha} \\ s_i \leftarrow Q s_g(T) + (1-Q) s_f(T) \\ T_{abs} \leftarrow T + 273.15\ K \\ a \leftarrow \frac{1}{\sqrt{\rho\left[\frac{\alpha}{a_g(T)^2*\rho_g(T)} + \frac{1-\alpha}{a_f(T)^2*\rho_f(T)} + \frac{(1-\alpha)\rho_f(T)C_{pl}T_{abs}}{(\rho_g(T)L)^2}\right]}} \\ M \leftarrow \frac{U}{a} \\ G \leftarrow \frac{\dot{m}}{A} \\ h \leftarrow Q h_g(T) + (1-Q) h_f(T) \end{array} \right. \tag{3.13}$$

After calculating the parameters at the flash, the marching procedure in the supersonic region for the diverging section begins. The marching solution consists of grid points denoted by the symbol j as the upstream grid point and $j + 1$ for the subsequent downstream grid point. The first grid point for starting the solving block is located at the point of the flash.

The equations describing the nozzle cross sectional area (A) and the distance (z) in the marching grid solutions are given by

$$A_{j+1} = A_j + \Delta A \tag{3.14}$$

$$z_{j+1} = z_j + \Delta z \tag{3.15}$$

The pressure variation as a function of area was derived in Chapter 2 and is given by Equation (2.56), without including the effects of friction in the evaluation. To include the friction effect, the conservation equations and second law of thermodynamics for compressible flows are implemented. Starting with the differential form of the mass conservation previously shown in Chapter 2 as Equation (2.36), and rearranging in terms of the specific volume (v) instead of the density, yields the following:

$$\frac{dv}{v} - \frac{dA}{A} - \frac{dU}{U} = 0 \tag{3.16}$$

Then, considering that the fluid does not undergo an isentropic process, and the associated entropy change is caused by friction, Equation (2.49) and (2.50) become,

$$dh = \frac{dP}{\rho} + T\,ds \tag{3.17}$$

$$\frac{dU}{U} = -\frac{1}{U^2}\frac{dP}{\rho} - \frac{T\,ds}{U^2} \tag{3.18}$$

To find an expression for $\frac{dv}{v}$, the specific volume can be considered as a function of the entropy and pressure as,

$$v = v(s, P) \tag{3.19}$$

Differentiating Equation (3.19) with respect to pressure and entropy, yields

$$dv = \left(\frac{\partial v}{\partial s}\right)_P ds + \left(\frac{\partial v}{\partial P}\right)_s dP \tag{3.20}$$

where ds is the local entropy generation for saturated two-phase fluid. The partial derivatives in Equation (3.20) can be expressed in terms of the following thermodynamic property relationships [14]:

$$\left(\frac{\partial v}{\partial s}\right)_P = \frac{\beta v T}{c_P}, \qquad \left(\frac{\partial v}{\partial P}\right)_S = -\frac{v^2}{c^2} \tag{3.21}$$

where β is the isobaric thermal expansion coefficient and defined as the rate of change in specific volume with an increase in temperature at a constant pressure as shown in Appendix (A), c_P is the local specific heat. Substituting the partial derivatives from Equation (3.21) in Equation (3.20) results in

$$\frac{dv}{v} = \frac{\beta T}{c_P} ds - \frac{v}{c^2} dP \tag{3.22}$$

Finally, substituting Equations (3.18) and (3.22) into (3.16), yields,

$$\frac{\beta T}{c_P} ds - \frac{v}{c^2} dP + \frac{v dP}{U^2} + \frac{T ds}{U^2} - \frac{dA}{A} = 0 \tag{3.23}$$

Multiplying all terms by U^2 and using the Mach number relation given by Equation (2.55), Equation (3.23) reduces to

$$(1 - M^2) v dP - U^2 \frac{dA}{A} + \left(1 + \frac{\beta U^2}{c_P}\right) T ds = 0 \tag{3.24}$$

Rearranging Equation (3.24) in terms of $\frac{dP}{dA}$, yields

$$\frac{dP}{dA} = \frac{\rho U^2}{A[1-M^2]} - \frac{T}{v} \frac{\left(1+\frac{\beta U^2}{c_P}\right)}{(1-M^2)} \frac{ds}{dA} \tag{3.25}$$

The entropy generation rate, $d\dot{S}_{gen}$ for two-phase flow is introduced from the first and second law of thermodynamics by Revellin [32] and, assuming adiabatic flow, the expression is given by

$$d\dot{S}_{gen} = \frac{\dot{m}}{\rho\, T}(dP)_{friction} \tag{3.26}$$

The entropy change (ds) can be calculated by applying the second law of thermodynamics to the control volume and assuming steady state, constant mass flow rate and adiabatic flow, yielding

$$ds = \frac{d\dot{S}_{gen}}{\dot{m}} \tag{3.27}$$

Substituting Equation (3.26) into (3.27) gives,

$$ds = \frac{1}{\rho\, T}(dP)_{friction} \tag{3.28}$$

where ρ is the two-phase mixture density and can be calculated by

$$\frac{1}{\rho} = \left[\left(\frac{Q}{\rho_g}\right) + (1 - Q)\left(\frac{1}{\rho_f}\right)\right] \tag{3.29}$$

Figure A.3 in Appendix (A) shows the evaluation of the isobaric thermal expansion coefficient for the liquid-vapor water mixture. Results conclude that the isobaric thermal expansion coefficient of the mixture is very close to the vapor thermal expansion coefficient; that is, the liquid contribution is minimal and can be ignored compared to the vapor contribution in a two-phase system. Equation (3.25) includes the term $\left(1 + \frac{\beta U^2}{c_P}\right)$, where the second term is considered negligible due to the very small values of two-phase mixture thermal expansion coefficient (β) as shown in Figure A.3. Therefore, the entire term is approximated as 1. The final equation for the variation of pressure as a function of the variation of area in the nozzle,

with varied cross-sectional area and including frictional effects, is obtained by substituting Equation (3.28) into Equation (3.25), yielding

$$\frac{dP}{dA} = \frac{\rho U^2}{A[1-M^2]} - \frac{1}{(1-M^2)}\left(\frac{dP}{dA}\right)_{friction} \tag{3.30}$$

The first term on the right-hand side represents the pressure drop due to momentum and the second term represents the pressure drop due to frictional effects. The $\left(\frac{dP}{dA}\right)_{friction}$ will be calculated using several two-phase pressures drop models for comparison purposes in Chapter 4.

Following the marching procedure steps, the total pressure drop in the nozzle, $\frac{dP}{dA}$, given in Equation (3.30) is solved numerically and used in calculating the pressure distribution in terms of the discretized points j and $j+1$ as described in Equation (3.31)

$$P_{j+1} = P_j + \left(\frac{dP}{dA}\right)_j \Delta A \tag{3.31}$$

The change in the entropy of the fluid can be expressed as

$$\Delta s = \frac{1}{\rho T}(\Delta P)_{friction} \tag{3.32}$$

The $(\Delta P)_{friction}$ is calculated from the two-phase pressures drop models, $\left(\frac{dP}{dA}\right)_{friction}$, divided by the area. Expressing Equation (3.32) in terms of the discretized points j and $j+1$, yields

$$s_{j+1} = s_j + \Delta P_{friction,j} \frac{1}{\rho_j T_j} \tag{3.33}$$

Introducing expressions for the other variables used in the marching grid solution within the nozzle, i.e., quality (Q_{j+1}), void fraction (α_{j+1}), mixture density (ρ_{j+1}), velocity (U_{j+1}), Mach number (M_{j+1}), mass flux (G_{j+1}), and enthalpy (h_{j+1}), gives

$$Q_{j+1} = \frac{s_{j+1} - s_f(T_{j+1})}{s_g(T_{j+1}) - s_f(T_{j+1})} \tag{3.34}$$

where the properties $s_g(T_{j+1})$ and $s_f(T_{j+1})$ are the saturated values of gas and liquid entropy evaluated at the new temperature (T_{j+1}).

$$\alpha_{j+1} = \frac{\rho_f(T_{j+1})\, Q_{j+1}}{\rho_g(T_{j+1})(1 - Q_{j+1}) + \rho_f(T_{j+1})\, Q_{j+1}} \tag{3.35}$$

where the properties $\rho_g(T_{j+1})$ and $\rho_f(T_{j+1})$ are the saturated values of gas and liquid density evaluated at the new temperature (T_{j+1}).

$$\rho_{j+1} = \rho_f(T_{j+1})(1 - \alpha_{j+1}) \; + \; \rho_g(T_{j+1})\alpha_{j+1} \tag{3.36}$$

$$U_{j+1} = \frac{\dot{m}}{(\rho_{j+1})(A_{j+1})} \tag{3.37}$$

$$M_{j+1} = \frac{U_{j+1}}{a_{j+1}} \tag{3.38}$$

$$G_{j+1} = \frac{\dot{m}}{A_{j+1}} \tag{3.39}$$

$$h_{j+1} = h_f(T_{j+1})(1 - \; Q_{j+1}) \; + \; h_g(T_{j+1})\, Q_{j+1} \tag{3.40}$$

3.4 The Length of Two-Phase "Condensation Shock" Region

After the flash occurs, and for the case where the inception Mach number is greater than 1, a supersonic flow accelerates in the diverging section of the nozzle causing the pressure to decrease to a point where the flow is abruptly interrupted by a condensation shock. Here the two-phase mixture converts back to a single-phase liquid through the remainder of the diverging section of the nozzle. The condensation shock is considered to be a spontaneous and abrupt change in the flow that occurs in the diverging section of the nozzle. This change usually happens when the flow immediately after the flash is moving at supersonic speeds. The distance from the flash inception to the condensation shock is referred to as the length of two-phase region. Analysis of the length of two-phase region in the converging-diverging nozzle is important to better evaluate the overall cooling capacity and facilitate improvement in the cooling efficiency of the nozzle. The heat transfer coefficient in the two-phase region is likely to be the highest causing the largest heat transfer rate in the region. The analysis will be used to investigate and predict the maximum length of two-phase region, which will provide a greater area for heat absorption and, hence, a greater cooling potential. Again, the longer the length of two-phase region, the higher the potential for cooling. Figure 3.11 shows an overview of a pressure distribution versus the distance, z, in the converging-diverging nozzle, showing the length of two-phase region and the condensation shock occurring in the diverging section of the nozzle.

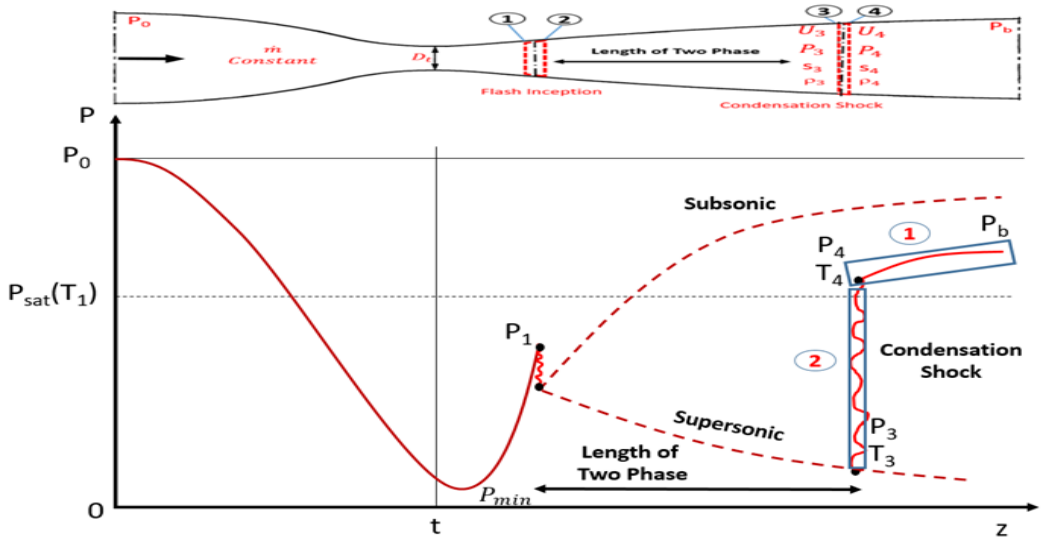

Figure 3.11 Overview of the length of two-phase region and the condensation shock.

In this section, we will introduce the assumptions and equations that were implemented to find the location of the condensation shock along the nozzle. The location of the condensation shock will provide the ability to calculate the length of the two-phase region. As seen in Figure 3.11, the condensation shock terminates from state 3 in the two-phase region to state 4 in the subcooled liquid region. The condensation shock is considered to be perpendicular to the nozzle flow. As shown in Figure 3.12, a control volume is defined enclosing the condensation shock with a cross sectional area normal to the flow direction; hence, the area is constant across the condensation shock. The upstream flow properties are denoted by the subscript 3 and the downstream properties are denoted by the subscript 4.

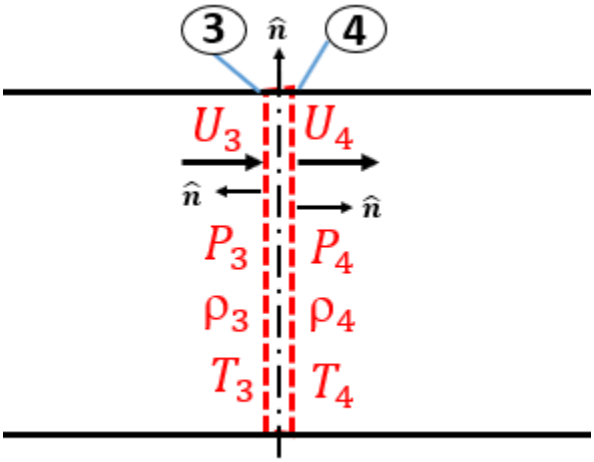

Figure 3.12 Control volume of the normal (condensation) shock across the flow in the nozzle.

The condensation shock analysis is considered to be a one-dimensional flow in the z-direction normal to the shock, where the flow properties are constant in any direction normal to the flow. The fluid is assumed to be in thermodynamic equilibrium upstream and downstream of the condensation shock. The flow is considered to be steady-state and adiabatic across the shock, which means there are no temperature gradients normal to the control volume. There is also no flow across the top and bottom boundaries of the control volume in the shock. Gravity and body forces are assumed to be negligible across the condensation shock.

The results of this analysis will introduce the dependence of the length of the two- phase region on the backpressure. As seen in Figure 3.11, two lines are highlighted in the pressure versus area plot. These correspond to the regions upstream and downstream of the

condensation shock. The analysis will be achieved by implementing a marching solution. First, a backward marching solution is used for the first line of state 4. Since the evaluation will be in the subcooled region, a mechanical energy balance will be implemented with input values of a backpressure and cross-sectional area, along with the assumption of constant density (incompressible) due to the subcooled conditions. The pressure relation at state 4 (Figure 3.12) can be expressed by

$$P_4 = P_b + \frac{1}{2}\rho\left(U_b^2 - U_4^2\right) - \Delta P_{friction} \tag{3.41}$$

where ΔP is the frictional pressure drop for the single-phase flow calculated using Equation (1.14). Equation (3.41) can be written in terms of the grid points for the marching solution using P_b, the backpressure, and U_b ,the value of velocity at the exit using the area at the exit, as the inputs,

$$P_{4_{j+1}} = P_b + \frac{1}{2}\rho\left(U_b^2 - U_{4_{j+1}}^2\right) - \Delta P_{friction,j} \tag{3.42}$$

Second, a forward marching solution is used for the second line of state 3 marked in Figure 3.11. Since the evaluation will be in the two-phase mixture region, the equations of conservation of mass, momentum, and energy obtained in Chapter 2 will be implemented to the control volume. The input values are used from the cavitation wave analysis results and, assuming a constant cross-sectional area at the shock, the conservation of mass Equation (2.8) can be rearranged in terms of states 3 and 4 which reduces to

$$\rho_3 U_3 = \rho_4 U_4 \tag{3.43}$$

Since pressure forces are the only forces acting on the control volume of the shock in the flow direction, and assuming a constant cross-sectional area at the shock, the momentum equation, Equation (2.18), can be rearranged in terms of states 3 and 4 which reduces to

$$P_3 - P_4 = \rho_4 U_4^2 - \rho_3 U_3^2 \tag{3.44}$$

While ignoring frictional head losses across the shock, and ignoring gravitational effects, the energy equation, Equation (2.26), can be rearranged in terms of states 3 and 4 and reduced to

$$h_3 + \frac{U_3^2}{2} = h_4 + \frac{U_4^2}{2} \tag{3.45}$$

Equation (3.44) can be written in terms of the grid points subscripts j and $j+1$ for the marching solution, where ρ_3 is the two-phase density and ρ_4 is the liquid density in the subcooled region as

$$P_{4_{j+1}} = P_{3_j} + \rho_{3_j} U_{3_j}^2 - \rho_4 U_{4_{j+1}}^2 \tag{3.46}$$

After obtaining the results of the two different lines of pressure distribution as a function of area using the forward and backward marching solution from Equation (3.42) and (3.46), they are plotted on the same graph. The intersection of those two lines is then found which will provide the pressure and cross-sectional area of the condensation shock location. The procedure is shown in details in Appendix (B). Then, the length of two-phase region can be found by calculating the distance between the flash inception and the condensation shock in the diverging section of the nozzle. The analysis will be applied for a given temperature by varying the backpressure in the calculations. One can therefore determine the changes in the length of two-phase region as these conditions are varied. This would be a first step toward determining the optimum conditions for achieving the maximum length of two-phase region.

Chapter 4 - Results and Discussions

This chapter presents the results from a set of comprehensive theoretical models developed in Chapter-3 for predictions of the pressure distribution as a function of cross-sectional area within the entire converging-diverging nozzle and the application of the numerical calculation techniques to describe the two-phase flow and cavitation phenomena. The nozzle inlet flow conditions such as inlet pressure, inlet temperature, mass flow rate, and backpressure from previous experimental results for water flowing through two converging-diverging nozzles (one made of glass and the second made from a transparent resin [37] are used for the analysis. The results for different inlet water temperatures are compared and discussed.

The predicted results, assumptions, nozzle inlet conditions and the numerical marching procedure used for the entire nozzle are presented in three sections. The first section introduces the point of the flash in the nozzle, i.e., the cavitation flash inception conditions, and its location. The second section presents the results of the cavitation wave analysis after occurrence of the flash. Finally, evaluation of the location of the condensation shock and determination of the length of two-phase region are presented in the third section. In addition, available pressure measurements are included which provide great insight into the flow behavior in the nozzle and how this behavior is influenced by the nozzle geometry and the inlet flow conditions. In particular, the effect of the backpressure on the length of two-phase region is presented and discussed for different inlet water temperatures.

4.1 Flash Inception Analysis Results

In order to develop some confidence in the proposed flash inception analysis, the flash prediction results developed by Abuaf [27] for Brown's data [28] were reproduced using the dynamic flash inception line analysis. The comparisons between Abuaf's results, given in Figure 1.8, and the calculated new results, are used for verification. Then, the modified dynamic flash inception line analysis is used to evaluate the onset of cavitation observed in Brown's [28], Ahmed's [23], and Gallman's [24] experimental data.

The dynamic flash inception line is evaluated using a numerical solving block for the water flow conditions in the nozzles. Results are plotted in terms of pressure undershoot as a function of local properties and depressurization rate. The reader is reminded that the pressure undershoot is the difference between the saturation pressure and the local pressure (see Chapter 1). The pressure undershoot represents the pressure threshold below the saturation pressure where flash is initiated. A third order polynomial was developed to recreate the converging-diverging nozzle geometry used by Brown [28] to be used in the flash prediction analysis. Two different tests conducted by Brown [28] were evaluated, corresponding to inlet temperatures of $270℃$ and $286℃$. The pressure data for the upstream taps and the throat given by Figure 1.7 were used to calculate the depressurization rate and the pressure undershoot. Appendix (C) shows an example calculation of all the experimental data superheats evaluated in the analysis. Equations (3.6) and (3.7) were used to calculate the depressurization rate for the upstream pressure taps and the tap at the throat, respectively. The throat tap provided a major challenge for the estimation of the depressurization because at the throat, $\frac{dA}{dz}$ equals to zero. The nozzle geometry cannot be used to calculate $\frac{dA}{dz}$, due to the "Vena contracta" effect For this case, the forward difference formula shown in Equation (3.10) was used as a numerical differentiation method between the throat and the downstream pressure taps to calculate $\frac{dA}{dz}$, and evaluate an equivalent $\frac{dP}{dz}$, as shown in Appendix (C). This approach appeared to provide the most representative evaluation considering the limited data upstream of the throat available for estimating the derivative. Figure 4.1 (a) and (b) show the results of the flash inception prediction for inlet temperatures of $270℃$ and $286℃$, respectivly. Brown's [28] experimental

superheat results are presented as the dashed line, and the solid curve represents the static flash inception line. In Figure 4.1, it is observed that as the flow approaches the smaller cross-sectional area of the throat, tap 6, the pressure undershoot increases. As the fluid approaches the throat, the cross-sectional area decreases causing the depressurization rate for the experimental superheats to increase at a region that supports high superheats. At the throat, the fluid cannot maintain any superheat within that region and relaxes with flash inception.

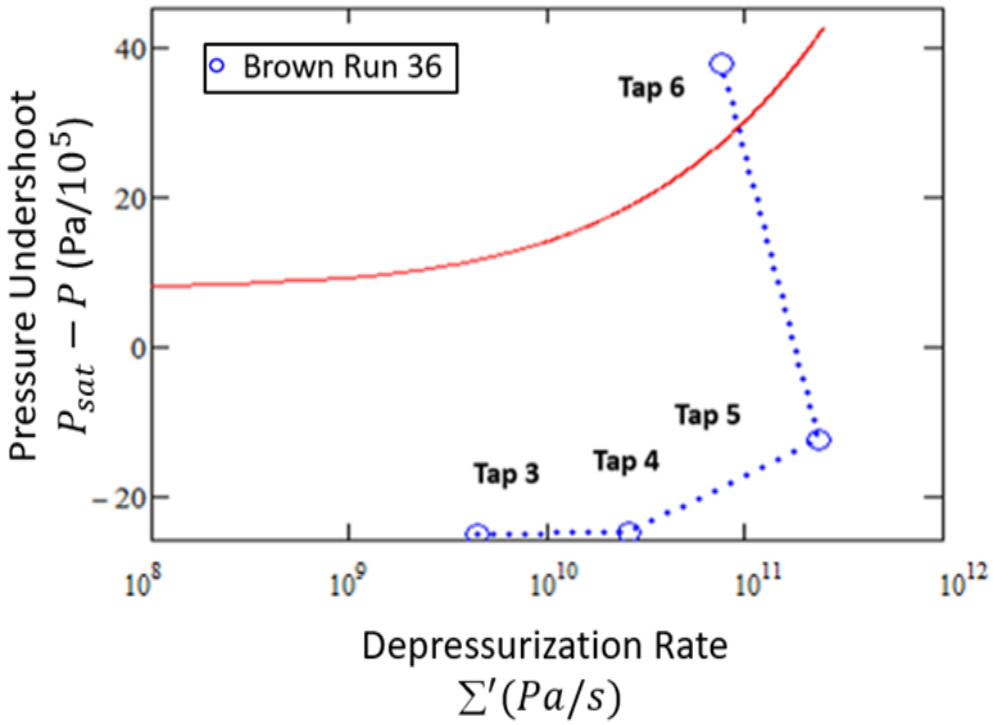

(a) T = 270℃

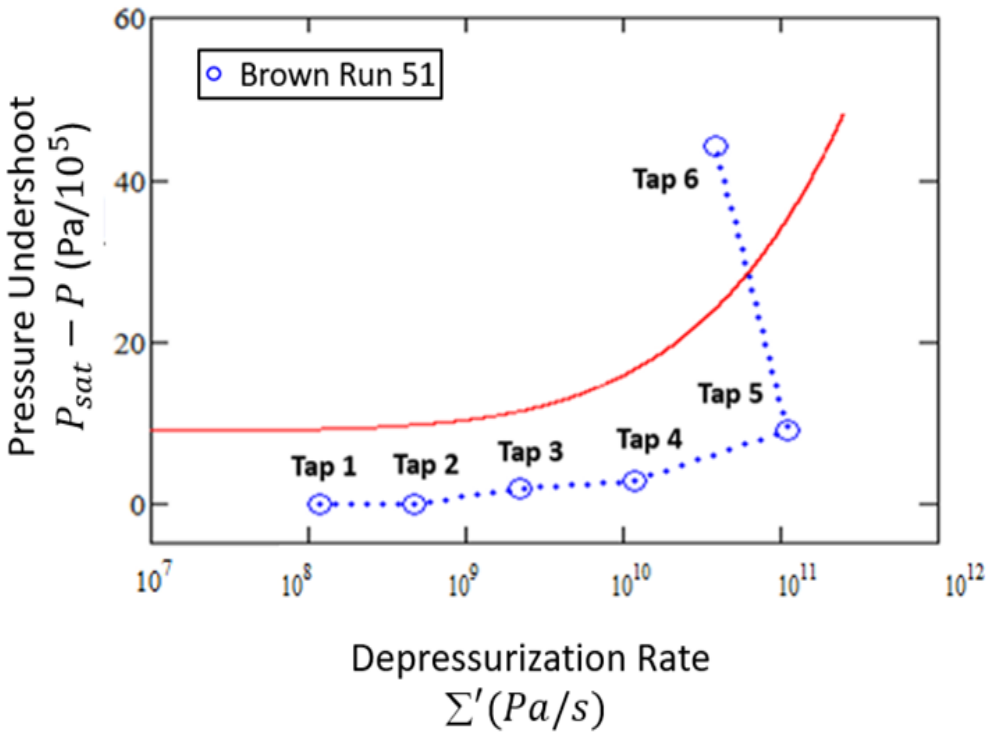

(b) T = 286℃

Figure 4.1 Reproduction of the flash inception results [27] for tests with inlet temperatures of 270℃ and 286℃, respectively [28]

The successful reproduction of Brown's results shown in Figure 4.1 verifies the reasonable accuracy of the marching procedure used for the dynamic flash inception analysis. After validating the analysis with the experimental data [28], the modified dynamic flash inception line was introduced. This analysis will account for the convective and turbulent pressure fluctuation effects, i.e., the area ratio effects and the turbulence intensity, and given by Equation (3.12). The turbulent effect considers the fluid particle experiencing a dynamic (i.e., turbulent) pressure fluctuations through the converging section of the nozzle up to the throat. By evaluating Equation (3.12), it is observed that including the turbulent pressure fluctuations will lower the flash inception line depending on the flow conditions.

Equation (4.1) the marching algorithm solution block in a functional form that was used to calculate the modified dynamic flash inception line, (ΔP_{Fi}), for the given range of depressurization rates. Starting the numerical solution with a given value of the inlet distance, and a selected grid increment of 0.5 mm to calculate the next value in the marching procedure, the cross-sectional area is then calculated and used in the evaluation of the depressurization rate to find the superheat data of the modified dynamic flash inception line. The term $\frac{dA}{dz}$ is calculated using a function in Mathcad evaluating a discrete approximation of a 3rd order polynomial representation of the geometry of the nozzle. The value of the turbulence intensity in the direction of the fluid particle movement is known to be very low in the converging section of nozzles due to the decreasing cross-sectional area to a minimum value, as observed by Jones [26].

For comparison purposes, a turbulent fluctuation intensity denoted by (ε), ranging between 0.07 and 0.12, is used in the evaluation.

$$f(z_j, \dot{m}) \left| \begin{array}{l} for\ j \in 1..n-1 \\ z_{j+1} \leftarrow z_j + 0.5 \\ A_{j+1} \leftarrow A_j(z_{j+1}) \\ \Sigma_{j+1} \leftarrow \frac{\dot{m}^3}{\rho_f^2 {A_{j+1}}^4} \left.\frac{dA}{dz}\right|_{z_{j+1}} \\ \Delta P_{Fi} \leftarrow 0.253 \frac{\sigma^{\frac{3}{2}}}{\sqrt{kT_c}} \frac{T_R^{13.73} \sqrt{1+14\,\Sigma_{j+1}^{0.8}}}{\left[1-\frac{v_f}{v_g}\right]} - 27(\varepsilon^2) \frac{\left(\frac{\dot{m}}{A_{j+1}}\right)^2}{2\rho_f} \left(\frac{A_z}{A_{in}}\right)^{1.4} \end{array} \right. \tag{4.1}$$

Following the successful reproduction of Brown's data and use of the dynamic flash inception model in Figure 4.1, the modified dynamic flash inception marching algorithm was applied to Brown's experimental data [28]. Figure 4.2 (a) and (b) show the results of the flash

inception prediction using the modified dynamic flash inception line for inlet temperatures of 270℃ and 286℃, respectively.

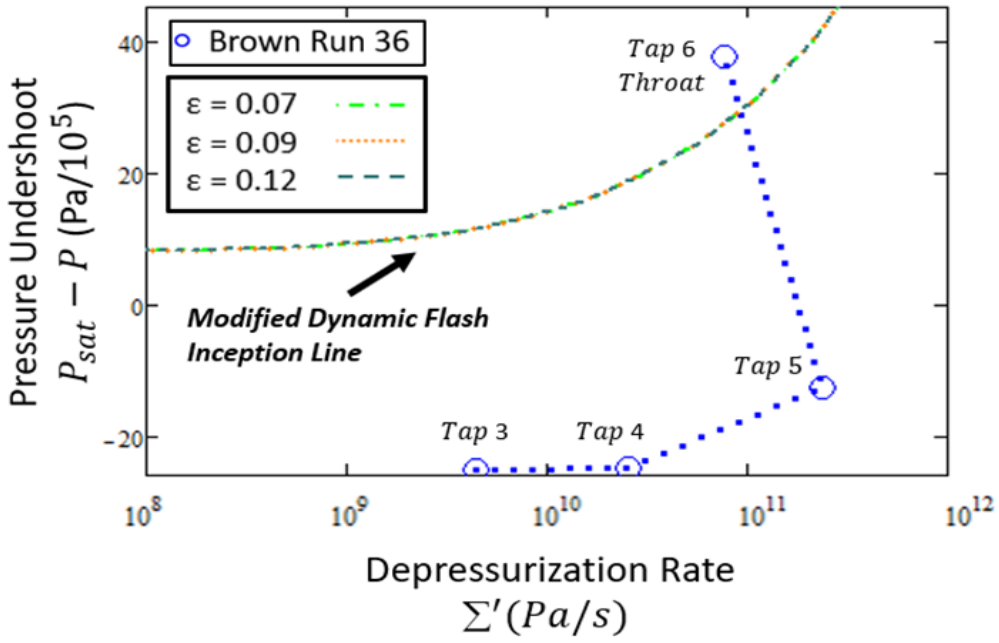

(a) T = 270℃

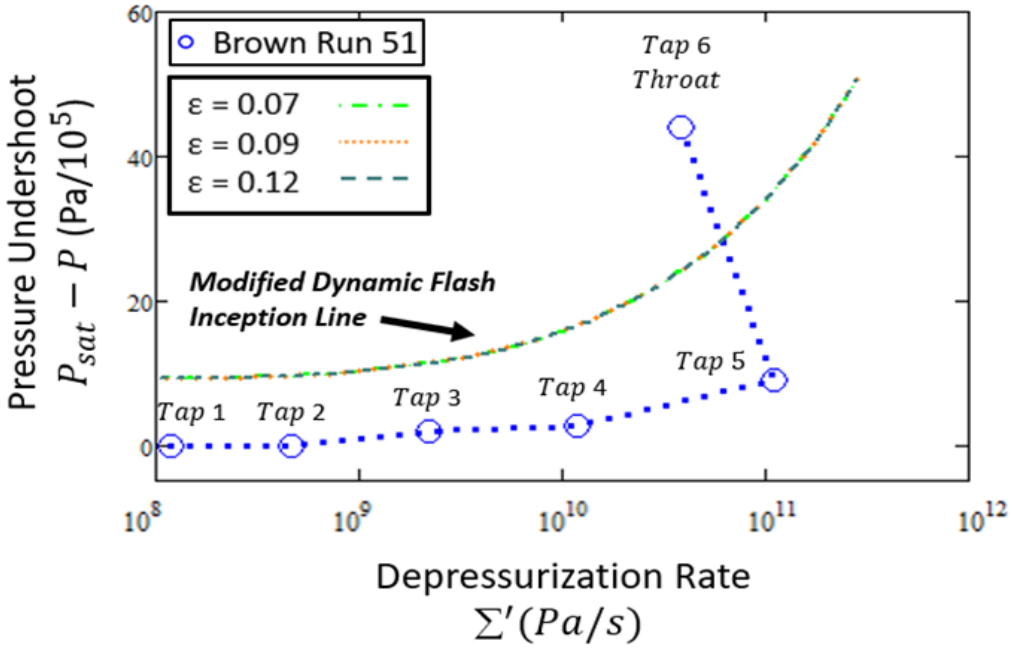

(b) T = 286℃

Figure 4.2 Flash onset prediction using the modified dynamic flash inception line for inlet temperatures of 270℃ and 286℃, respectively [28]

Results are shown in terms of pressure undershoot as a function of depressurization rate. The blue dashed line indicates the experimental data superheats. The modified dynamic flash inception line is shown for three different turbulence intensities of 0.07, 0.09, and 0.12. It is observed that the different turbulence intensities using the modified dynamic flash inception analysis are showing approximately the same results, which indicates that turbulence intensity is not playing a significant role in the prediction of the modified dynamic inception line. All flash inception lines cross the experimental data superheats between tap 5 and tap 6, the throat. The intersection of the flash inception line with the experimental superheat predicts that the flash would occur approximately at the throat where it has the minimum geometrical cross-sectional area. These results justify using the modified dynamic flash inception analysis for flowing systems in nozzles. Next, the modified dynamic flash inception analysis is used to predict the onset of flash for Ahmed's [23] test conditions applying the nozzle configuration given in Figure 3.3.

Previous experimental results by Ahmed [23] in a converging-diverging nozzle using a blow down system with different water conditions and different inlet temperatures of 70 ℃, 50 ℃, and 25 ℃ were provided in Table 1-1. Using the three different conditions, inlet temperature, inlet pressure, and mass flow rate, the predicted single-phase pressure distributions in the converging section were plotted as a function of distance as shown by Figure 3.5, Figure 3.6, and Figure 3.7. Those pressure curves were used to calculate the superheats and the depressurization rates to predict the onset of flash in the converging-diverging nozzle. Three different locations of calculated pressure, given at distances of -8 mm and -4 mm upstream of the throat, and at 0 mm, which is at the throat, were used to calculate the superheats. The details of these calculations are presented in Appendix (C). The locations can be seen in the nozzle geometry given in Figure 3.3. The pressures at the three locations respectively are (96 kPa, 56 kPa, 4.47 kPa) for 70 ℃, (95 kPa, 46 kPa, -14 kPa) for 50 ℃, and (94.7 kPa, 43 kPa, -23 kPa) for 25 ℃. The modified dynamic flash inception analysis is first applied to the case with an inlet temperature of 70 ℃ to predict the point of flash in the nozzle. Figure 4.3 shows the results of the prediction for the pressure undershoot as a function of depressurization rate for 70 ℃. From the figure, it is seen that the flash inception is predicted to occur where the superheats data between location 3 and location 4 crosses the modified dynamic flash inception

line. Location 3 is 4 mm upstream of the throat and location 4 is at the minimum geometrical cross-sectional area in the nozzle, the throat. As mentioned in the literature review from Ahmed's experimental flow visualization tests [23], the point of flash was observed to be stable at the throat. Another visualization [23] observed a region of two-phase flow located at a small distance downstream of the throat with the lowest pressure, which has been explained by the "Vena contracta" effect. The modified dynamic flash inception analysis is applicable in the converging section of the nozzle up to the throat, but does not allow for determining the pressure undershoot downstream of the throat because of the increasing cross-sectional area in the diverging section of the nozzle affecting the estimation of $\frac{dA}{dz}$. Therefore, it will be assumed that the flash occurs approximately at the throat or near downstream of the throat.

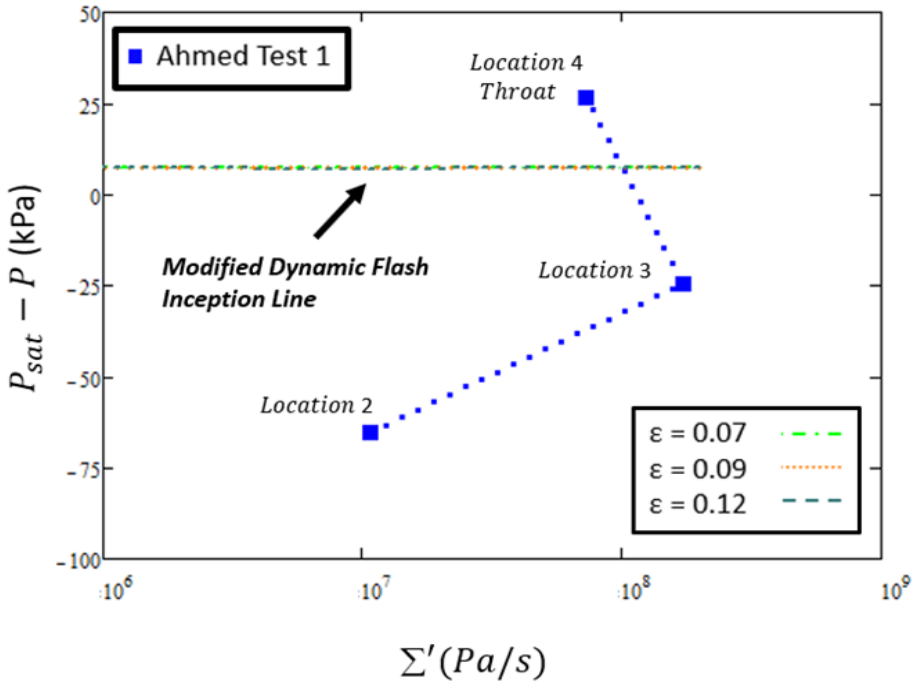

Figure 4.3 Flash onset prediction using the modified dynamic flash inception line for 70 ℃ [23]

The same behavior and conclusions are observed from the results of the other two experimental data sets for inlet temperatures of 50 ℃ and 25 ℃ shown in Figure 4.4 and Figure 4.5, respectively. The results show the modified dynamic flash inception line predicted the flash inception location for the tests with different inlet temperatures of 70 ℃, 50 ℃, and 25 ℃

very well. Next, the modified dynamic flash inception analysis is used to predict the flash inception for Gallman's [24] water test conditions applying the nozzle configuration given by Figure 3.3.

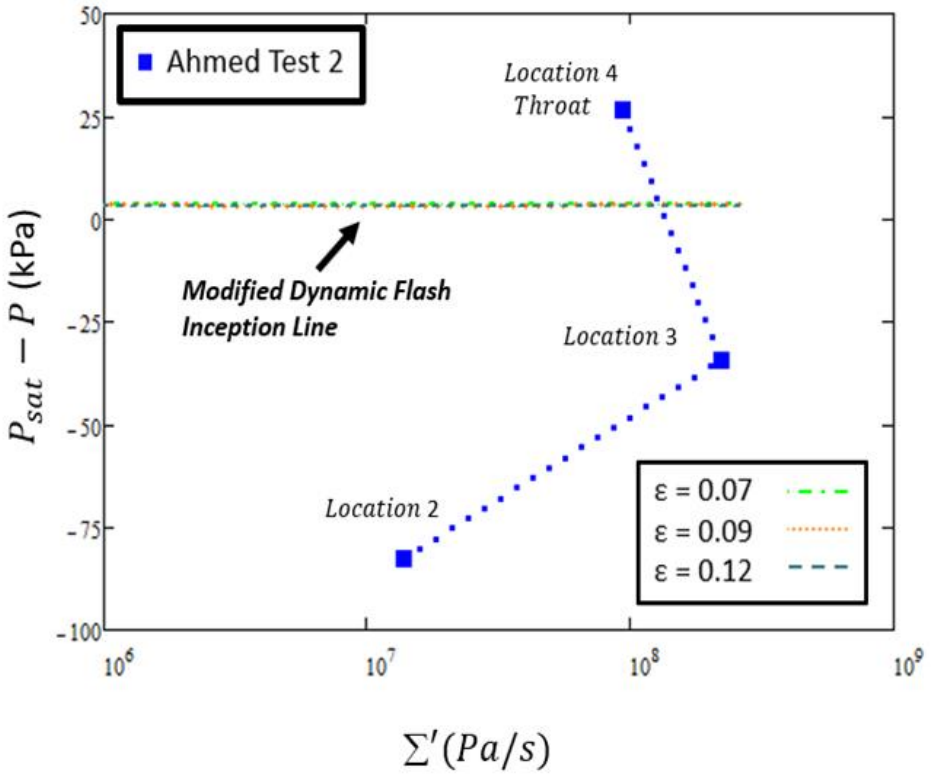

Figure 4.4 Flash onset prediction using the modified dynamic flash inception line for 50 ℃ [23]

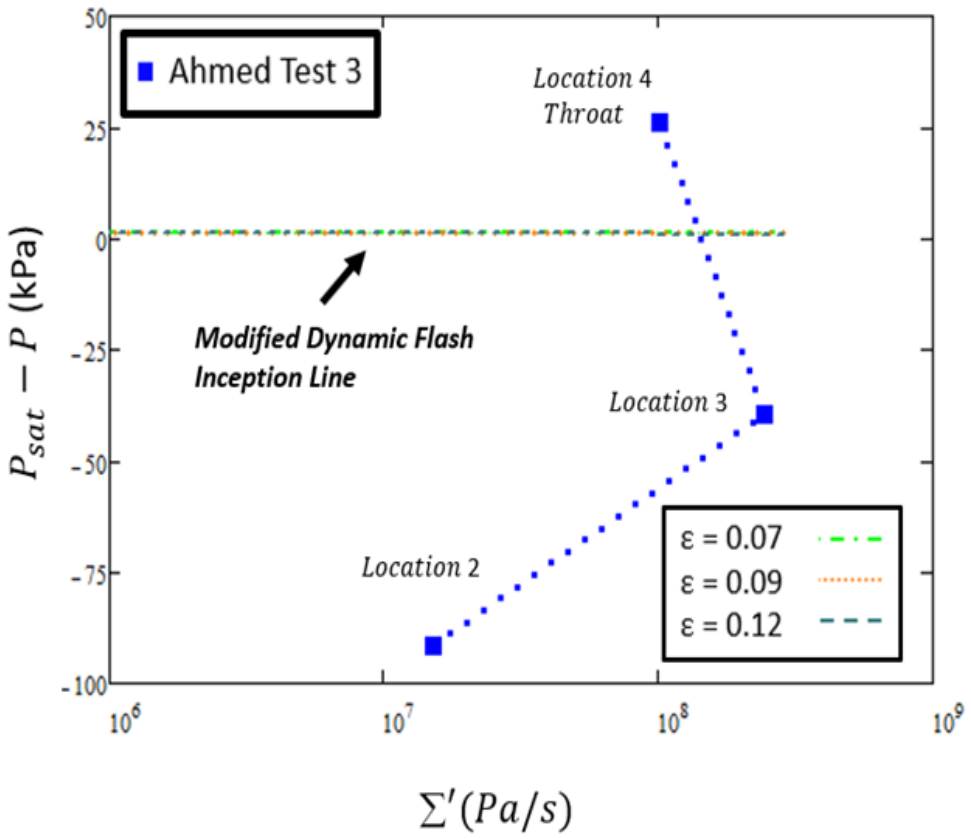

Figure 4.5 Flash onset prediction using the modified dynamic flash inception line for 25 ℃ [23]

Gallman [24] obtained direct pressure measurement data using pressure taps from a transparent converging-diverging nozzle capable of allowing visualization. Three different tests conducted using a plastic 3D converging-diverging nozzle having the same geometry as the nozzle configuration shown in Figure 3.3. He varied the steady state flow test conditions by controlling the nozzle backpressure, and recorded the onset of cavitation using a high-speed video camera. The experimental test conditions are applied in the modified dynamic flash inception analysis to predict the point of the flash in the nozzle. The water conditions for the three tests associated with different backpressures, and the measured mass flow rate are shown in Table 4-1.

Table 4-1 Water conditions for the flash inception prediction analysis for water, Gallman [24]

Test	Back Pressure	Inlet Pressure	Mass Flowrate	Fluid Temperature	Saturation Pressure
Number	(kPa)	(kPa)	(kg/s)	(°C)	(kPa)
1	43.2	99.4	0.02448	20	2.33
2	30.5	102.7	0.02448	20	2.33
3	15.17	103.4	0.02448	20	2.33

The measured experimental pressure data for the water experiments [24] were employed in the modified dynamic flash inception analysis in a similar manner to investigate the location of the flash initiation. The first test had a backpressure of 43.2 kPa. Figure 4.6 shows the measured experimental pressure distribution as a function of distance along the length of the nozzle for the first test condition with an inlet pressure of 99.4 kPa, a backpressure of 43.2 kPa, and an inlet temperature of 20°C. The solid black vertical line in Figure 4.6 indicates the location of the throat in the nozzle, and the corresponding pressure tap location. As seen from the figure, the minimum pressure occurred slightly downstream of the throat due to the "Vena contracta" effect in the diverging section of the nozzle. This is accompanied by significant frictional losses in the downstream region where cavitation and two-phase flow exists.

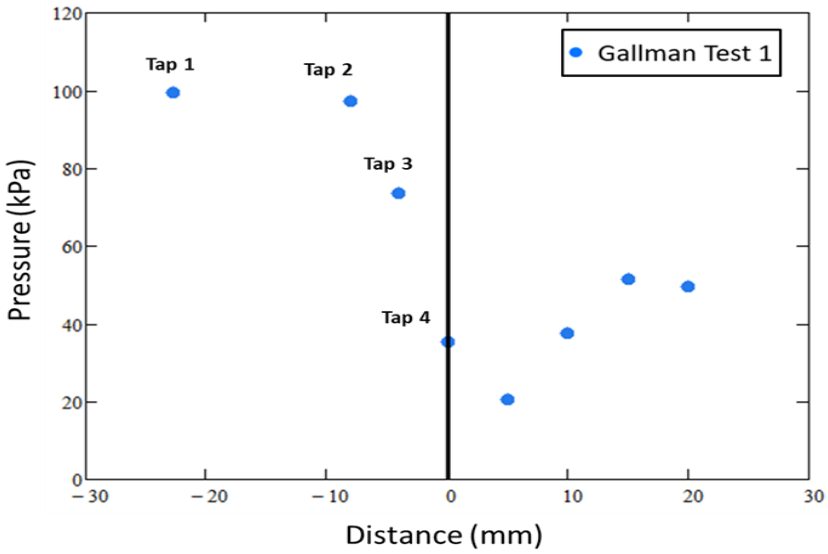

Figure 4.6 Pressure distribution as a function of distance in nozzle for a backpressure of 43.2 kPa [24]

The nozzle geometry, the water temperature, constant mass flow rate, and the pressure distribution data up to the throat shown in Figure 4.6 were used as inputs in the analysis for the evaluation of the flash inception point. Using the test conditions given in Table 4-1 and following a procedure similar to that shown in Figure 4.3, the results of the first test are plotted in Figure 4.7 in an attempt to predict the flash inception point. Figure 4.7 shows the pressure undershoot as a function of depressurization rate for an inlet temperature of 20℃. The blue dashed line indicates the experimental data superheats. The values of pressure undershoot in the figure were calculated from the measured pressure at each tap, starting from the inlet tap up to the throat tap in the converging section of the nozzle. The pressure undershoot was determined by subtracting the local pressure from the saturation pressure for the given temperature. The depressurization rate was calculated using Equations (3.6) and (3.7), as shown in Appendix (C).

The results from Figure 4.7 show the modified dynamic flash inception line for three different turbulence intensities 0.07, 0.09, and 0.12. Again, it is observed that the impact of the turbulence intensity on the modified dynamic flash inception lines is insignificant and all three turbulence intensity results are close to each other. However, the results show that the experimental data superheats never intersect with the modified dynamic flash inception lines. This is due to the lower range of the depressurization rate and the lower value of the water temperature for the current experimental data points. In the literature review, the range of depressurization rate that was given for Brown's data [28] falls between 10^8 Pa/s and 10^{11} Pa/s, whereas Gallman's [24] experimental data points have depressurization rates in the range of 10^6 Pa/s to 10^8 Pa/s. This range is much lower than what is given by Brown's data as is the temperature range associated with the two experimental nozzles.

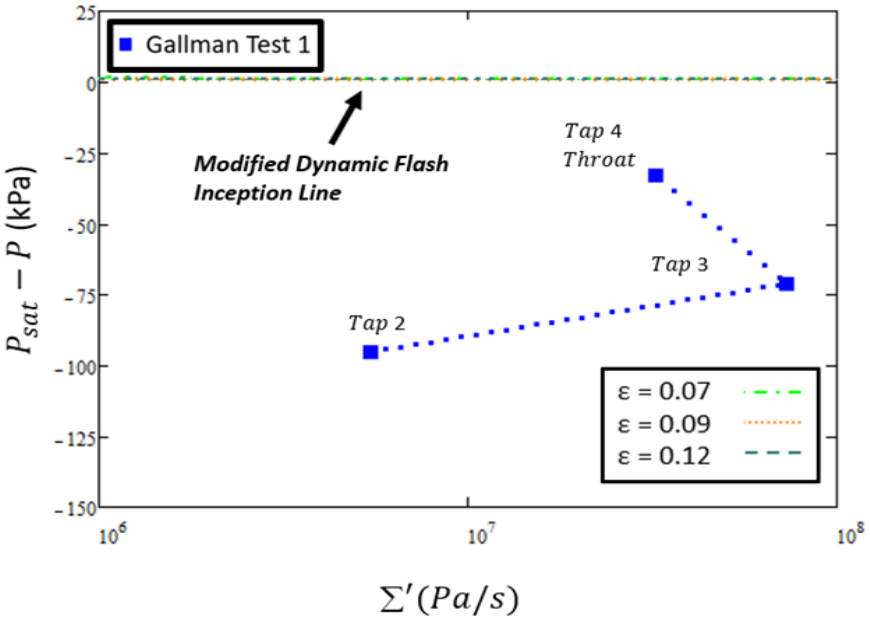

Figure 4.7 Flash onset prediction for a backpressure of 43.2 kPa [24] using the modified dynamic flash inception line

After applying the modified dynamic flash inception analysis to predict the onset of the flash for the first test, the same analysis is implemented to the second and third experimental tests. The second experimental test had water conditions with an inlet pressure of 102.7 kPa and a backpressure of 30.5 kPa and the third experimental test with an inlet pressure of 103.4 kPa and a backpressure of 15.17 kPa; both having the same inlet temperature of 20℃ as shown in Table 4-1. Figure 4.8 shows the pressure distribution data as a function of distance for both water tests [24]. Figure 4.8 (a) shows the pressure distribution data for a backpressure of 30.5 kPa and Figure 4.8 (b) shows the pressure distribution data for backpressure of 15.17 kPa.

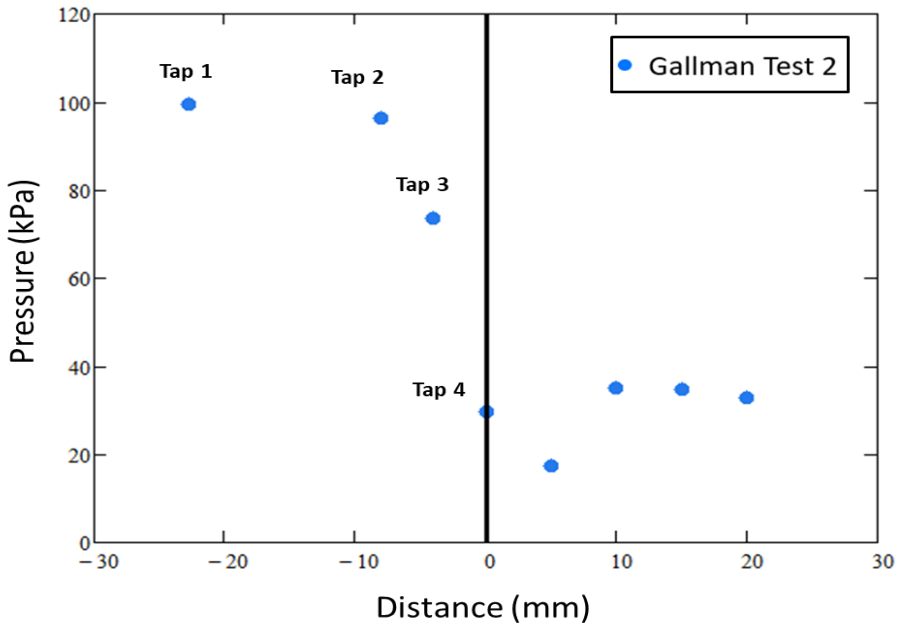

(a) Backpressure = 30.5 kPa

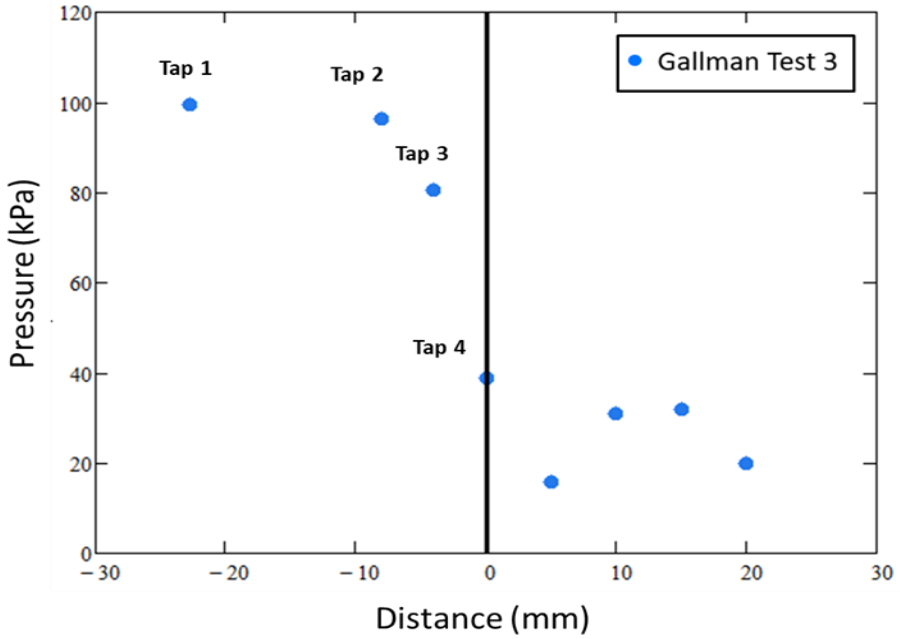

(b) Backpressure = 15.17 kPa

Figure 4.8 Pressure distribution as a function of distance in nozzle; (a) Backpressure of 30.5 kPa, (b) Backpressure of 15.17 kPa [24]

Using the measured pressure distribution, the experimental superheat data is calculated and plotted in terms of the pressure undershoot as a function of depressurization rate for each test, as given in Appendix (C). Figure 4.9 show the results of the second and third water run, where the modified dynamic flash inception line analysis is applied. Figure 4.9 (a) shows the flash onset prediction for a backpressure of 30.5 kPa and Figure 4.9 (b) shows the flash onset prediction for a backpressure of 15.17 kPa. The figures show the pressure undershoot as a function of depressurization rate for experimental superheats data and the modified dynamic flash inception line using the different ranges of turbulence intensity fluctuations. The results again show that the experimental data superheats line never intersects with the modified dynamic flash inception line.

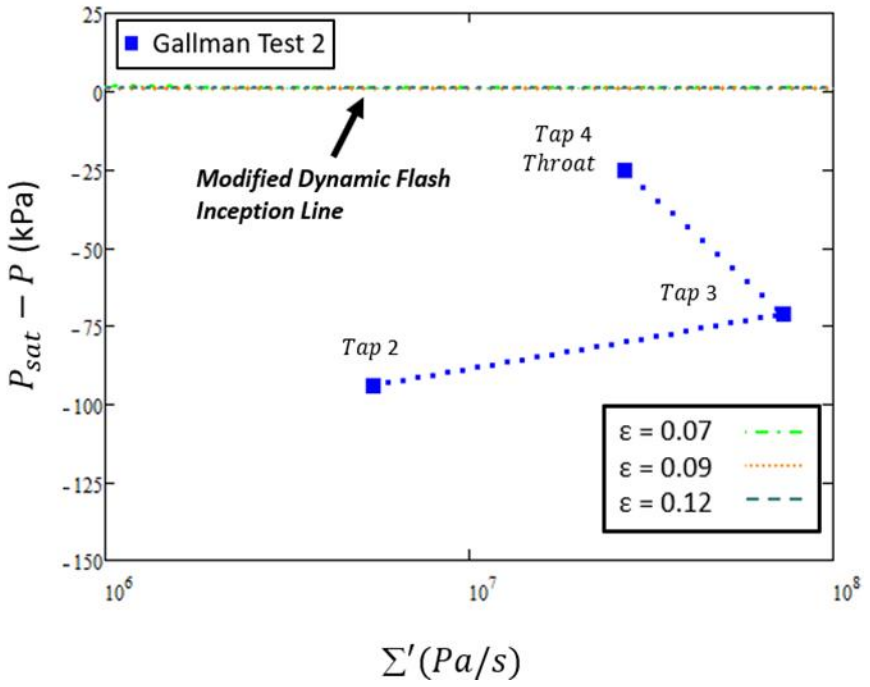

(a) Backpressure = 30.5 kPa

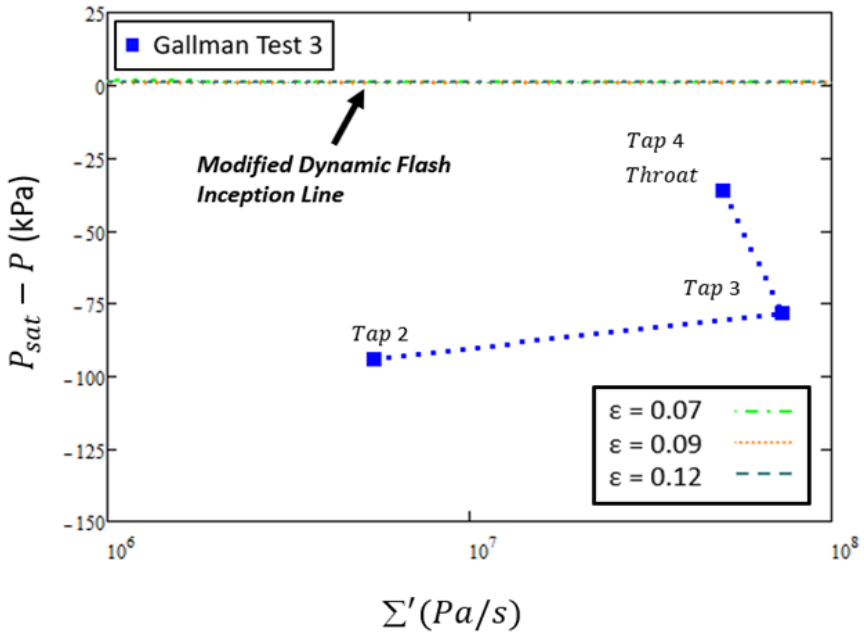

(b) Backpressure = 15.17 kPa

Figure 4.9 Flash onset prediction using the modified dynamic inception line; (a) Backpressure of 30.5 kPa, (b) Backpressure of 15.17 kPa [24]

After further investigation into the reasons behind the modified dynamic flash inception not predicting the flash onset for Gallman's 20 ℃ experimental data [24], yet working successfully for Ahmed's 25 ℃ experimental data [23], it was determined that the difference in the mass flow rates was the key factor. The mass flow rate for Ahmed's experiment was $0.0349\frac{kg}{s}$ for the inlet water temperature of 25 ℃; however, the mass flow rate for Gallman's experiment was lower at $0.0248\frac{kg}{s}$ for the inlet water temperature of 20 ℃ t. A lower mass flow rate causes the depressurization rate to be smaller and the pressure in the nozzle does not go below the saturation pressure; therefore, a flash is not predicted to occur. Ahmed [23] further observed that flash initiated around a mass flow rate of $0.0349\frac{kg}{s}$ and at a lower mass flow rate wouldn't result in a flash inception. However, Gallman [24] observed that flash seem to be initiated at a lower mass flow rate of $0.0248\frac{kg}{s}$ even though flash was not supposed to occur at a lower mass flow rate. This discrepancy can be explained by hypothesizing that the pressure taps drilled in the 3D plastic nozzle at the throat may have resulted in a localized burr causing a premature flash inception to occur on one side of the nozzle starting at the throat (see

Appendix D). In addition, the plastic nozzle material used may have exhibited characteristics of a rough surface, which can cause a premature flash inception, as compared to the smooth glass nozzle used by Ahmed.

To validate the argument, a higher mass flow rate was used for Gallman's test conditions to calculate a new pressure distribution and predict new results for the flash inception. First, water conditions of a mass flow rate of $0.0349\frac{kg}{s}$, an inlet temperature of 20 ℃, and an inlet pressure of 99.4 kPa used to predict the single-phase pressure drop in the converging section of the nozzle. Figure 4.10 shows the comparison of the calculated pressure distribution (red line) and the measured data (black circles) by Gallman [24] for a mass flow rate of $0.0248\frac{kg}{s}$ and the calculated pressure distribution (blue line) for the new proposed mass flow rate of $0.0349\frac{kg}{s}$ for a temperature of 20℃. The solid black vertical line in Figure 4.10 indicates the location of the throat in the nozzle and the dash line corresponds to the saturation pressure for the inlet temperature. Since the calculated line with a mass flow rate of $0.0248\frac{kg}{s}$ predicted the experimental data measured by Gallman [24] in the converging section of the nozzle, it is reasonable that it be used to predict the pressure distributions for other mass flow rates. It is observed that using a mass flow rate of $0.0349\frac{kg}{s}$ theoretically lowers the pressure distribution significantly below the saturation pressure, which is likely sufficient enough to cause the flash inception to occur in the nozzle (as was the case with Ahmed's nozzle).

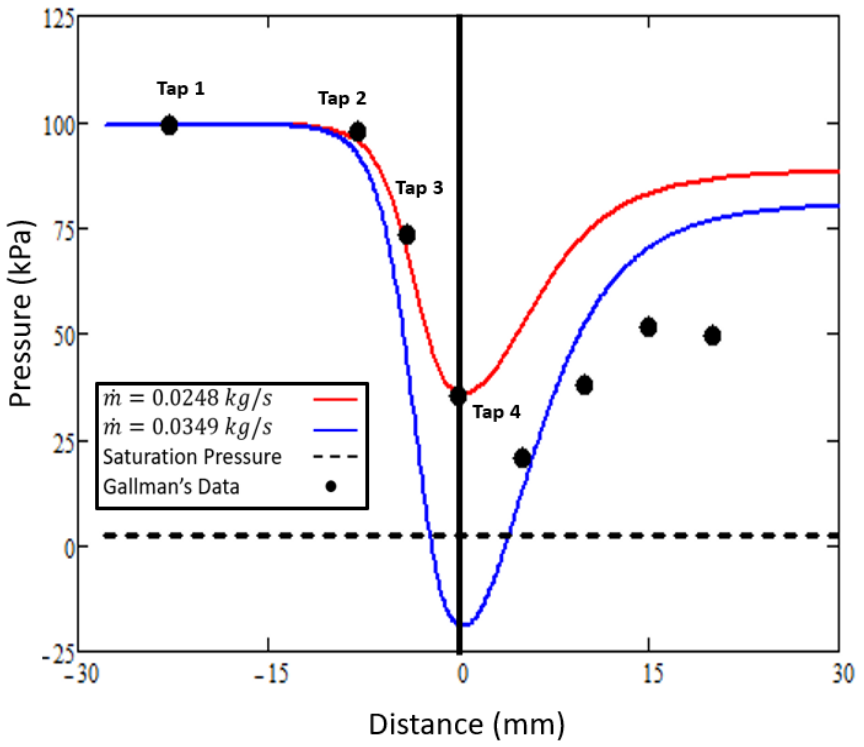

Figure 4.10 Comparisons of the calculated pressure distribution for different mass flow rates and the measured data by Gallman [24] for a temperature of 20℃

After predicting the pressure distribution for the new mass flow rate, the modified dynamic flash inception line analysis can be applied to predict the onset of flash. Figure 4.11 shows the pressure undershoot as a function of depressurization rate for the experimental superheats using the modified dynamic flash inception analysis for an inlet temperature of 20℃ and a mass flow rate of $0.0349\frac{kg}{s}$. The blue dashed line indicates the experimental data superheats. From the figure, it is seen that the flash inception is predicted to occur at the throat of the nozzle where the modified dynamic flash inception line crosses the superheats data between location 3 and location 4, at the throat. The results verify that the modified dynamic flash inception analysis should work for all nozzle flows with the exception of cases where premature flash occurs in the nozzle similar to Gallman's experimental visualization (see details in Appendix D).

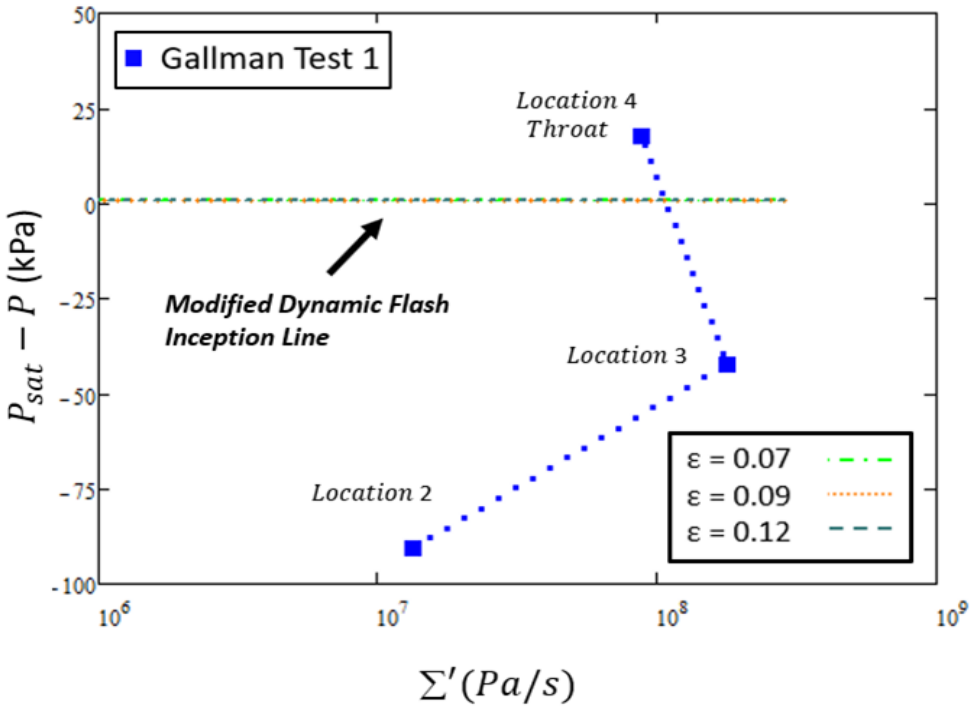

Figure 4.11 Flash onset prediction temperature of 20℃ [24] using the modified dynamic flash inception line

4.2 Flash "Cavitation Wave" Results

Once the flash inception location is found, one will be able to start the prediction of the onset of cavitation (flash inception) using cavitation wave analysis in the diverging section of the nozzle. The results of the flash inception prediction will be used as the starting conditions to run the step-by-step marching procedure given previously by Equation (3.13). Also, the key assumptions for the evaluations have been discussed in chapter 3 and will be used in this analysis. In this section, evaluation and comparisons are presented between the experimental results obtained by Ahmed [23] and the theoretical results from the current analysis.

The single-phase pressure analysis cannot be used to calculate the pressure distribution downstream of the throat and beyond the point of flash inception due to the presence of a two-phase mixture. A two-phase pressure drop model must be implemented to account for the phase change after cavitation. Also, the previous flash inception point analysis did not account for the separation effects and the associated "Vena Contracta" effects that occur at the throat and downstream of the throat. Separation was clearly shown to occur in the experimental results for water flowing through the converging-diverging nozzle [23], which are being used for comparison with the current theoretical analysis. In the referenced experimental flow visualization results, it was shown that the point of flash occurred a few millimeters downstream of the throat, defining the initiation of a two-phase mixture. For that reason, an assumption is made that the flash inception occurred 4 mm to 5 mm downstream of the throat, consistent with the "Vena Contracta" effect observed in the experimental results [23]. The pressure and area at that location are then calculated and used as the starting conditions for the flash (cavitation) wave analysis beyond the point of flash. From the previously calculated pressure distribution for water flowing through a converging-diverging nozzle in Figure 3.5, Figure 3.6, and Figure 3.7 , it is shown that the pressure in the diverging section approaches the saturation pressure 4 mm to 5 mm downstream of the throat for all three of the different temperature cases (70 ℃, 50 ℃, and 25 ℃). Values close to the saturation pressure can be assumed and used as the flash inception point for the analysis.

For the two-phase flow following the flash inception, void fraction is introduced to characterize the fluid flow in the nozzle. It will be used to calculate key physical parameters in the analysis. For the flash wave analysis, the homogenous equilibrium model (HEM) is assumed with the no-slip condition, where both liquid and gas phases are traveling with the same velocity. The HEM void fraction relationship given by Equation (1.4) is plotted for the different cases of temperatures used in the experimental analysis. Figure 4.12 (a) shows this variation of void fraction as a function of two-phase flow quality for different saturation temperatures of 370 ℃, 286 ℃, 198 ℃, 70 ℃, 50 ℃, and 25 ℃. As seen in Figure 4.12 (a), the void fraction increases rapidly at very low qualities up to a point where it approaches unity. The curves for 70 ℃, 50 ℃, and 25 ℃ are steep using the scale given in Figure 4.12 (a). At that scale, the difference in the lines of void fraction as a function of quality is almost imperceptible and collapse together for temperatures of 70 ℃, 50 ℃, and 25 ℃. Expanding the scale as shown in Figure 4.12 (b) presents better results for lower temperatures as the void fraction approaches unity. At very high temperatures and pressures, the vapor specific volume will decrease, reducing the void fraction to an almost linear relationship with the quality.

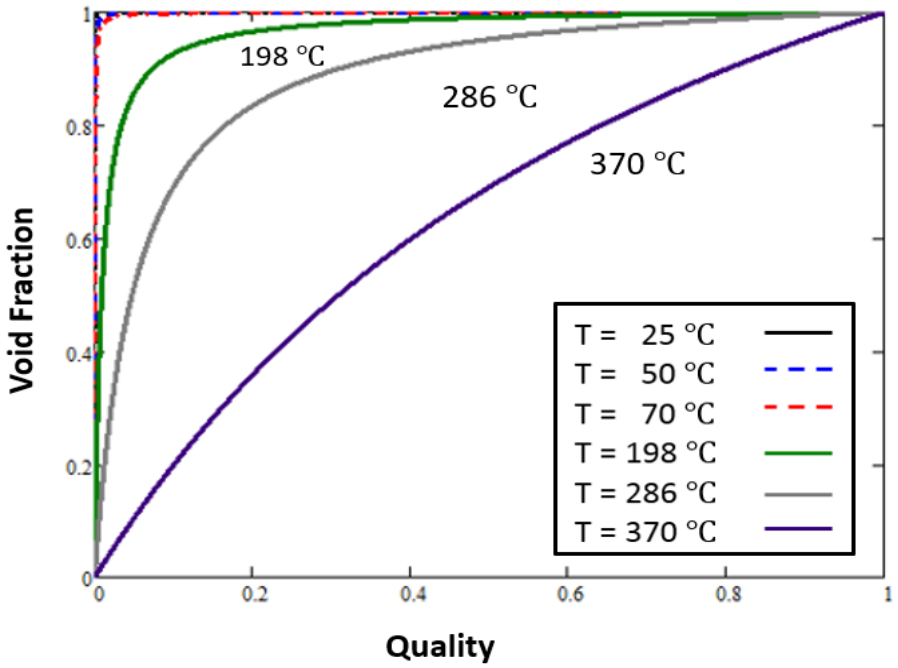

(a) Full range

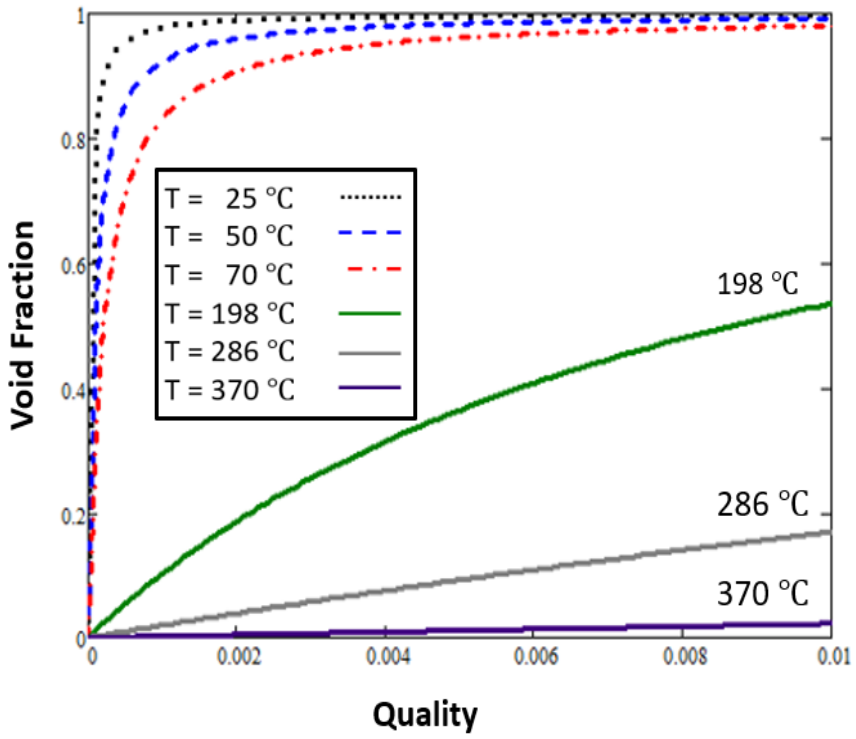

(b) Expanded range

Figure 4.12 Void fraction (HEM) as a function of quality for various fluid temperatures

Another important parameter to understand and evaluate is the value of the speed of sound downstream of the flash inception. Two different speed of sound models given by Wallis [14] Equation (1.8) and Franc [15] Equation (1.9) were discussed in the literature review for two-phase flow in the converging-diverging nozzle. Assuming the two-phase mixture is homogenous, in thermodynamic equilibrium, and neglecting surface tension effects, the calculated speed of sound from both equations is compared for all three given temperatures under investigation. Figure 4.13 shows the Wallis [14] speed of sound equation as a function of void fraction for water. Figure 4.14 shows the Franc [15] speed of sound calculation as a function of void fraction for water. Results show that using the Wallis equation gives high values of speed of sound up to 1000 m/s at very small void fraction then decreases to a minimum at a value of void fraction of 0.5, with the same pattern for all temperatures. On the other hand, the equation by Franc shows low speed of sound values between 0.01 and 1 at very low void fraction and then increasing values of sound speed, for all temperature, as the void fraction increases to a maximum value of 1. Considering the homogenous equilibrium model

assumption and the accounting for phase change in the Franc speed of sound equation, the Franc model was chosen for the flash wave analysis downstream of the flash inception.

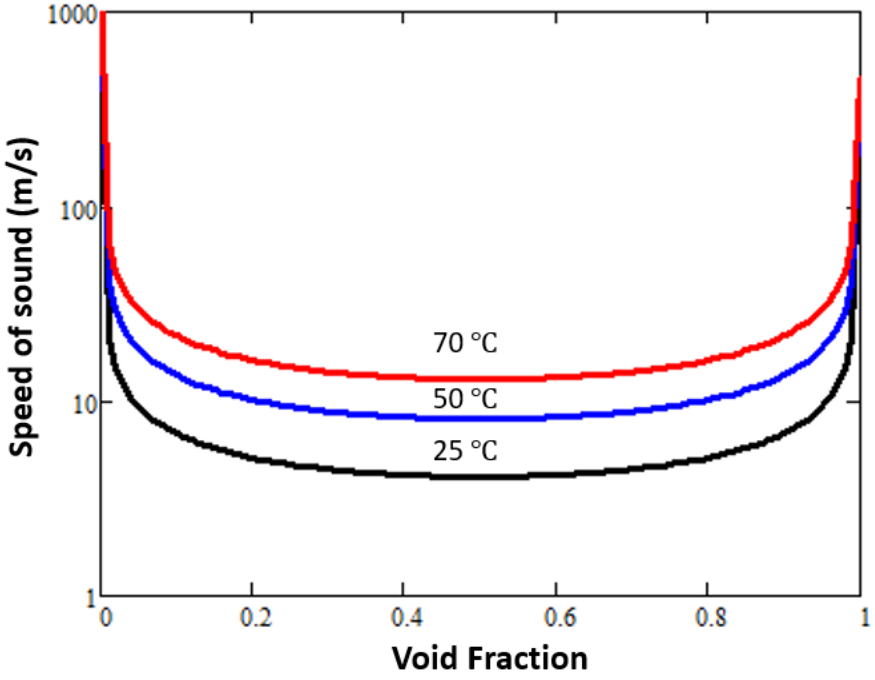

Figure 4.13 Speed of sound as a function of void fraction by Wallis [14]

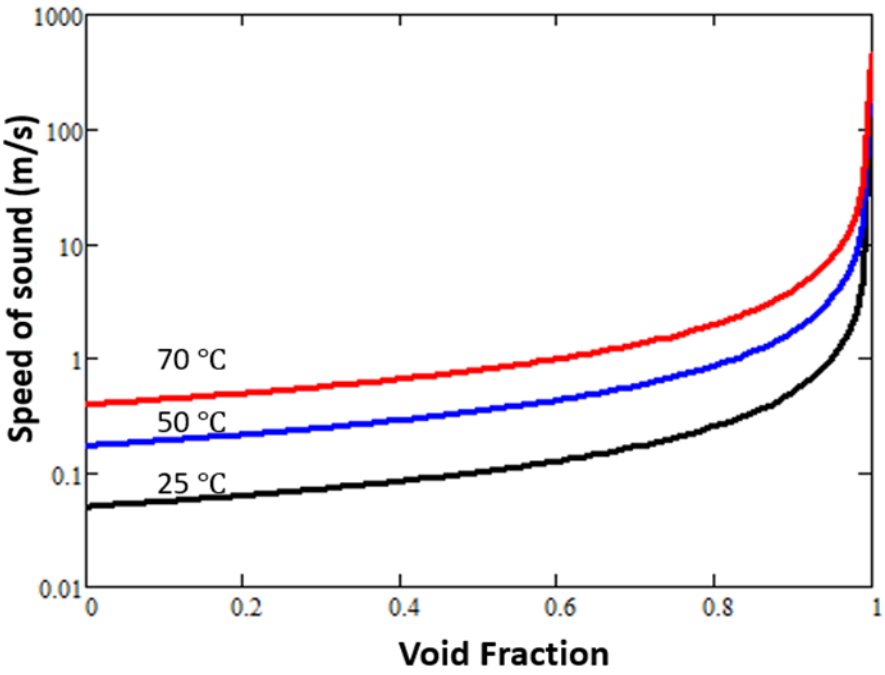

Figure 4.14 Speed of sound as a function of void fraction by Franc [15]

Limited experimental work was found to be available in the published literature for two-phase pressure drop models in variable area ducts. This led to investigating comparisons between the different models that were previously discussed in the literature review. The Friedel, the Lockhart-Martinelli, and the Jung- Radermacher two-phase frictional pressure drop models have been studied and each was implemented, for comparison purposes, into the current nozzle analysis model and compared to the experimental data [23]. The comparisons between the models for a temperature of 70 ℃ and the nozzle geometry shown in Figure 3.3. Each two-phase pressure drop model is calculated from the single-phase pressure drop due to friction multiplied by a two-phase multiplier. Each two-phase multiplier was calculated using a different empirical correlation associated with each model. The single-phase pressure drop was calculated for smooth pipe flows and then implemented in the pressure drop model. Results of the two-phase pressure drop models using friction factors for smooth pipe flows showed poor comparisons with the experimental results. Considering the analysis on converging-diverging nozzles, a single-phase pressure drop using the diffuser model is introduced and used in the two-phase model. Equation (4.2) shows the single-phase head loss coefficient for general diffusers from inlet area A_1 at location 1 in the diffuser to outlet area A_2 at location 2 in the diffuser.

$$K = \left[1 - \left(\frac{A_1}{A_2}\right)^2\right] - C_P \tag{4.2}$$

where C_P is the pressure recovery coefficient defined by

$$C_P = \frac{P_2 - P_1}{\frac{1}{2}\rho U_1^2} = \eta\left[1 - \left(\frac{A_1}{A_2}\right)^2\right] \tag{4.3}$$

where η is referred to as the pressure recovery efficiency, or the diffuser efficiency, which is defined as the actual pressure recovery divided by the ideal pressure recovery which depends only on the nozzle geometry (from Bernoulli's equation). U_1 is the velocity at the inlet of the diffuser, and P_1 and P_2 are the pressures at the inlet and outlet of the diffuser, respectively. When there is no pressure recovery, the diffuser efficiency will have a value of zero. For the

case of full pressure recovery, the diffuser efficiency will have a value of 1. Because of flow separation occurring in the nozzle along with wall friction losses, a nominal value for the diffuser efficiency is assumed to be 75%, which was fitted with the experimental data given by Table 1-1. Finally, the equivalent pipe flow friction factor for the diffuser case is given by

$$f = \frac{Kd}{L} \tag{4.4}$$

where d is the nozzle diameter and L is the pipe length. Results of the comparisons showed that the Friedel model using the diffuser friction factor compared best with the experimental work and was therefore selected as the model to be used for the two-phase nozzle analysis [23].

After comparing the different models of the speed of sound, and the friction factor and frictional pressure drop models, the models that provided the best results were implemented into the model. The chosen models are the Franc model for the speed of sound, the diffuser model for the single-phase friction factor, and the Friedel model for the two-phase pressure drop multiplier model. After determining the flash inception point, the step-by-step marching procedure is started at this point downstream of the throat of the converging-diverging nozzle. The marching procedure code shown in Equation (3.13) starts with four input parameters: the calculated pressure downstream the flash, the specific volume at the given temperature, the area at the flash inception and the mass flowrate. The input parameters can be found and calculated from Table 3-2 for the three different water temperatures that are being analyzed, i.e., 70 ℃, 50 ℃, and 25 ℃. Experimentally, it was shown that the flash inception occurred a few millimeters downstream of the throat caused by the "Vena contracta" effects. The analysis makes the same assumptions given the same converging-diverging nozzle geometry. The supersonic region is then calculated from the program following the procedure presented in Chapter 3.

Figure 4.15 shows the pressure distribution as a function of distance in the nozzle for a temperature of 70 ℃. The converging-diverging nozzle geometry is also included in the figure for explanation purposes. Results show the estimated values of pressure as a function of

distance through the nozzle up to a point before the shock wave analysis is implemented. Then, after the flash occurs downstream of the throat, as seen in Figure 4.15, the pressure starts slowly decreasing in the supersonic region. It is shown that the pressure drop is very small for water cavitation through the converging-diverging nozzle, similar to previous experimental work by Abuaf [27]. Once the flash inception occurs, the two-phase flow quality of water in the supersonic region was shown to be very small and ranged between $5x10^{-6}$ and $2x10^{-4}$. From Figure 4.12 and Figure 4.13, it is observed that the smaller the flow quality, the smaller the void fraction becomes, which results in slowing the flow acceleration in the supersonic region. This causes the pressure to drop more gradually through the remainder of the diverging section of the nozzle. The qualities in the supersonic region were too small to cause a noticeable pressure and temperature drop. Similar results follow from analyzing the two other test conditions for 50 ℃, and 25 ℃. Figure 4.16 shows the pressure distribution as a function of distance in the nozzle for a temperature of 50 ℃.

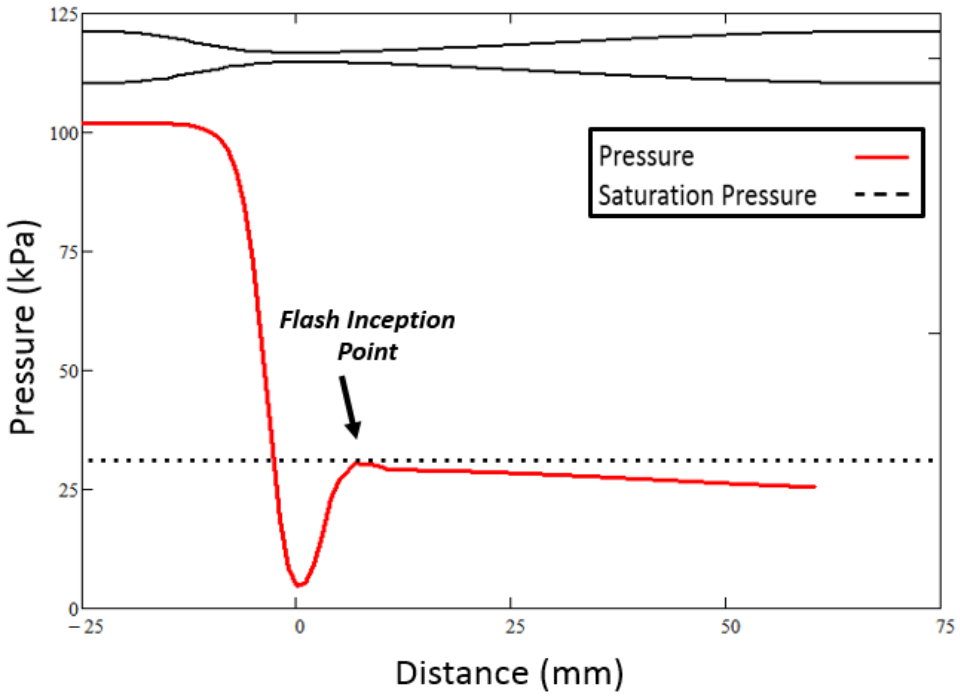

Figure 4.15 Pressure distribution as a function of distance in the converging diverging nozzle for a temperature of 70 ℃ under cavitating conditions.

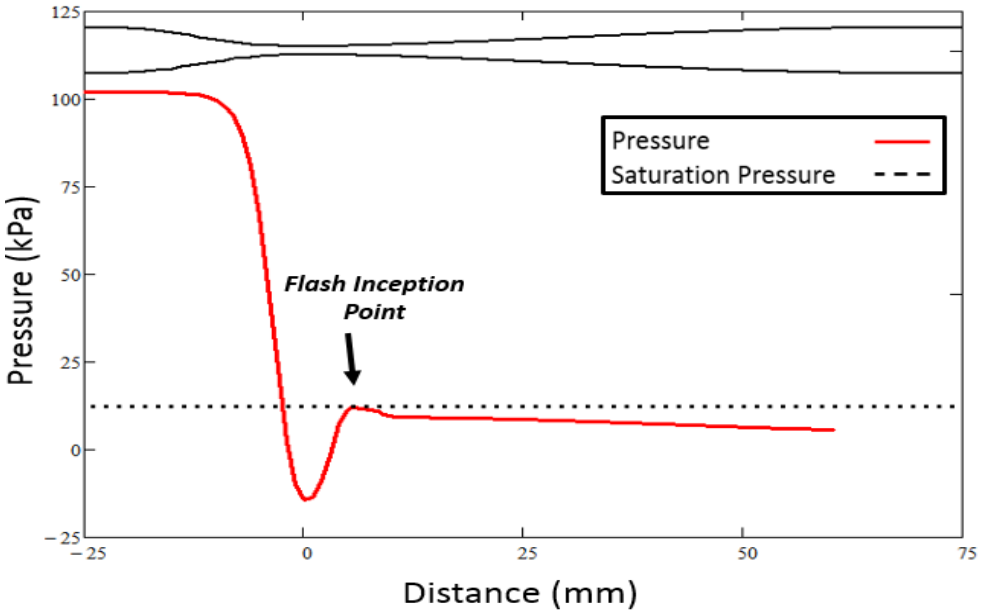

Figure 4.16 Pressure distribution as a function of distance in the converging diverging nozzle for a temperature of 50 ℃ under cavitating conditions.

4.3 Length of Two-Phase "Condensation Shock" Results

Determination of the length of the two-phase region represents the final step in the model development to predict the results of the cavitation phenomena in the converging-diverging nozzle, and completely describe the behavior of the pressure distribution from the nozzle inlet to the outlet. This section will compare the length of two-phase region that was experimentally measured by Ahmed [23] with the predictions from the model developed in the current analysis. Ahmed's data was presented in Figure 1.13 for water flows at temperatures of 70 ℃, 50 ℃, and 25 ℃. As seen from Figure 4.15 and Figure 4.16, the supersonic pressure distribution decreases as it travels in the diverging section. After a certain distance away from the throat and depending on the backpressure, the pressure trend is terminated abruptly by a condensation shock and the flow instantaneously deaccelerates until it reaches single-phase liquid flow. It is further observed that the location of the condensation shock is dependent on the backpressure. This section presents the predictions of the condensation shock locations in the diverging section for various backpressures. Also included is the effect of the backpressure on the length of two-phase region in the nozzle, which ultimately affects the cooling potential of a given nozzle.

In chapter 3, an analysis was introduced to calculate the upstream and downstream properties of the condensation shock using two different numerical solution methods; that is, the backward marching procedure and the forward marching procedure. The backward procedure uses the backpressure and the outlet area as the input parameter to calculate the single-phase pressure values. The forward procedure uses the flash wave analysis results shown in the previous section to calculate the proprieties from state 3 to state 4 at different points on the supersonic pressure distribution shown in Figure 3.11. Once both results of the backward and forward procedure are obtained, they are plotted in the same figure in terms of pressures as a function of area. Results show both lines intersecting at a specific area, which corresponds to the exact distance where the condensation shock terminates in the diverging section of the nozzle. From the nozzle polynomial profile fit, this area then corresponds to the position from the throat to the shock. Finally, the length of the two-phase region is determined by subtracting the distance to the flash inception point from the distance to the condensation shock.

The prediction of the locations of the condensation shock for the previous water experiments flowing through a converging-diverging nozzle at a temperature of 70 ℃ is given in Figure 4.17 for different backpressures. Similar to the previously referenced experimental work, backpressures of 67 kPa, 57 kPa, 47 kPa, and 37 kPa were used in the numerical model for comparison with the measured locations of the shock and the measured lengths of two-phase region. Figure 4.17 shows the pressure distribution as a function of area for a temperature of 70 ℃ , the black curve represents the values of pressure at state 4 determined from the forward marching procedure applied to the supersonic region. The four different curves crossing the black curves, are the results of the backward marching procedure for the four different backpressures in the subcooled region starting from the outlet of the converging-diverging nozzle. Figure 4.17 also shows the nozzle geometry downstream of the throat and the saturation pressure level. For each curve of backpressure, there is an intersection between the black curve that corresponds to a value of pressure and area in the nozzle. This intersection determines the predicted location of the condensation shock for the given value of backpressure as explained in details in Appendix (B). The distance between this condensation shock position and the flash point position determines the length of the two-phase regions for each backpressure. Downstream of the condensation shock, a subsonic subcooled liquid flow persists for the

remainder of the diverging section of the nozzle. If there is no intersection in the forward and backward differencing, then a condensation shock does not occur in the nozzle and the flow remains in the supersonic region, exiting as two-phase flow at the end of the diverging section of the nozzle. This behavior is predicted for values of backpressures less than 31 kPa and was visualized in the experimental work [27], where the flow never condensed back to single-phase subcooled liquid for a backpressure of 30 kPa at a temperature of 70 ℃. For the second set of experimental test data, corresponding to a temperature of 50 ℃, the condensation shock location was similarly predicted for six different backpressures at 67 kPa, 57 kPa, 47 kPa, 37 kPa, 27 kPa and 16 kPa. Results for the shock location at a temperature of 50 ℃ are shown in Figure 4.18.

Finally, the above analysis procedure was applied to the last set of experimental data corresponding to a temperature of 25 ℃. The condensation shock location was predicted for eight different backpressures: 60 kPa, 54 kPa, 47 kPa, 40 kPa, 33 kPa, 26 kPa, 19 kPa and 16 kPa. Results for the shock location at a temperature of 25 ℃ are shown in Figure 4.19.

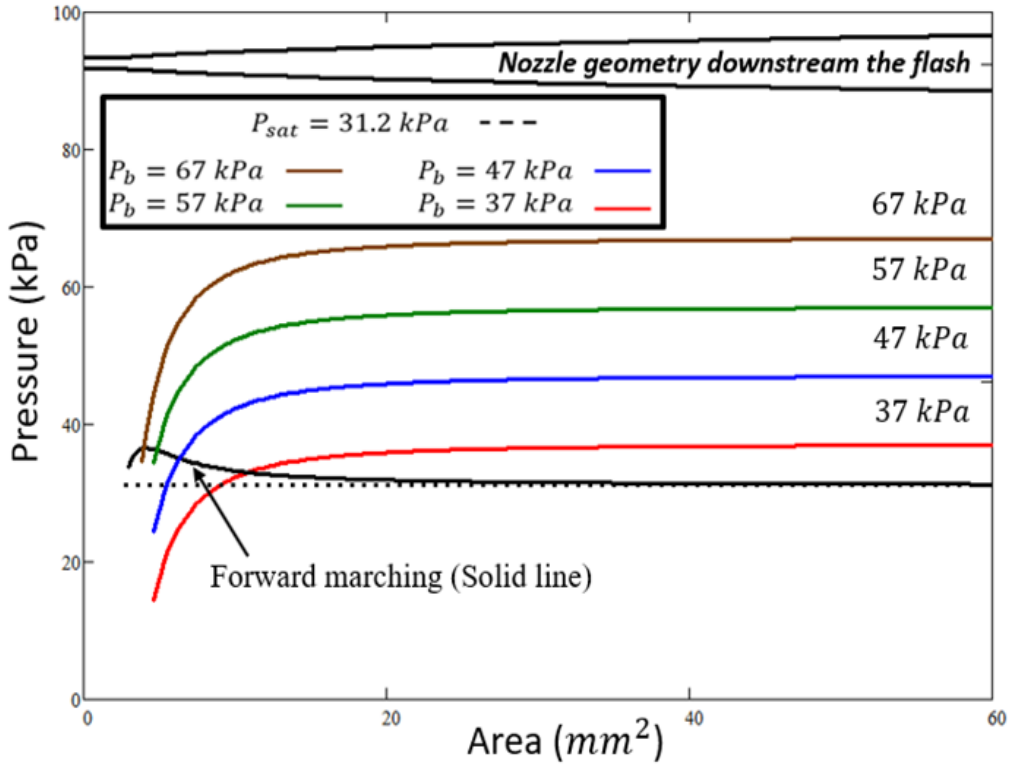

Figure 4.17 Condensation shock prediction for a temperature of 70 ℃ for four different back pressures

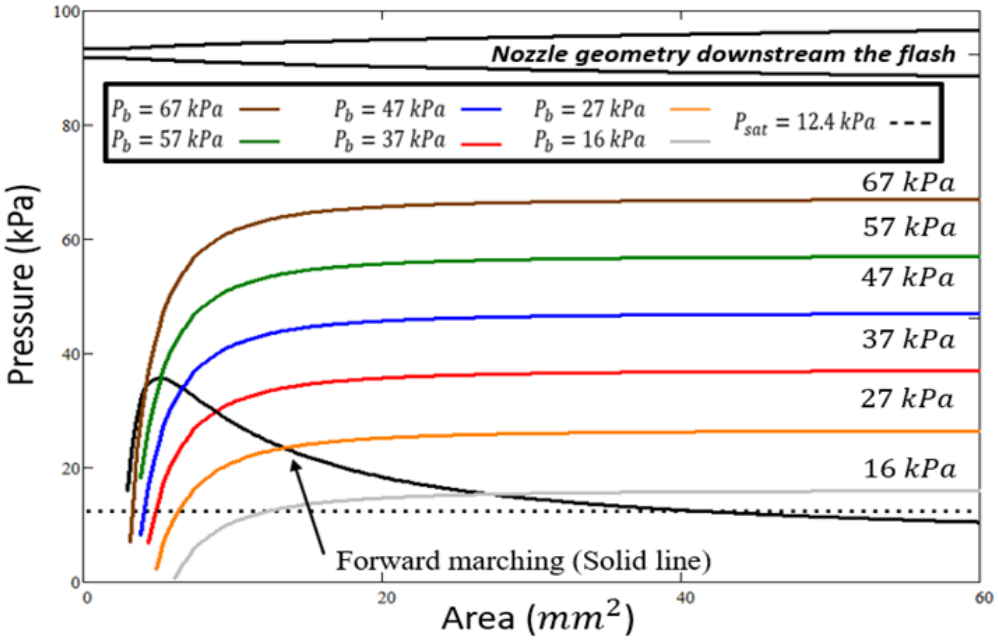

Figure 4.18 Condensation shock prediction for a temperature of 50 ℃ for six different back pressures

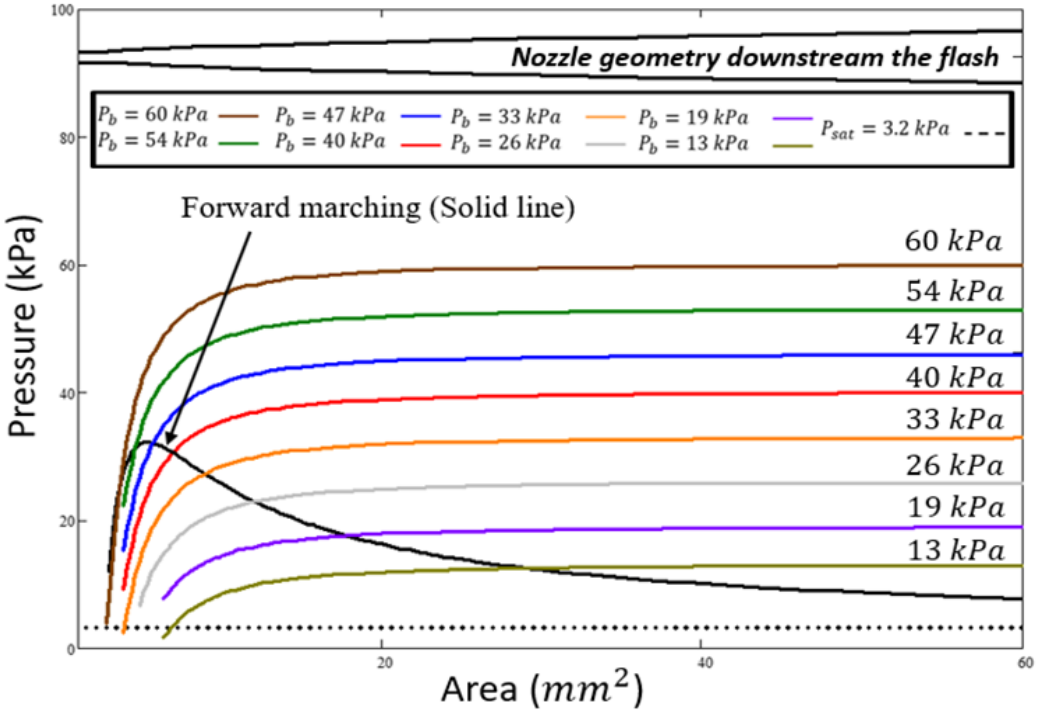

Figure 4.19 Normal shock prediction for a temperature of 25 ℃ for eight different back Pressures

As seen from the results presented in Figures 4.17, 4.18, and 4.19, the condensation shock occurs downstream of the throat for all tested backpressures. From the aforementioned numerical predictions, it appears that the backpressure must be above the saturation pressure and less than the inlet pressure for the condensation shock to occur in the diverging section of the converging-diverging nozzle, otherwise the flow will continue as two-phase flow throughout the diverging section of the nozzle. Results show that as the backpressure is decreased, the condensation occurs closer to the outlet section of the nozzle; therefore, at a further distance from the throat. Figure 4.20 shows the pressure distribution as a function of distance in the nozzle for a temperature of 70 ℃, and includes the predicted condensation shock location for four different backpressures. The schematic diagram of the converging-diverging nozzle geometry is included in the figure to indicate the relative location within the nozzle, and to depict the corresponding pressure behavior in the nozzle for the four different backpressures. Figure 4.21 shows the pressure distribution as a function of distance in the nozzle for a temperature of 50 ℃. Results of the model show the predicted pressure distribution behavior along the converging-diverging nozzle for all the given experimental conditions.

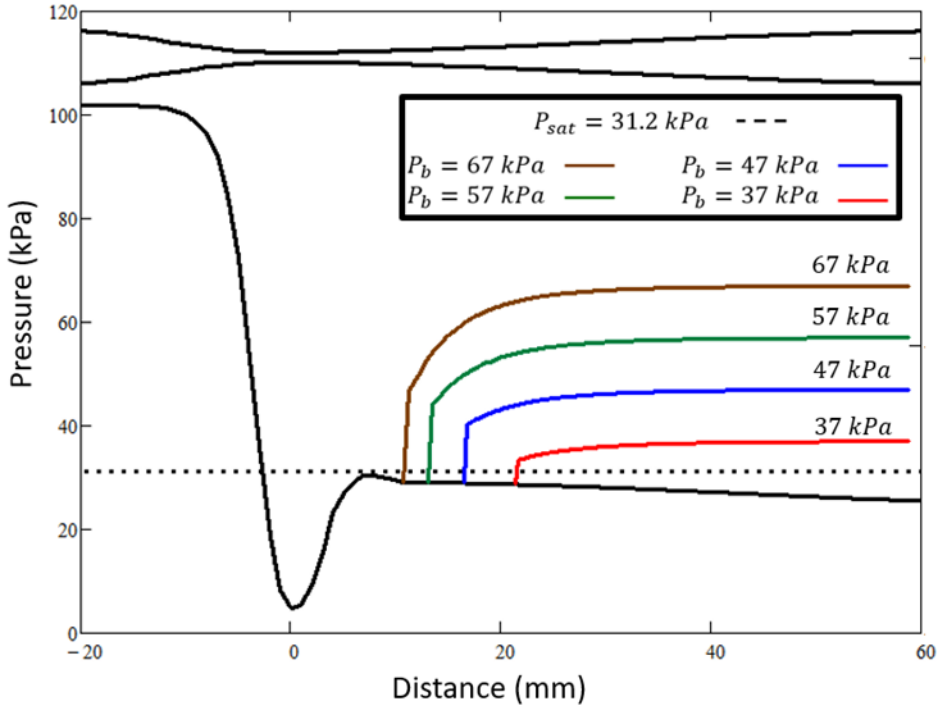

Figure 4.20 Prediction of the pressure distribution vs. distance in the converging-diverging nozzle for a temperature of 70 ℃

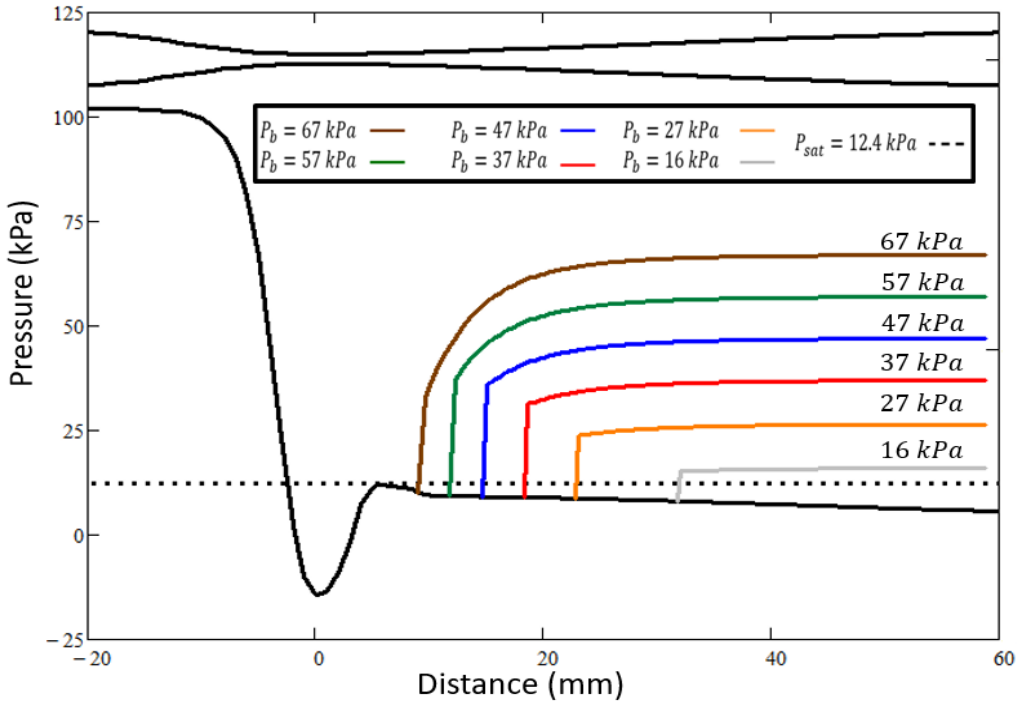

Figure 4.21 Prediction of the pressure distribution vs. distance in the converging-diverging nozzle for a temperature of 50 ℃

Once the prediction of the position where the condensation shock occurs in the diverging section of the nozzle is determined, the length of two-phase region can be calculated as described earlier. Finally, the results are compared to the experimental results for water with temperatures of 70 ℃, 50 ℃, and 25 ℃. Figure 4.22 shows the results of the comparisons between the model predictions and the experimental points for the length of two-phase region as a function of absolute backpressure for a temperature of 70 ℃. The proposed model shows good agreement with the experimental results. It is also clear that the length of two-phase region increases as the backpressure is decreased, which is consistent with the experimental flow visualization results that took place in the glass nozzle [23].

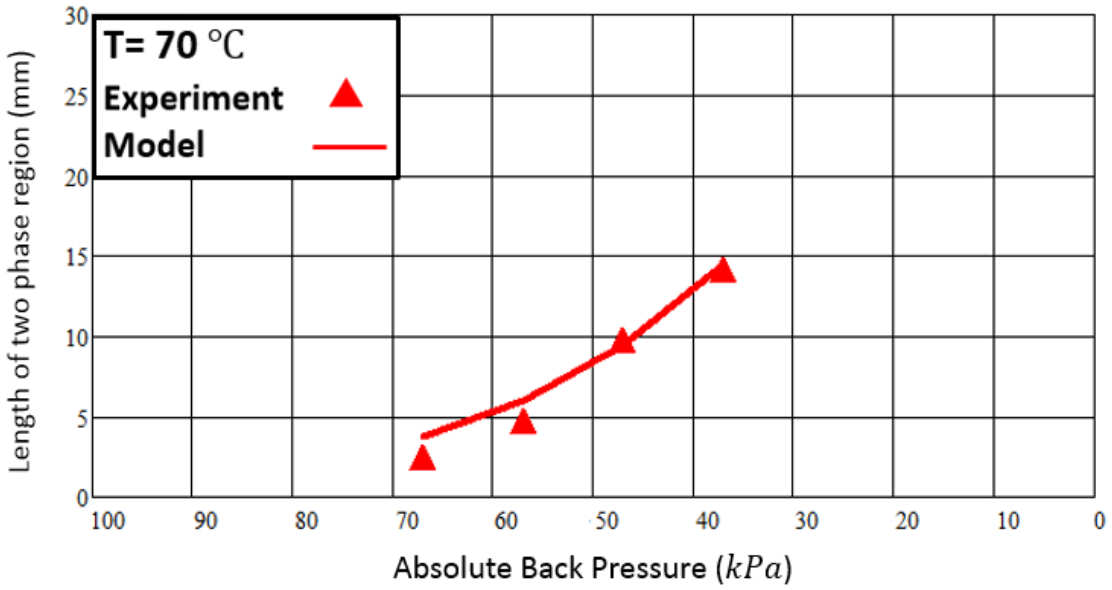

Figure 4.22 Comparisons of the experimental results [23] and predictions for the length of two-phase region as a function of backpressure for a temperature of 70 ℃ (current model)

The comparisons between experimental and predicted results for the length of the two-phase region as a function of absolute backpressure for a temperature of 50 ℃ is shown in Figure 4.23. The proposed model shows fair agreement with the experimental results. In particular, the trend of the predictions follows the trend of the data, with the predictions a few mm above the measured length of the two-phase region.

Finally, Figure 4.24 shows the comparison between experimental and predicted results for the length of two-phase region as a function of absolute backpressure for a temperature of 25 ℃. Result show a fair agreement with the experimental results, including the correct trend of the data with the predictions a few mm above the measurements. The results presented in Figures 4.22, 4.23, and 4.24 all show that as the backpressure is reduced, the length of two-phase region is increased.

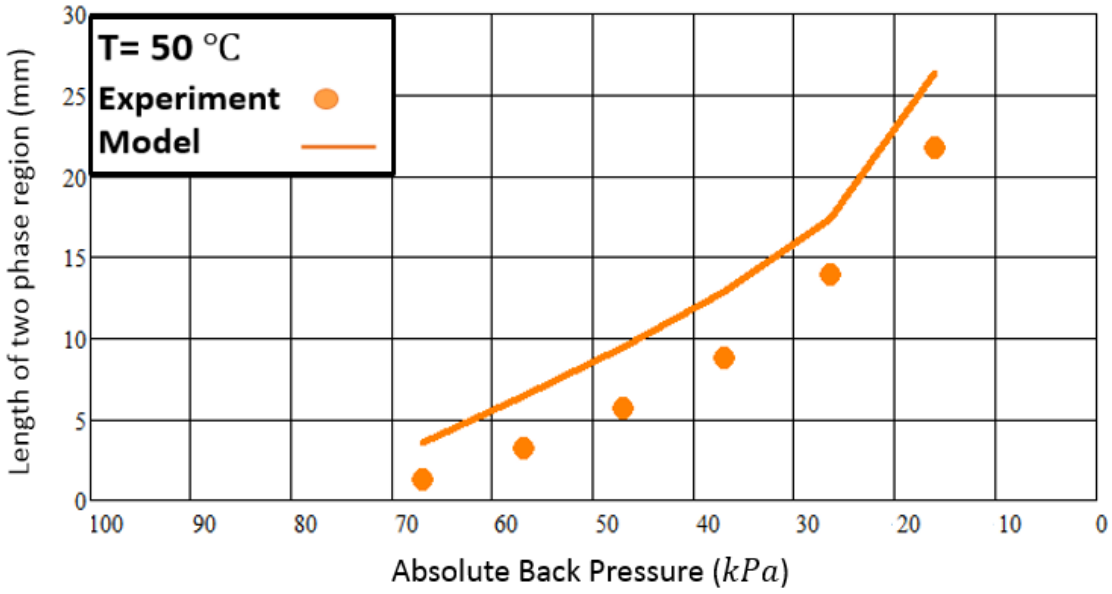

Figure 4.23 Comparisons of the experimental results [23] and predictions for the length of two-phase region as a function of backpressure for a temperature of 50 ℃ (current model)

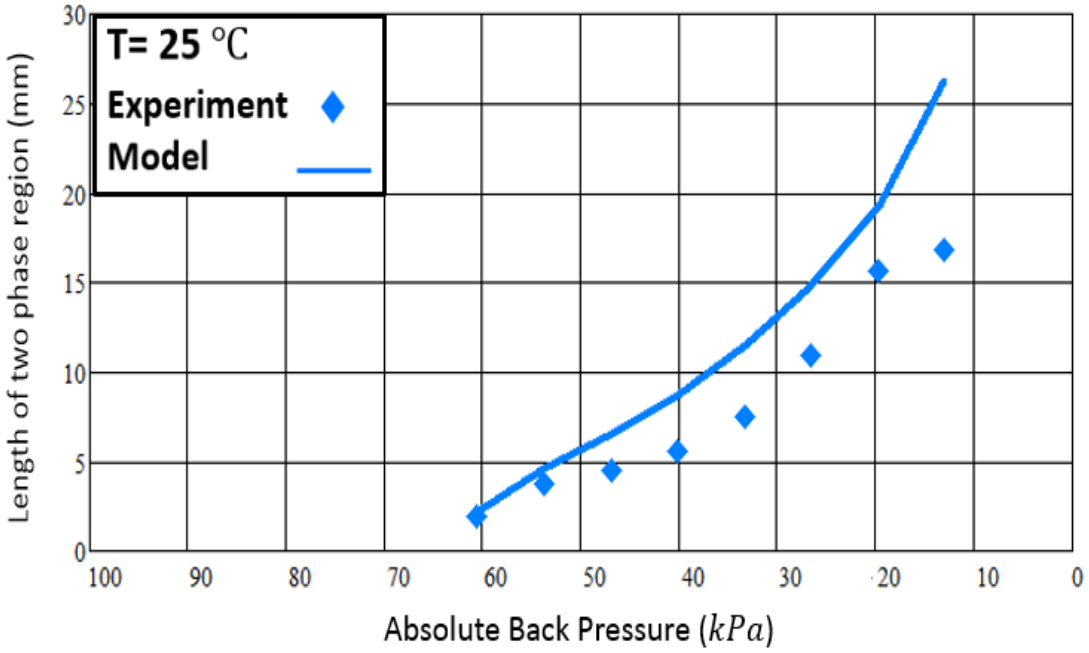

Figure 4.24 Comparisons of the experimental results [23] and predictions for the length of two-phase region as a function of backpressure for a temperature of 25 ℃ (current model)

The predicted length of two-phase region for water flowing in a converging-diverging nozzle with temperatures of 70 ℃, 50 ℃, and 25 ℃ compared with experiments is shown in Figure 4.25. The theoretical model shows fair agreements with the experimental results with respect to the slope of the change but it does not match the experimental values. Figure 4.25 shows as the temperature increases, the curves shift to the lift and at a given backpressure, the length of two-phase increases as the temperature increases. The model can be used to evaluate and optimize the best nozzle geometry to achieve maximum cooling potential for water through converging-diverging nozzles by achieving the largest length of two-phase region.

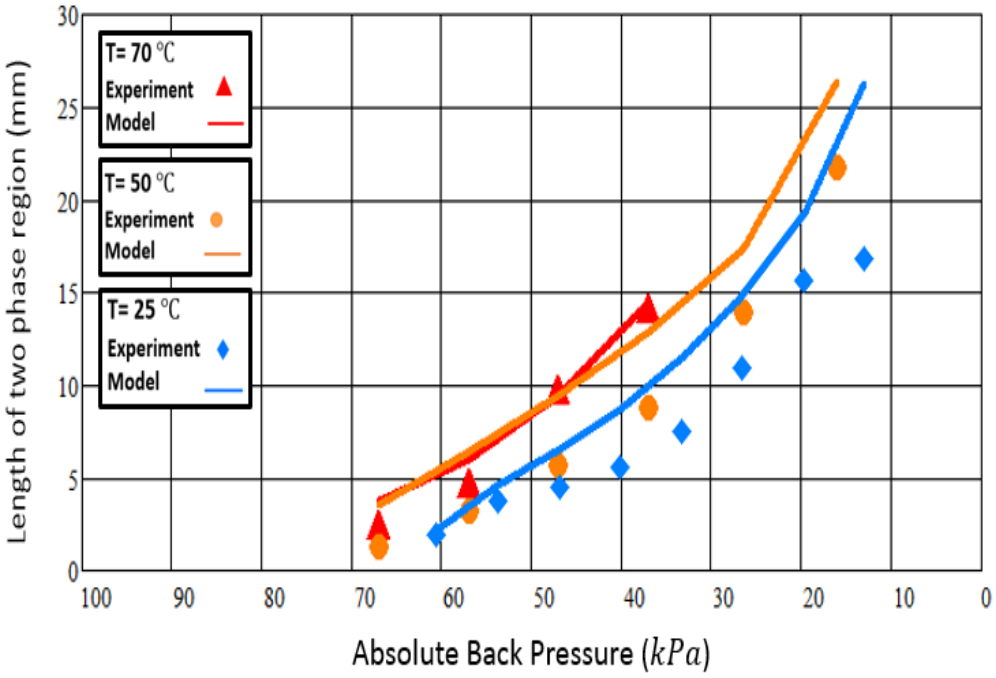

Figure 4.25 Variation of the length of two-phase region as a function of back pressure for all temperatures

Chapter 5 - Summary, Conclusions, and Recommendations

The results for the investigation of water flow through a converging-diverging nozzle are summarized and presented in this chapter. Recommendations for continuation of this work in the future are offered in this chapter as well.

5.1 Summary and Conclusions

The main objective of this research project was to explore the possibility of developing a water-based non-vapor compression cooling system by investigating the flash phenomena for water flow through converging-diverging nozzles. Cavitation can occur when the static pressure of the fluid falls below the vapor pressure, into a metastable liquid state. The research work presented in this dissertation focusses largely on the development of a comprehensive theoretical model and evaluation techniques to predict the two-phase flow and cavitation phenomena in the diverging section of a converging-diverging nozzle and the effect of developing cavitation in the flow. The proposed comprehensive theoretical model evaluates both the converging and diverging sections of the nozzle in developing a complete model for fluid flow through the entire converging-diverging nozzle. Several types of numerical analyses were used to evaluate flow behavior in the different sections of the converging-diverging nozzle. These include single-phase pressure distribution analysis, flash inception analysis, flash cavitation wave analysis, and condensation shock analysis. Using a marching algorithm approach, the models were used to predict the pressure distribution as a function of distance throughout the entire nozzle. This spanned from the inlet to the throat for the single-phase liquid water, and from the throat to the outlet, which involved both single-phase liquid water flow and two-phase flow regions. For a constant mass flow rate, the modeling accounted for the onset of cavitation, when the backpressure was dropped sufficiently, and included a prediction of the length of the two-phase region in the diverging section of the nozzle.

Two 5^{th} order polynomials were used to separately fit the dimensions (radius distribution) of the converging and diverging sections of the nozzle. These polynomial approximations represent the geometry of the glass nozzle used in Ahmed's experimental set up

[23], as well as the transparent resin nozzle used in Gallman's experimental work [24]. These nozzle profiles were needed to generate the theoretical analysis for comparison with experimental results. The glass nozzle used in the experimental work had both an inlet and an outlet diameter of 9.3 mm, a converging section with a length of 25 mm up to the throat, a diverging section with a length of 73 mm from the throat to the outlet of the nozzle, and a nozzle throat with a diameter of 1.7 mm.

The pressure distribution from the inlet to the point of flash inception was predicted using a mechanical energy balance model with the assumption of single-phase one-dimensional liquid water flow through the converging section of the nozzle. Two versions of this model were presented; one for frictionless flow and one accounting for frictional head losses. Each of these models consisted of a finite sectioning off of the nozzle in the axial direction and utilizing a pipe flow approximation for the frictional head loss within each section. This model did not account for fluid separation or the "Vena contracta" effect; thus, it only provided reasonable predictions, up to the point of cavitation inception, in the converging section of the nozzle where these effects are not present.

A flash inception analysis was used to predict the onset of flash, which represents the location of a phase transition from single-phase liquid to two-phase mixture for a given set of flow conditions. The point of flash inception is predicted by evaluating a modified dynamic flash inception line as a function of the depressurization rate for each experimental data set. Flash inception is considered to take place when the pressure undershoot, defined as the difference between the saturation pressure and the local pressure, crosses the modified dynamic inception line. The modified dynamic flash inception line analysis modified the static flash inception line introduced by Jones [26] by incorporating a total depressurization rate, along with the effects of turbulence and area ratio, in the converging section of the nozzle [36]. The reproduction of Abuaf's [27] results was used to verify the accuracy of the marching procedure developed for the dynamic flash inception analysis. Then, in conjunction with the marching analysis, the modified dynamic flash inception line analysis was used to predict the flash inception line for Brown's experimental data [28] for water inlet temperatures of 270°C and 286°C. For the current modified dynamic flash inception line analysis, turbulence intensities

ranging between 0.07 and 0.12 were used; however, results showed that these levels of turbulence intensity had a minimal effect on the flash inception line and hence a minimal effect on the flash inception point.

Following verification of the modified dynamic flash inception line analysis, it was applied to Ahmed's [23] experimental test results obtained for water flow through a glass converging-diverging nozzle for inlet temperatures of 70 ℃, 50 ℃, and 25 ℃. The results of this marching analysis showed that the experimental data superheats intersected with the modified dynamic flash inception line at an axial position corresponding to nearby the throat, indicating that flash inception occurred at a location close to the throat of the nozzle.

Gallman [24] used a nozzle manufactured from a transparent resin material. His converging- diverging nozzle was identical in size and shape to the glass nozzle used by Ahmed [23]. In addition, his nozzle was able to include machined pressure taps along both the converging and the diverging sections of the nozzle. He obtained experimental data for water with an inlet temperature of 20 ℃ and three different backpressures of 43.2 kPa, 30.5 kPa, and 15.2 kPa. The modified dynamic flash inception line analysis performed for his test conditions showed that the experimental pressure depression lines didn't cross the flash inception lines, even though flash inception was visually observed by Gallman in the nozzle using a laser light flow visualization technique. After careful analysis, it was observed that the mass flow rate ($0.0248\frac{kg}{s}$) in Gallman's experiments was lower than the mass flowrate ($0.0349\frac{kg}{s}$) in Ahmed's experiments, resulting in lower range of the depressurization rates and higher levels of pressure distribution in the nozzle. The visual observation of flash inception at a much lower mass flow rate can be explained by hypostasizing that the pressure tap drilled in the 3D transparent resin nozzle at the throat produced a small burr on the inside surface of the nozzle, causing premature flash inception at the throat tap. As a follow-up to this observation, the flash inception analysis for Gallman's experimental test conditions were repeated using the larger mass flow rate associated with the testing by Ahmed. The results showed that using Ahmed's larger mass flowrates for Gallman's nozzle, with the same 20 ℃ inlet water temperature, the modified dynamic flash inception line analysis accurately predicted flash occurring at, or very close to, the throat.

After the flash inception point was accurately predicted, the next step was to introduce the flash/cavitation analysis in downstream of the diverging section of the nozzle. A numerical solution was developed by applying the equations of conservation of mass, momentum, and energy to a control volume associated with the fluid particle moving from z to $z+\Delta z$ location in the diverging section of the nozzle. The numerical solution assumes a constant mass flow rate based on the experimental test conditions used by Ahmed [23]. The homogenous equilibrium model (HEM) was used in the analysis to determine the pressure distribution in the diverging section of the nozzle as a function of distance. Following the flash inception point, which was predicted to occur downstream of the throat, a subsonic flow or a supersonic flow can develop depending on the Mach number. According to the differential analysis, given in Equations (2.56) and (2.59), if the Mach number is less than one, subsonic flow conditions will exist just downstream of the cavitation point. In this case, the flow decelerates causing pressure to increase to the saturation pressure and condense to liquid before exiting the nozzle. If the Mach number is greater than one, supersonic conditions occur. The flow accelerates in the diverging section of the nozzle from a Mach number greater than one causing the pressure to drop as the area increases. Modifying the differential analysis by incorporating friction was used to predict the pressure distribution for the supersonic region. An observation was made during the experimental flow visualization that the flash inception occurred at approximately 4 mm and up to 5 mm downstream of the throat considering the "Vena Contracta" effect. For the analysis purposes, it was simply assumed that the flash inception occurred at a fixed 4 mm downstream of the throat. For simplicity, a pressure close to the saturation pressure was used as the flash inception point for the analysis. Two different models of the speed of sound, the friction factor, and two-phase frictional pressure drop models were investigated in conjunction with the two-phase supersonic flow analysis. The Friedel two-phase pressure drop model [20], the Franc speed of sound equation [15], and the friction factor based on a simplified diffuser model [18] appeared to give the best results for predicting the length of two-phase region and were therefore implemented in the analysis. After calculating the pressure distribution for the supersonic region, results showed that the pressure was slowly decreasing in the supersonic region. Regardless of the inlet temperature of the water, the pressure drop was very small in the supersonic region of the nozzle, similar to the experimental measurements conducted by Ahmed [23].

The condensation shock model was developed by defining a control volume with a cross-sectional area normal to the flow direction. The shock was considered perpendicular to the nozzle flow direction. Two different numerical solution methods were used to predict the location of the condensation shock. A forward procedure was used in the upstream supersonic two-phase region. The pressure and location from the flash wave analysis results were used as an input to calculate the supersonic pressure distribution. A backward marching procedure used the backpressure and the outlet area as input parameters to calculate the single-phase pressure distribution downstream of the condensation shock. Once both results of the backward and forward procedure were obtained, they could be plotted in the same figure in terms of pressures as a function of area. The point where they intersect corresponded to a prediction of the location of the condensation shock for a given backpressure. The pressure distributions as a function of distance were plotted for temperatures of 70 ℃, 50 ℃, and 25 ℃. Results show that as the backpressure is decreased, the condensation shock terminates closer to the outlet section of the nozzle. Therefore, longer two-phase regions were observed downstream of the throat as the backpressure was reduced. The length of two-phase region was calculated as the distance from the flash inception to the condensation shock. Comparisons between the developed model predictions for the two-phase region length, and the experimental measurements for water with temperatures of 70 ℃, 50 ℃, and 25 ℃, all showed good agreement. The predictions showing that the length of two-phase region increased as the backpressure decreased were in agreement with the experimental glass nozzle flow visualization results [23].

.

5.2 Recommendations and Future Work

A comprehensive theoretical model for the converging-diverging nozzle was developed using available experimental data. The developed comprehensive model analysis could be used to optimize the nozzle geometry to achieve the maximum length of two-phase region providing a greater area for heat absorption, hence, a greater cooling potential. It is recommended that more experimental data with improved direct pressure measurement capability for water flowing through converging-diverging nozzles be explored. It would be useful to obtain experimental pressure distribution data throughout the converging-diverging nozzle using different inlet and backpressure test conditions for a few different inlet water temperatures. The expanded experimental data sets complemented with flow visualization for the onset of flash and the length of two-phase region can be useful for developing a general model to predict the pressure distribution throughout the nozzle. The model, verified by comparison with additional experimental data, should be useful for flow of other fluids in converging-diverging nozzles, determining the flash inception point and the length of the two-phase region, which are needed to estimate performance for cooling applications. Furthermore, such a model could be further analyzed for different nozzle geometries, to predict and achieve the maximum length of two-phase region for water and other fluids. The best nozzle geometry could then be manufactured for experimental testing to verify the achievable length of two-phase region. The model could be further developed by attempting to predict the pressure distribution for different fluids, and comparing with experimental results. The range of low temperatures for water used in the work resulted in very high void fraction and quality to obtain even a small and insignificant temperature drop; therefore, higher temperatures for water could be explored to provide more measurable results.

References

[1] Alkotami, A., Beck, T., Sorensen, C. M., Hosni, M. H., Eckels, S. J., & Tomasi, D. (2015). A Thermodynamic Analysis of the Temperature Drop and Potential Cooling Effect of Cavitation. Proceedings of IMECE 2015

[2] Brennen, Christopher E. Cavitation and bubble dynamics. Cambridge University Press, 2013.

[3] Davis, Michael P. Experimental investigation of the cavitation of aviation fuel in a converging-diverging nozzle. ProQuest, 2008.

[4] Nakagawa, Masafumi, Menandro Serrano, and Atsushi Harada. "Shock waves in supersonic two-phase flow of CO2 in converging-diverging nozzles." (2008).

[5] Schneider, Brandon, et al. "Cavitation enhanced heat transfer in microchannels." Journal of Heat Transfer 128.12 (2006): 1293-1301

[6] Wang, Yi-Chun, and Christopher E. Brennen. "One-dimensional bubbly cavitating flows through a converging-diverging nozzle." Journal of fluids engineering 120.1 (1998): 166-170.

[7] Wilms, Jeffrey. Flow Visualization of Cavitation. MS Thesis. Kansas State University, Manhattan, 2013.

[8] Awad, Mohamed. Two-Phase Flow Modeling in Circular Pipes. Doctoral Thesis. Memorial University of Newfoundland, Canada, 2007.

[9] Salvador, F.J., et al. "Using a homogeneous equilibrium model for the study of the inner nozzle flow and cavitation pattern in convergent–divergent nozzles of diesel injectors." Journal of Computational and Applied Mathematics 309 (2017): 630-641

[10] Jung Seob KIM and Heather Jean DUNSHEATH. A homogeneous equilibrium model improved for pipe flows. Proceedings of the World Congress on Engineering and Computer Science (WCECS 2010), 2, October 2010.

[11] Alok, P., Sahu, D.: Numerical simulation of capillary tube for selected refrigerants using homogeneous equilibrium model. Int. J. Air Cond. Refrig. 27, 1950001 (2019)

[12] Stewart H. B., & Wendroff B., (1984) “Two-Phase Flow: Models and Methods”. Journal of Computational Physics, 56, 363-409.

[13] Lockhart, R. W., and Martinelli, R. C., 1949, "Proposed Correlation of Data for Isothermal Two-Phase, Two-Component Flow in Pipes," Chemical Engineering Progress Symposium Series, 45 (1), pp. 39-48.

[14] Wallis G. One-dimensional two-phase flow. New York: McGraw-Hill; 1967.

[15] Franc, Jean-Pierre. Physics and control of cavitation. (Grenoble univ. (France), 2006)

[16] Weisman.J, "Chapter 15 Two-phase flow patterns," in Handbook of Fluids in Motion, Ann Arbor, Mich. Ann Arbor Science, 1983.

[17] Kim S.-M., Mudawar I. (2014). Review of databases and predictive methods for pressure drop in adiabatic, condensing and boiling mini/micro-channel flows, International Journal of Heat and Mass Transfer, 77, 74-97.

[18] Blevins RD: Applied Fluid Dynamics Handbook. Van Nostrand Reinhold, New York, 1984

[19] Chisholm D. (1967). A theoretical basis for the Lockhart-Martinelli correlation for two-phase flow, International Journal of Heat and Mass Transfer, 10, 1767-1778.

[20] Friedel L. (1979). Improved friction pressure drop correlations for horizontal and vertical two-phase pipe flow, In European Two-Phase Group Meeting, Ispra, Italy, Paper E2.

[21] Dalkilic A.S., Agra O., Teke I., Wongwises S. (2010). Comparison of frictional pressure drop models during annular flow condensation of R600a in a horizontal tube at low mass flux and of R134a in a vertical tube at high mass flux, International Journal of Heat and Mass Transfer, 53, 2052-2064.

[22] Filip, Alina, Băltăreţu, Florin, and Damian, Radu-Mircea (2014), 'Comparison of Two-Phase Pressure Drop Models for Condensing Flows in Horizontal Tubes', Mathematical Modelling in Civil Engineering (10), 19

[23] Ahmed, Z. (2017). Quantitative flow measurement and visualization of cavitation initiation and cavitating flows in a converging-diverging nozzle. M.S. Thesis, Mechanical and Nuclear Engineering Kansas State University

[24] Gallman, B. (2019). Steady and metastable cavitation in a converging-diverging nozzle. M.S. Thesis, Mechanical and Nuclear Engineering Kansas State University

[25] Alamgir, Md., and Lienhard, H. H., Personal communication (1979); "Correlation of Pressure Undershoot During Hot-Water Depressurization," J. Heat Transfer, in press.

[26] Jones, O. C., JR., "Flashing Inception in Flowing Liquids," BNL-NUREG-26134 (1979).

[27] Wu, B.J.C.; Abuaf, N.; Saha, P. (1981), A study of nonequilibrium flashing of water in a converging-diverging nozzle: Volume 2 – Modeling. U.S. Nuclear Regulatory Commission, Washington, D. C

[28] Brown, R. A., "Flashing Expansion of Water Through a Converging-Diverging Nozzle," UCRL-6665-T (1961).

[29] Soyama, H. and Hoshino, J. (2016). Enhancing the Aggressive Intensity of Hydrodynamic Cavitation through a Venturi Tube by Increasing the Pressure in the Region Where the Bubbles Collapse. AIP Advances 6(045113), 1-13.

[30] Munson, B. R. (2015). Fundamentals of fluid mechanics

[31] Eric W. Lemmon, Mark O. McLinden and Daniel G. Friend, "Thermophysical Properties of Fluid Systems" in NIST Chemistry WebBook, NIST Standard Reference Database Number 69, Eds. P.J. Linstrom and W.G. Mallard, National Institute of Standards and Technology, Gaithersburg MD, 20899, https://doi.org/10.18434/T4D303, (retrieved September 20, 2012).

[32] R. Revellin, S. Lips, S. Khandekar, J. Bonjour, Local entropy generation for saturated two-phase flow, Energy 34 (9) (2009) 1113–1121.

[33] Macias, L C, and Ramey, Jr, H J. Multiphase, multicomponent compressibility in petroleum reservoir engineering. United States: N. p., 1986.

[34] G.A. Melhem, A systematic approach to relief and flare systems evaluation, Process Saf Prog 32 (2013).

[35] A. Bejan, Advanced Engineering Thermodynamics, 2nd edn, Wiley, New York, 1997

[36] Abuaf N, Jones OC, Wu BJC (1983) Critical flow in Nozzles with sub-cooled inlet conditions. J Heat Transfer 105:379–383

[37] Team XYZ. (2019, June 5). Womp.xyz: Make your 3D printing ideas a reality.

Retrieved from https://gen.xyz/blog/wompxyz

[38] Simões-Moreira, J.R., and C.W. Bullard. 2003. Pressure drop and flashing mechanisms in refrigerant expansion devices. International Journal of Refrigeration 26(7):840–48

Appendix A - Isobaric Thermal Expansion Coefficient

The isobaric thermal expansion coefficient, used in Equation (3.25), is defined by

$$\beta = \frac{1}{v}\left(\frac{\partial v}{\partial T}\right)_P \tag{A.1}$$

where v is the specific volume, T is the temperature, and P is the pressure. The thermal expansion coefficient for the homogeneous two-phase mixture can be evaluated starting with the two-phase mixture specific volume given by

$$v = Qv_g + (1 - Q)v_f \tag{A.2}$$

The rate of change in the specific volume with respect to temperature at a constant pressure is given by

$$\left(\frac{\partial v}{\partial T}\right)_P = Q\left(\frac{\partial v_g}{\partial T}\right)_P + (1 - Q)\left(\frac{\partial v_f}{\partial T}\right)_P \tag{A.3}$$

Substituting Equation (A.2) and (A.3) into (A.1), yields

$$\beta = \frac{Q\left(\frac{\partial v_g}{\partial T}\right)_P + (1-Q)\left(\frac{\partial v_f}{\partial T}\right)_P}{Qv_g + (1-Q)v_f} \tag{A.4}$$

In the mixture region the pressure and temperature are locked together resulting in the specific volumes being only a function of temperature; therefore, the relations for the liquid, β_f and vapor, β_g isobaric thermal expansion coefficient are given by

$$\beta_f = \frac{1}{v_f}\left(\frac{\partial v_f}{\partial T}\right)_P = \frac{1}{v_f}\left(\frac{dv_f}{dT}\right)_P \tag{A.5}$$

$$\beta_g = \frac{1}{v_g}\left(\frac{\partial v_g}{\partial T}\right)_P = \frac{1}{v_g}\left(\frac{dv_g}{dT}\right)_P \tag{A.6}$$

Substituting Equation (A.5) and (A.6) into (A.4), the final relation for the mixture isobaric thermal expansion coefficient can be written as

$$\beta = \frac{Qv_g\beta_g + (1-Q)v_f\beta_f}{Qv_g + (1-Q)v_f} \tag{A.7}$$

Values for the thermal expansion coefficient of liquid and vapor phases can be evaluated by Refprop and the (NIST) webbook [31]. Figure (A.1) shows the isobaric thermal expansion coefficient for water in liquid phase using the values given by (NIST) tables and compared to the values calculated by an equation introduced by Melhem [34].

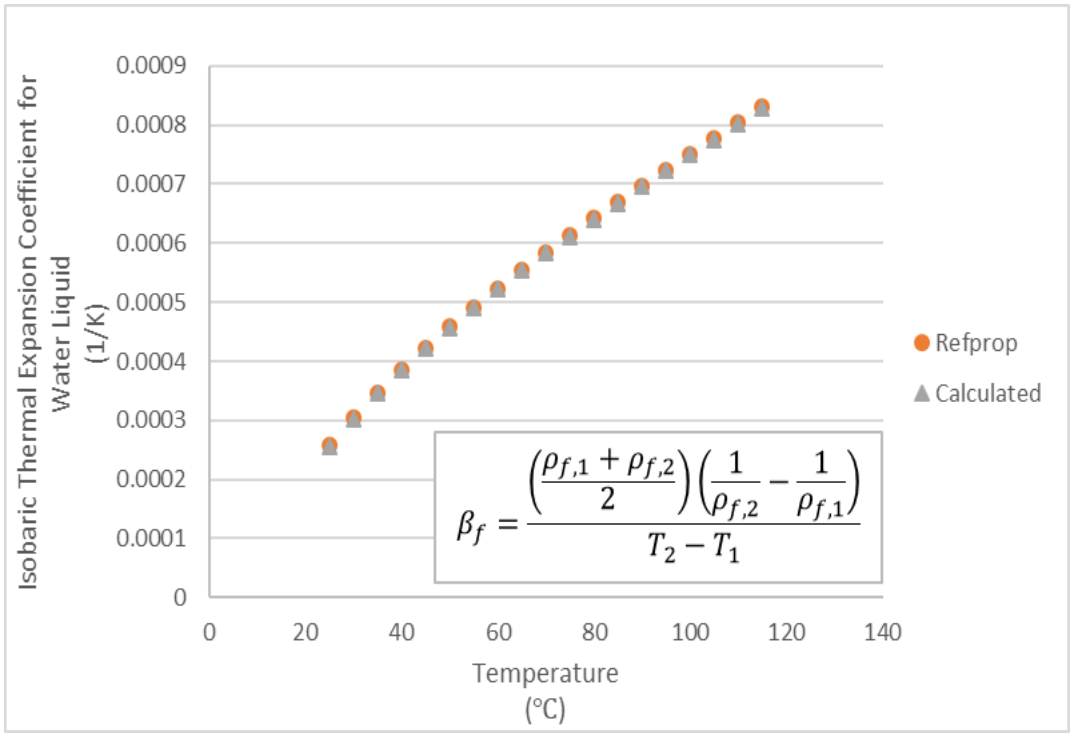

Figure A.1 Comparisons of the isobaric thermal expansion coefficient for water liquid as a function of temperature

Figure (A.2) shows a comparison between the isobaric thermal expansion coefficient for water vapor taken from (NIST) values and the values calculated by the Van der Waals equation of state introduced by Bejan [35].

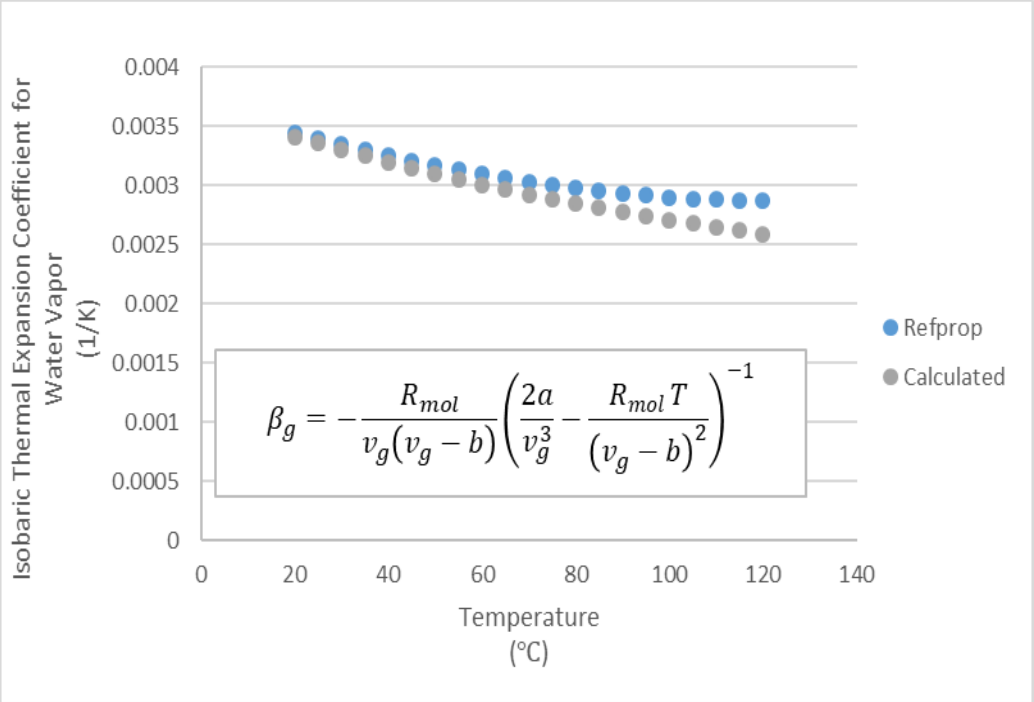

Figure A.2 Comparisons of the isobaric thermal expansion coefficient for water vapor as a function of temperature

Finally, the mixture isobaric thermal expansion coefficient for water can be calculated and compared to the separate liquid and vapor thermal expansion coefficients taken from (NIST) values, as shown in Figure A.3.

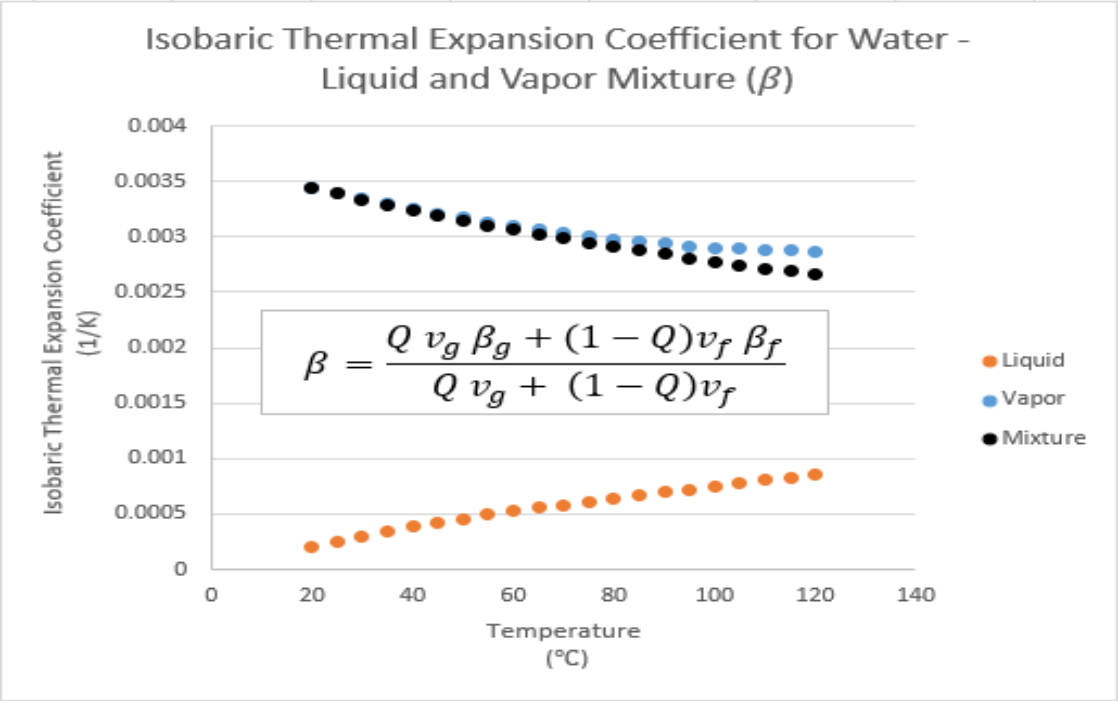

Figure A.3 The mixture isobaric thermal expansion coefficient for water as a function of temperature

Figure A.4 shows the term $\frac{\beta U^2}{c_P}$ as a function of temperature, the term is included in Equation (3.25) as $\left(1+\frac{\beta U^2}{c_P}\right)$. As seen from Figure A.4, $\frac{\beta U^2}{c_P}$ considered negligible due to the small values shown as the temperature increases; therefore, the entire $\left(1+\frac{\beta U^2}{c_P}\right)$ term is approximated as 1.

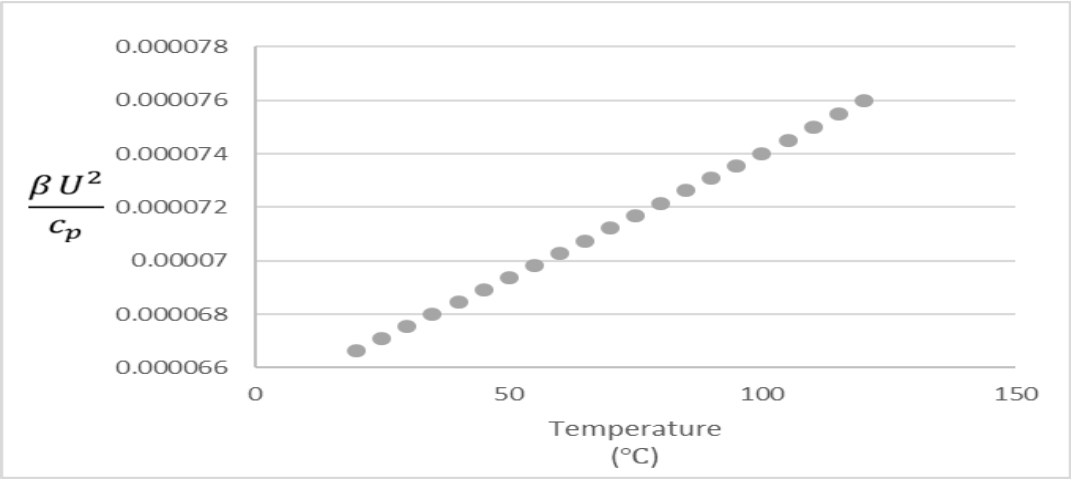

Figure A.4 Given term for water as a function of temperature

Appendix B - Condensation Shock

The condensation shock evaluation was split into two marching solutions as shown in Figure 3.11, a backward marching solution in subcooled region starting from the backpressure and a forward marching solution in the two-phase region after the flash. Figure B.1 is an expansion of Figure 3.11 focusing on the condensation shock evaluation showing the two marching solution lines.

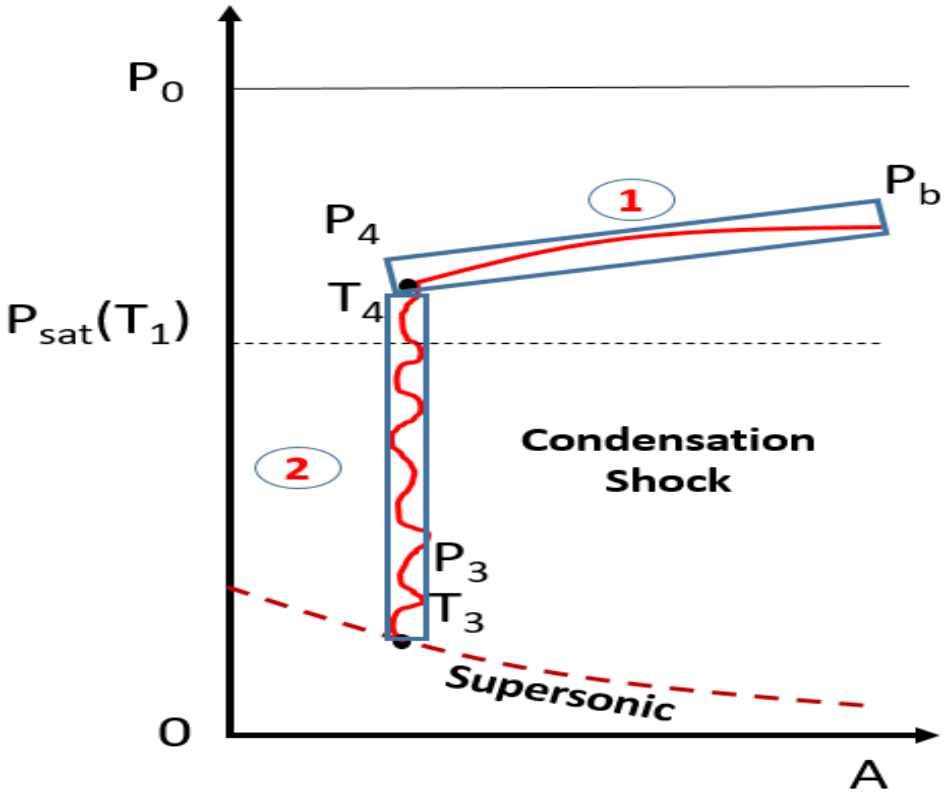

Figure B.1 Condensation shock evaluation in terms of pressure and area

Figure B.2 shows example results from applying the backward marching solution using the derived Equation (3.42). The red line corresponds to different values of pressures at state 4 with a backpressure of 47 kPa and the dashed black line corresponds to the saturation pressure of 70 ℃. Figure B.3 shows example results from applying the forward marching solution using the derived Equation (3.46). The black line corresponds to different values of pressures at state 4 using the calculated values from state 3.

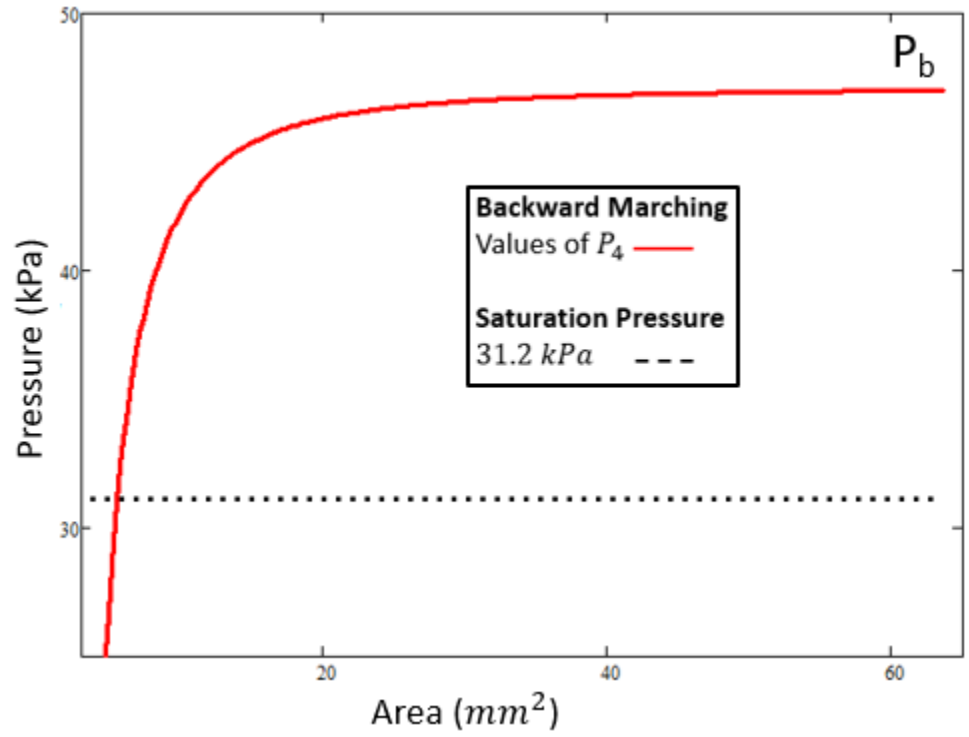

Figure B.2 Results of the backward marching solution for a backpressure of 47 kPa

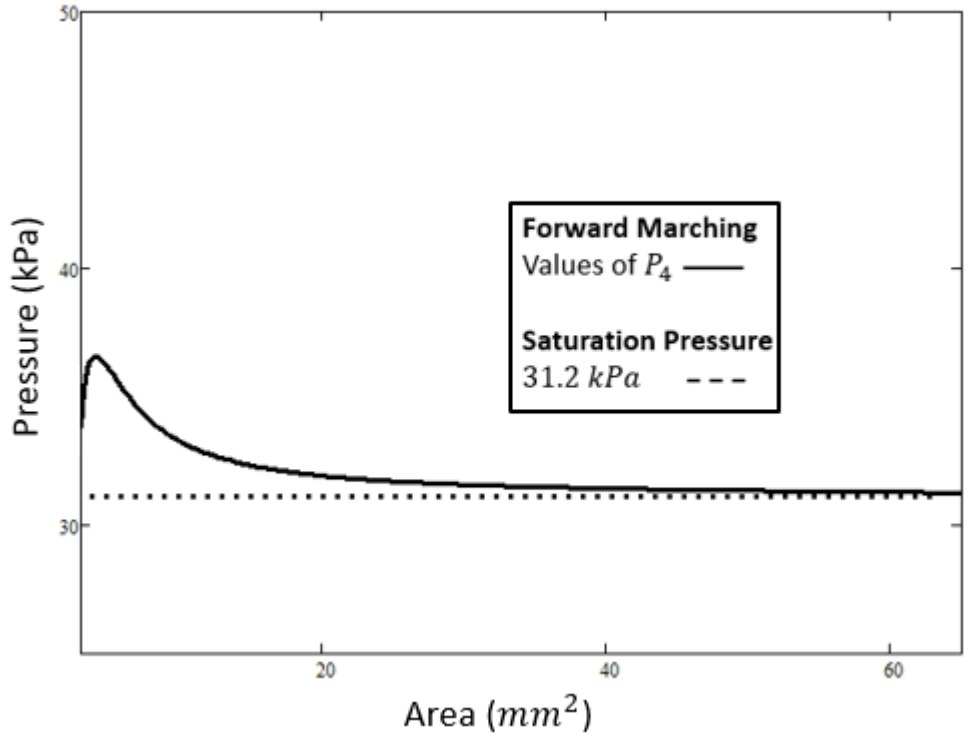

Figure B.3 Results of the forward marching solution for a temperature of 70 ℃

Finally, Figure B.4 shows the results of combining the backward and forward marching procedures. The intersection of these two curves provides a value of the pressure and cross-sectional area corresponding to the condensation shock location, as shown in Figure B.5

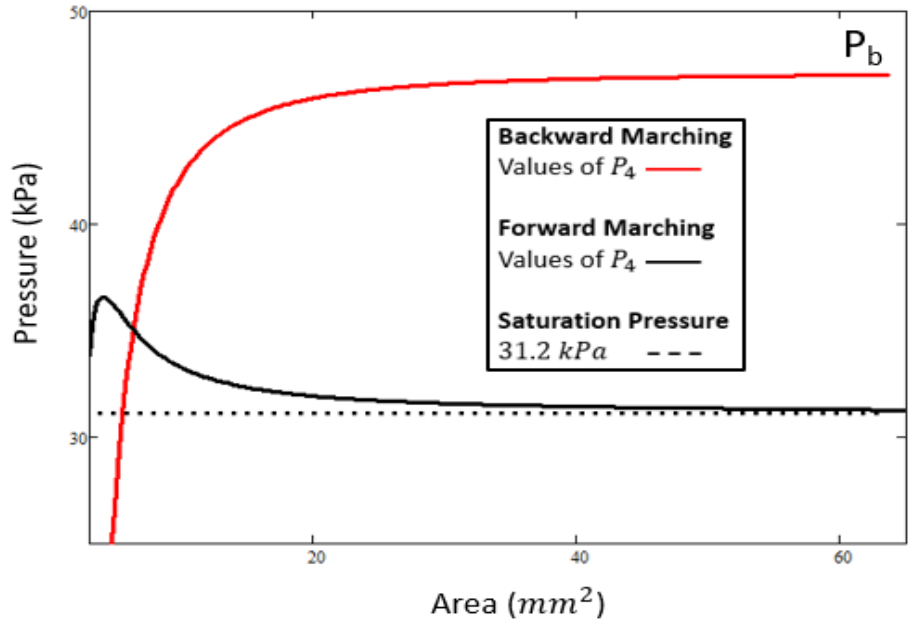

Figure B.4 The condensation shock location for water at backpressure of 47 kPa

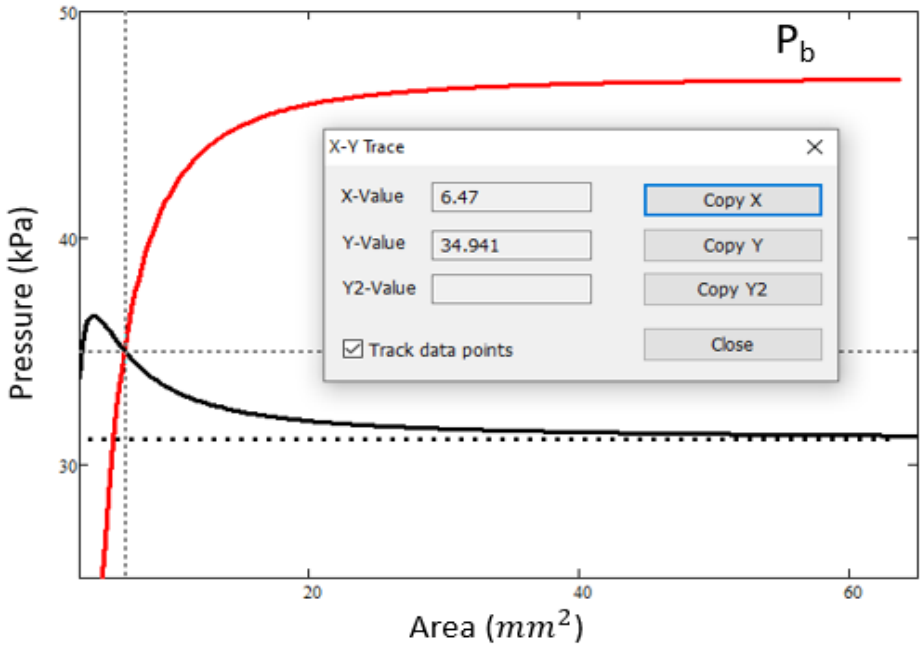

Figure B.5 The intersection values of pressure and area at state 4

Appendix C - Superheat Data Estimation

The experimental superheats are in terms of the pressure undershoot as a function of the depressurization rate. The pressure undershoot is defined as the difference between the saturation pressure and the local pressure at a given tap, $P_{sat} - P$. The estimation of the depressurization rate, $\frac{dP}{dt}$, in the converging section up to near the throat can be found using Equation (3.6). At the throat, the estimation of the depressurization rate is calculated from Equations (3.7) and (3.8) using the forward difference method of numerical differentiation approximation given by Equation (3.10). The equations are copied and showed below. Example calculations of the experimental superheats used in the analysis for Brown's [28], Gallman's [24], and Ahmed's [23] data are given below.

$$\sum' = \frac{dP}{dt} = \frac{\dot{m}^3}{\rho_f^2 A^4}\frac{dA}{dz} \tag{3.6}$$

At the throat,

$$\sum' = \frac{dP}{dt} = \frac{dP}{dz}\frac{dz}{dt} \tag{3.7}$$

where,

$$\frac{dz}{dt} = \frac{\dot{m}}{\rho_f A} \tag{3.8}$$

where $\frac{dP}{dz}$ forward difference method numerical differentiation approximation

$$\frac{dP}{dz} = \frac{P_{z+\Delta z} - P_z}{\Delta z} \tag{3.10}$$

C.1 Brown's Data

The pressure distribution for Brown's data shown in Figure 1.7 which was used to calculate the depressurization rate and the pressure undershoot.

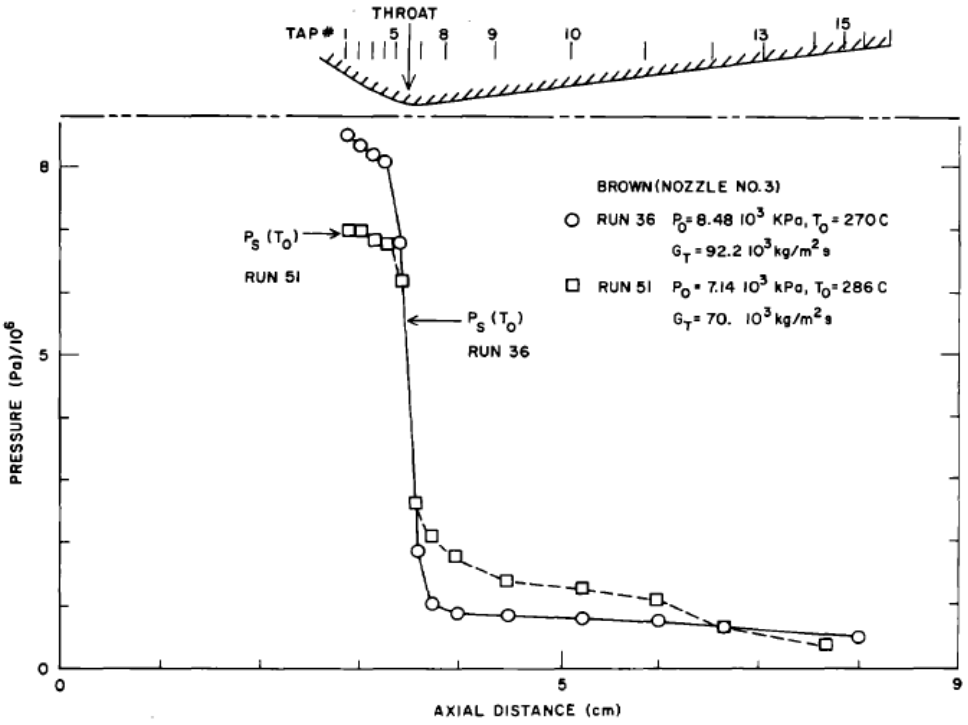

Figure C.1 Pressure distributions for two experiments (Run 36, 51) under 18.3 and50C subcooled inlet conditions [28]

Equation (3.6) was used to calculate the depressurization rate for Brown's data (Run 36) for the pressure taps 3, 4, and 5. Equations (3.7), (3.8) were used to calculate the depressurization rate for tap 6 (throat). Equation (3.10) is applied between taps 6 and 7 as an approximation to calculate $\frac{dP}{dt}$. Table C-1 shows the inlet conditions for (Run 36) as well as the parameters given for taps 3, 4, 5, 6, and 7 that will be used in the estimation. The given distance z is the distance from the inlet of the nozzle.

Table C-1. Inlet conditions for Run 36 [28]

Inlet Conditions		Tap	z(mm)	D(mm)	$A_z(mm^2)$	P(MPa)
T	270 ℃	3	32.5	8.69	59.3	8.03
P_{sat}	5.5 MPa	4	33.8	6.73	35.6	8.01
ρ	767.46 kg/m^3	5	35.1	4.75	17.7	6.76
$\dot{m}$	1.14 kg/s	6(throat)	36.3	3.96	12.3	1.74
		7	37.6	4.49	15.9	0.95

Calculating $\frac{dP}{dt}$ for pressure tap 3, 4, and 5 is shown below using Equation (3.6), where $\frac{dA}{dz}$ is calculated numerically in Mathcad from a 3rd order polynomial of the geometry of the nozzle given by Brown [28].

$$\frac{dP}{dt} = \frac{\left(1.14\,\frac{kg}{s}\right)^3}{\left(767.46\frac{kg}{m^3}\right)^2 (59.3\ mm^2)^4}\ (22.6\ mm) = 4.7x\ 10^9\ \frac{Pa}{s} \qquad \text{(Tap 3)}$$

$$\frac{dP}{dt} = \frac{\left(1.14\,\frac{kg}{s}\right)^3}{\left(767.46\frac{kg}{m^3}\right)^2 (35.6\ mm^2)^4}\ (14.7\ mm) = 2.3x\ 10^{10}\ \frac{Pa}{s} \qquad \text{(Tap 4)}$$

$$\frac{dP}{dt} = \frac{\left(1.14\,\frac{kg}{s}\right)^3}{\left(767.46\frac{kg}{m^3}\right)^2 (17.7\ mm^2)^4}\ (7.38\ mm) = 2.3\ x\ 10^{11}\,\frac{Pa}{s} \qquad \text{(Tap 5)}$$

Calculating $\frac{dP}{dt}$ for pressure tap 6 (throat) using forward difference method given by Equation (3.10) between tap 6 and 7, yields

$$\frac{dP}{dt} = \frac{(0.95 - 1.74)MPa}{(-1.27)mm}\,\frac{\left(1.14\,\frac{kg}{s}\right)}{\left(767.46\frac{kg}{m^3}\right)(12.3\ mm^2)} = 7.6\ x\ 10^{10}\,\frac{Pa}{s} \qquad \text{(Tap 6)}$$

Finally, the pressure undershoot is be calculated for each tap using the values from Table C-1 and the definition $P_{sat} - P$ as shown below. Figure C.2 shows the superheat data in blue for Brown's (Run 36) data.

$$P_{sat} - P = (5.5 - 8.03)MPa = -25.3\ x\ 10^5\ Pa \quad \text{(Tap 3)}$$

$$P_{sat} - P = (5.5 - 8.01)MPa = -25.1\ x\ 10^5\ Pa \quad \text{(Tap 4)}$$

$$P_{sat} - P = (5.5 - 6.76)MPa = 12.6\ x\ 10^5\ Pa \quad \text{(Tap 5)}$$

$$P_{sat} - P = (5.5 - 1.74)MPa = 37.6\ x\ 10^5\ Pa \quad \text{(Tap 6)}$$

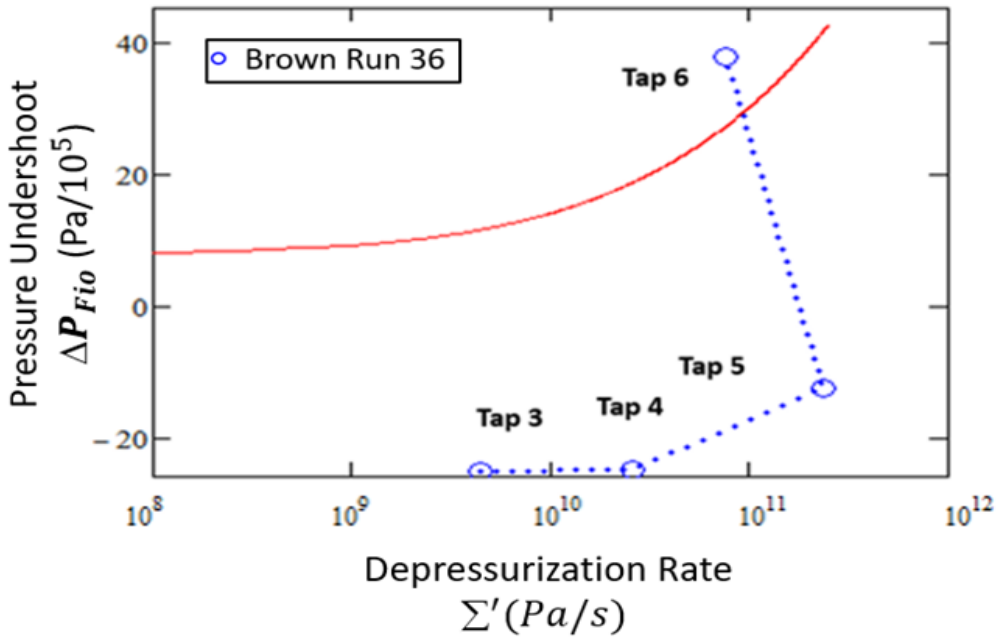

Figure C.2 Reproduction of the flash inception results [27] for (Run 36) with inlet temperature of 270℃ [28]

C.2 Ahmed's Data

The pressure distribution for Ahmed's data shown in Figure C.3 was used to calculate the depressurization rate and the pressure undershoot.

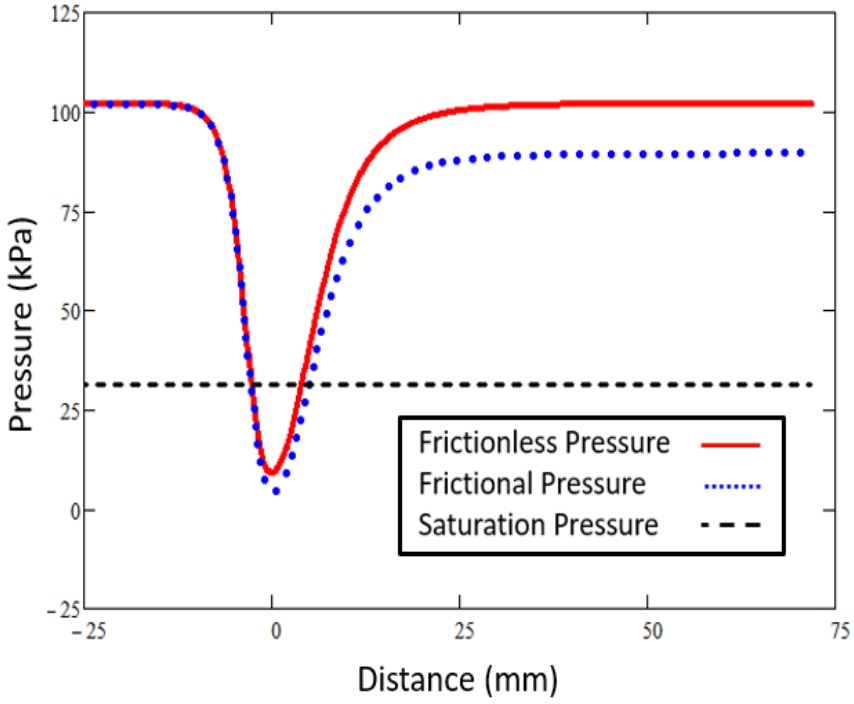

Figure C.3 Pressure distribution for water flowing through converging-diverging nozzle at 70 ℃

Equation (3.6) was used to calculate the depressurization rate for Ahmed's data for the pressure taps 2 and 3. Equations (3.7), (3.8) were used to calculate the depressurization rate for tap 4 (throat). Equation (3.10) is applied between taps 4 and 5 as an approximation to calculate $\frac{dP}{dt}$. Table C-2 shows the test conditions for Ahmed's data.

Table C-2. Test conditions for test 1 [23]

Inlet Conditions		Tap	z(mm)	D(mm)	$A_z(mm^2)$	P(kPa)
T	70 ℃	2	-8	3.43	9.22	96.3
P_{sat}	31.2 kPa	3	-4	2.04	3.27	55.6
ρ	977.6 kg/m^3	4 (throat)	0	1.71	2.31	4.47
$\dot{m}$	0.0305 kg/s	5	5	1.91	2.82	30.8

where z is the distance from the throat, where the throat position has a value of zero as is shown in Figure 3.3. Calculating $\frac{dP}{dt}$ for pressure taps 2 and 3using Equations (3.6) is shown below, where $\frac{dA}{dz}$ is calculated numerical differentiation in Mathcad from a 5th order polynomial of the geometry of the nozzle shown in Figure 3.3.

$$\frac{dP}{dt} = \frac{\left(0.0305\,\frac{kg}{s}\right)^3}{\left(977.6\frac{kg}{m^3}\right)^2 (9.22\,mm^2)^4}\,(2.57\,mm) = 1.1\,x\,10^7\,\frac{Pa}{s} \qquad \text{(Tap 2)}$$

$$\frac{dP}{dt} = \frac{\left(0.0305\,\frac{kg}{s}\right)^3}{\left(977.6\frac{kg}{m^3}\right)^2 (3.27\,mm^2)^4}\,(0.81\,mm) = 1.7\,x\,10^8\,\frac{Pa}{s} \qquad \text{(Tap 3)}$$

Calculating $\frac{dP}{dt}$ for pressure tap 4 (throat) using the forward difference method given by Equation (3.10) between tap 4 and 5, yields

$$\frac{dP}{dt} = \frac{(30.8 - 4.47)kPa}{(5)mm}\,\frac{\left(0.0305\,\frac{kg}{s}\right)}{\left(977.6\frac{kg}{m^3}\right)(2.31\,mm^2)} = 7.3\,x\,10^7\,\frac{Pa}{s} \qquad \text{(Tap 4)}$$

Finally, the pressure undershoot is calculated for each tap using the values from Table C-2 and the equations $P_{sat} - P$ as shown below. Figure C.4 shows the superheat data in blue for Ahmed's test 1 data.

$$P_{sat} - P = (31.2 - 96.3)kPa = -65.1\ kPa \quad \text{(Tap 2)}$$

$$P_{sat} - P = (31.2 - 55.6)kPa = -24.4\ kPa \quad \text{(Tap 3)}$$

$$P_{sat} - P = (31.2 - 4.47)kPa = 26.7\ kPa \quad \text{(Tap 4)}$$

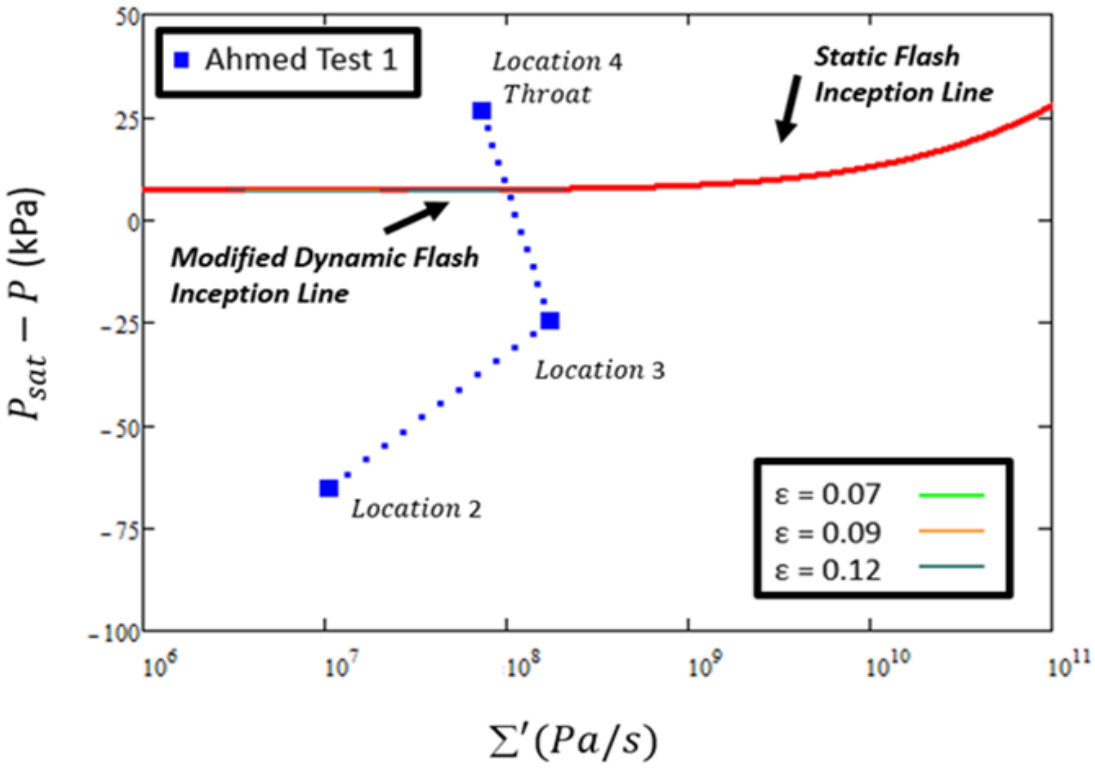

Figure C.4 Flash onset prediction using the modified dynamic flash inception line for 70 ℃ [23]

C.3 Gallman's Data

The pressure distribution for Gallman's data [24] shown in Figure 1.7 was used to calculate the depressurization rate and the pressure undershoot.

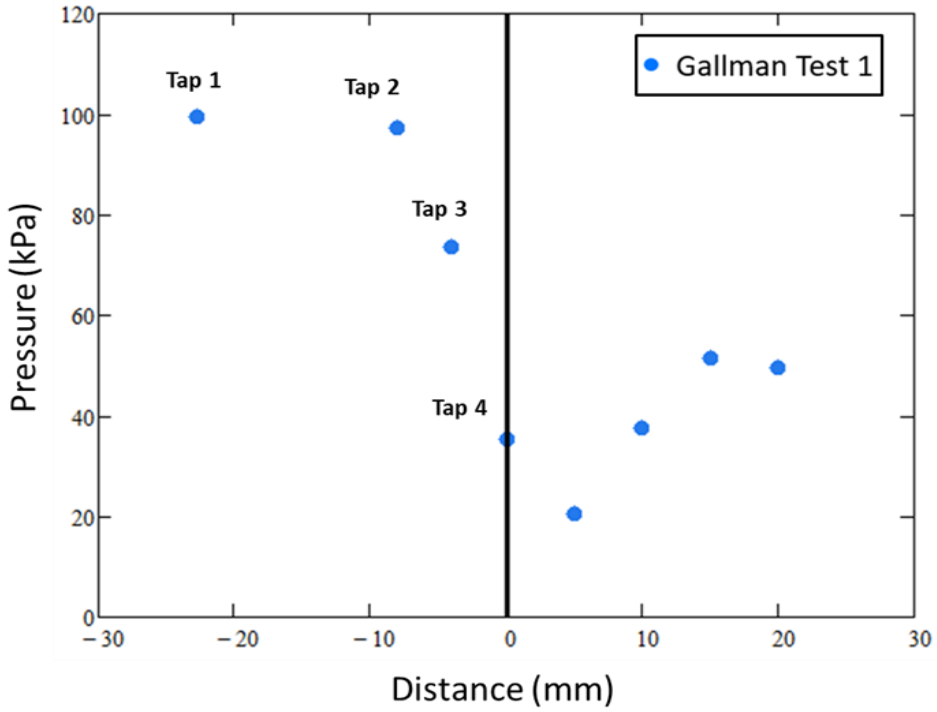

Figure C.5 Pressure distribution as a function of distance in nozzle for a backpressure of 43.2 kPa [24]

Equations (3.6) are used to calculate the depressurization rate for Gallman's data [24] from the measurements at pressure taps 2 and 3. Equations (3.7), (3.8) were used to calculate the depressurization rate for tap 4 (throat). Equation (3.10) is applied between taps 4 and 5 as an approximation to calculate $\frac{dP}{dt}$. Table C-3 shows the inlet conditions for Gallman's test 1.

Table C-3. Inlet conditions for Test 1 [24]

Inlet Conditions		Tap	z(mm)	D(mm)	$A_z(mm^2)$	P(kPa)
T	20 ℃	2	-8	3.43	9.22	97.4
P_{sat}	2.34 kPa	3	-4	2.04	3.27	73.6
ρ	998.2 kg/m^3	4 (throat)	0	1.71	2.31	35.3
$\dot{m}$	0.0248 kg/s	5	5	1.91	2.82	20.4

where z is the distance from the throat, where the throat position has a value of zero as is shown in Figure 3.3. Calculating $\frac{dP}{dt}$ for pressure taps 2 and 3 using Equations (3.6) shown below, where $\frac{dA}{dz}$ is calculated numerically in Mathcad from a 5th order polynomial of the geometry of the nozzle shown in Figure 3.3.

$$\frac{dP}{dt} = \frac{\left(0.0248\,\frac{kg}{s}\right)^3}{\left(998.2\frac{kg}{m^3}\right)^2 (9.22\ mm^2)^4}\ (2.57\ mm) = 5.4\ x\ 10^6\ \frac{Pa}{s} \qquad \text{(Tap 2)}$$

$$\frac{dP}{dt} = \frac{\left(0.0248\,\frac{kg}{s}\right)^3}{\left(998.2\frac{kg}{m^3}\right)^2 (3.27\ mm^2)^4}\ (0.81\ mm) = 7.3\ x\ 10^7\ \ \frac{Pa}{s} \qquad \text{(Tap 3)}$$

Calculating $\frac{dP}{dt}$ for pressure tap 4 (throat) using a forward difference method given by Equation (3.10) between tap 4 and 5, yields

$$\frac{dP}{dt} = \frac{(20.4 - 35.3)kPa}{(5)mm}\,\frac{\left(0.0248\,\frac{kg}{s}\right)}{\left(998.2\frac{kg}{m^3}\right)(2.31\ mm^2)} = 3.3\ x\ 10^7\ \ \frac{Pa}{s} \qquad \text{(Tap 4)}$$

Finally, the pressure undershoot is calculated for each tap using the values from Table C-2 and the definition $P_{sat} - P$ as shown below. Figure C.6 shows the superheat data in blue for Gallman's test 1 data.

$$P_{sat} - P = (2.34 - 97.4)kPa = -95.1\ kPa \quad \text{(Tap 2)}$$

$$P_{sat} - P = (2.34 - 73.6)kPa = -71.2\ kPa \quad \text{(Tap 3)}$$

$$P_{sat} - P = (2.34 - 35.3)kPa = -35.3\ kPa \quad \text{(Tap 4)}$$

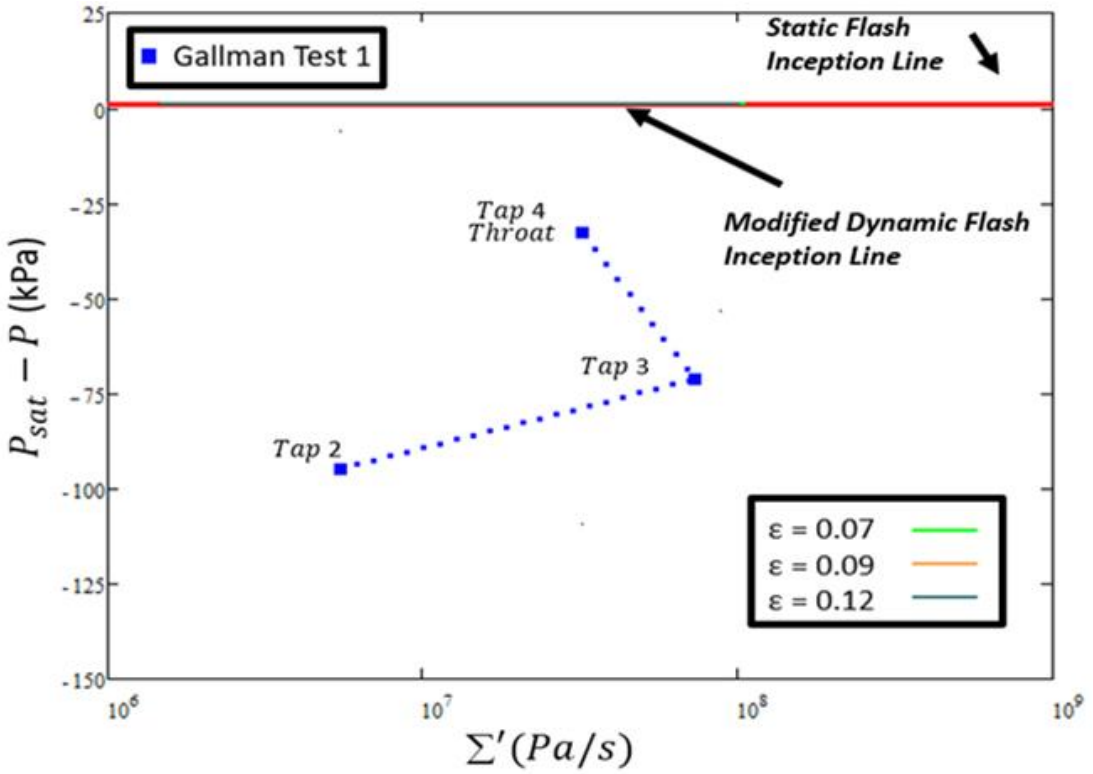

Figure C.6 Flash onset prediction for a backpressure of 43.2 kPa [24] the modified dynamic flash inception line

Appendix D - Gallman's Experimental Flow Visualization [24]

Gallman [24] extended the work that was done by Ahmed in an attempt to enable pressure measurements and visualize the flash in steady state two-phase flow experiments using water with an inlet temperature of 20℃. A clear 3D transparent plastic printed nozzle was used in experiments that matched the same geometry as the nozzle used by Ahmed [23], as given in Figure 3.3. Eight pressure taps were placed in the 3D nozzle, which were made by drilling holes through to the inner surface. Figure D.1 show a close-up image of the pressure taps locations. A high-speed camera was used to visualize the two-phase flow condition and the flash behavior.

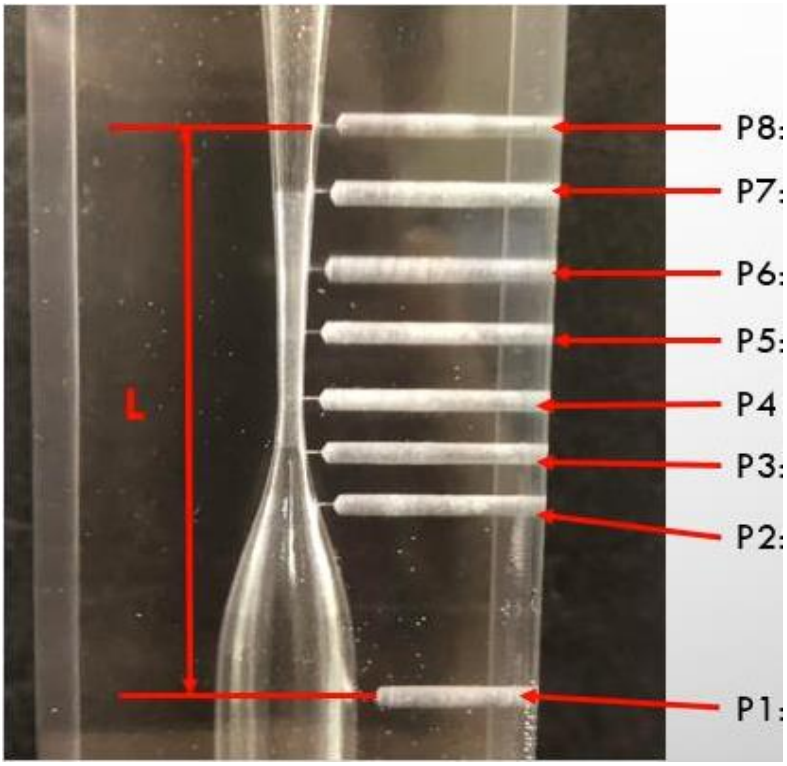

Figure D.1 Pressure taps location for the 3D plastic nozzle [24]

Figure D.2 show the visualization of the result of flash initiation and cavitation onset for flow in the plastic nozzle with a backpressure of 43.2 kPa. As seen from the figure, the flash initiated close to the pressure tap (tap 4) at the throat along one side of the nozzle. Results strongly suggest that the bore hole of the pressure tap likely had a small burr on the inside surface, which acted as a nucleation site and develop pre-mature flash inception. The white dashed lines show the length of two-phase region in the nozzle.

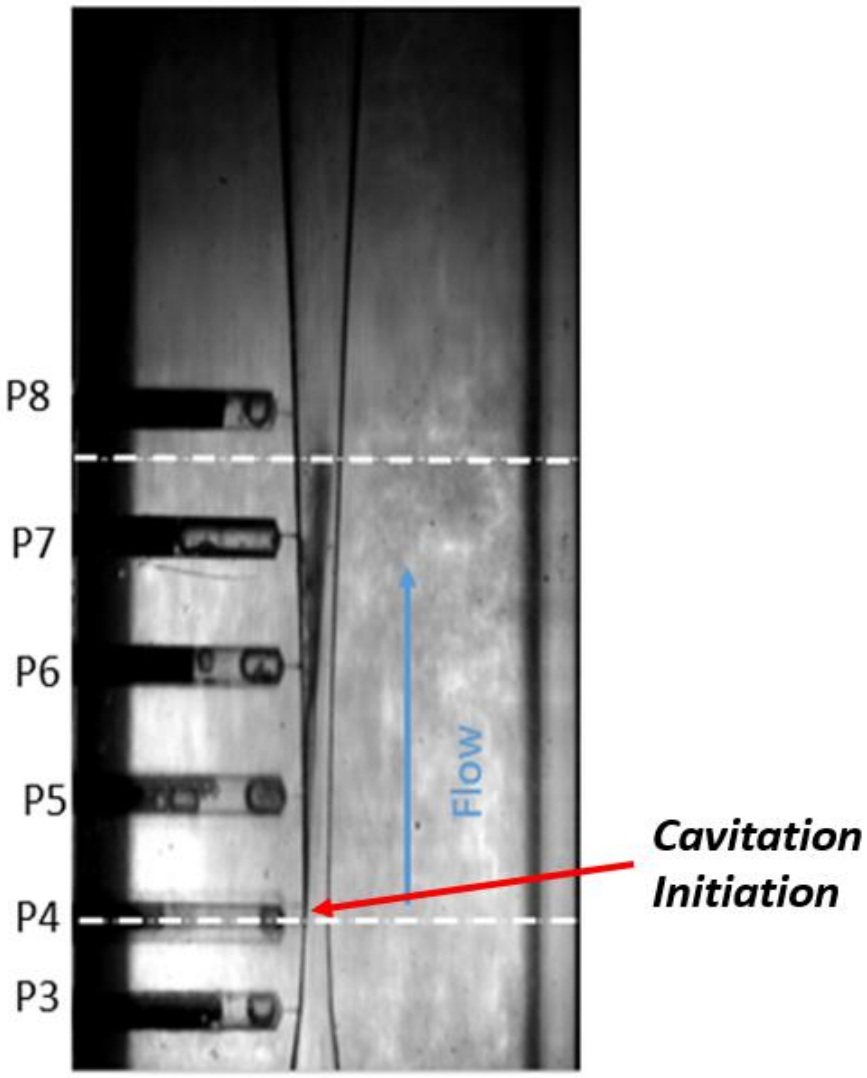

Figure D.2 Image of two-phase flow for a backpressure of 43.2 kPa [24]

Appendix E - Flash Inception (Evaporation Wave)

Analysis of the cavitation "flash" point is presented by investigating the Rayleigh and Rankine-Hugoniot equations [38] for homogeneous flow through a converging-diverging nozzle. Simoes [38] introduced a flash inception analysis for a 1-D evaporation wave in convergent nozzles. The analysis was presented based on experimental work for short nozzles. An isentropic convergent nozzle with uniform metastable liquid state is assumed where a 1-D evaporation wave occurs at some point downstream. Just downstream of the evaporation wave (flash), a two-phase flow can be predicted using the Rayleigh and Rankine-Hugoniot equations, which are developed below. Section 3.3 the flash cavitation wave is used to evaluate the downstream state (subsonic or supersonic) as shown in Figure 3.9. Using a marching algorithm and a differential analysis on the control volume shown in Figure 3.10, the downstream state was calculated. The downstream state can also be found using the Rayleigh and Rankine-Hugoniot equations and will be introduced in this appendix. For the same control volume shown in Figure 3.10, the conservation of mass equation can be introduced assuming steady state and one dimensional from state 1 to state 2 by

$$\dot{m}_2 = \dot{m}_1 \tag{E.1}$$

or

$$(\rho UA)_2 = (\rho UA)_1 \tag{E.2}$$

Where state 1 is the metastable liquid state upstream and state 2 is the downstream state which will be either supersonic or subsonic. Introducing J as the superficial mass flux in the following form

$$J = \frac{\dot{m}}{A} \tag{E.3}$$

Substituting Equation (E.2) into (E.3) yields the final form of the conversation of mass equation

$$[J] = \frac{U_2 - U_1}{v_2 - v_1} = \frac{[U]}{[v]} \tag{E.4}$$

where U is the velocity, and v is the specific volume and the brackets in the equation represents the difference between state 2 and state 1.

Assuming one-dimensional, uniform velocity, steady flow, constant area, and ignoring gravitational forces, frictional forces, and shear forces, the conversation of momentum can be reduced to

$$P_1 A - P_2 A = \dot{m}\,(U_2 - U_1) \tag{E.5}$$

Dividing by the area A and substituting Equation (E.4) into (E.5) yields

$$P_1 - P_2 = J\,(U_2 - U_1) \tag{E.6}$$

Rearranging Equation (E.6) in terms of the bracket difference, yields the final form of the conversation of momentum equation

$$[P + J\,U] = 0 \tag{E.7}$$

For a steady flow with uniform velocities, and the assumption that the system has adiabatic walls, no gravitational effects, and that there is no work (by friction), the conversation of energy can be reduced to

$$\left(h_2 + \frac{1}{2}U_2^2\right) = \left(h_1 + \frac{1}{2}U_1^2\right) \tag{E.8}$$

where h is the specific enthalpy. In terms of the bracket differences, Equation (E.8) yields the final form of the conversation of energy equation as follows

$$\left[h + \frac{\mathrm{U}^2}{2}\right] = 0 \tag{E.9}$$

Combining the conservation of mass, Equation (E.4), and the conservation of momentum, Equation (E.7), yields the so-called Rayleigh equation [38] in the form

$$J^2 = -\frac{[P]}{[v]} \tag{E.10}$$

where P is the pressure and v is the specific volume. The term $[P] = P_2 - P_1$ and $[v] = v_2 - v_1$. Combining the conservation of mass, Equation (E.4), the conservation of momentum, Equation (E.7), and the conservation of energy, Equation (E.9), yields the so-called Rankine-Hugoniot equation [38] in the form

$$[h] = -\frac{v_1 + v_2}{2}[P] \tag{E.11}$$

Simoes [38] introduced the analysis of the Rayleigh and Rankine-Hugoniot equations in a graphical form. Figure E.1 shows a liquid-vapor saturation region for a simple fluid plotted in terms of pressure and specific volume. State 1 refers to the given upstream initial metastable state and state 2 is the downstream solution found from the intersection between the lines that represents the two equations, points A, B, or C. The intersection between the equations usually occur with two points, as shown Figure (E.1), where point A represents a subsonic solution and point B represents a supersonic solution.

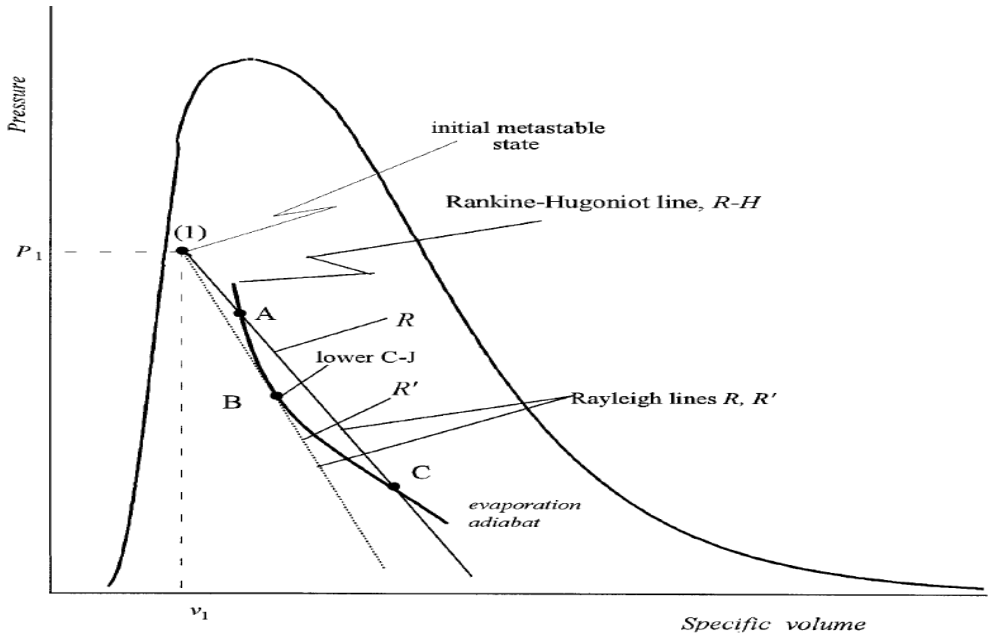

Figure E.1 Graphical solution of the flash inception analysis [38]

The Rayleigh and Rankine-Hugoniot Equations, (E.10) and (E.11), respectfully, are used below to illustrate the prediction of the downstream subsonic and supersonic points for R134a flowing through a converging-diverging nozzle with an inlet temperature of 35 ℃. The nozzle has a 1.5 mm throat diameter and the mass flow rate is 12 $\frac{g}{s}$. Figure E.2 shows the results of the graphical solution of the flash inception for R134a through a converging-diverging nozzle. It is observed that, for the given set of conditions, the Rayleigh and Rankine-Hugoniot lines intersects in two locations, points A and B, referring to the subsonic and supersonic conditions downstream of the flash.

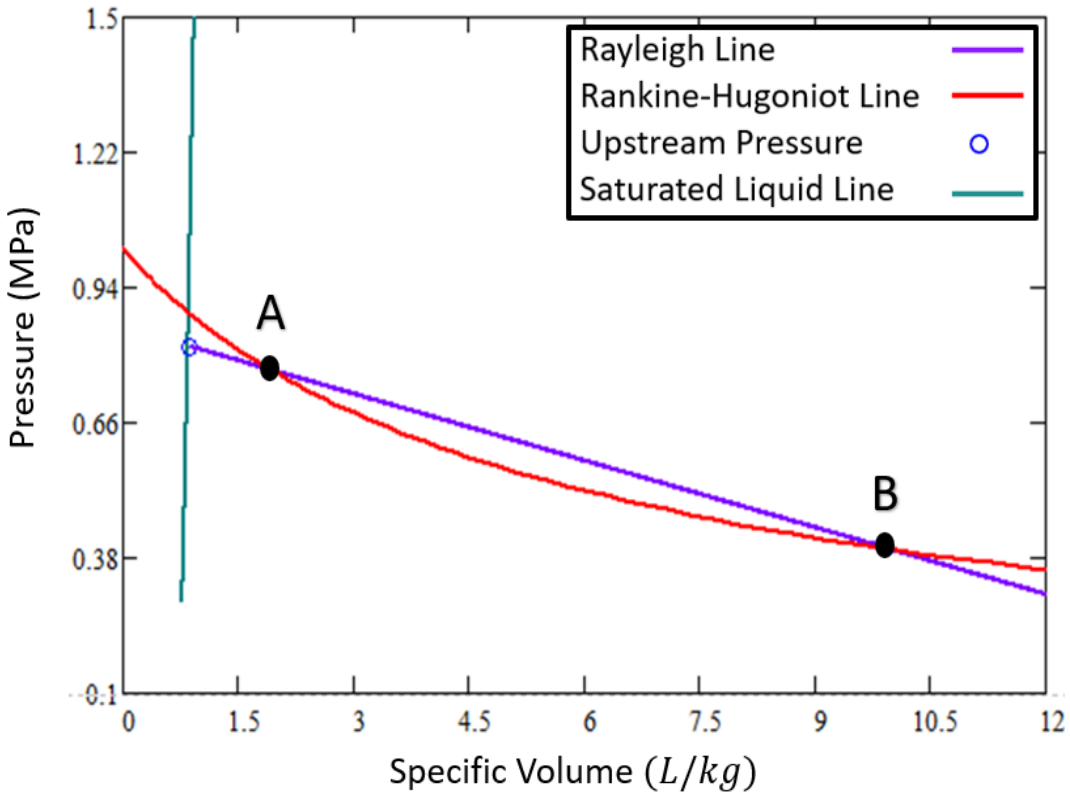

Figure E.2 A flash inception analysis for R134a with an inlet temperature of 35 ℃

The Rayleigh and Rankine-Hugoniot equations are now used in an attempt to predict the downstream subsonic and supersonic points for Ahmed's experimental water [23], flowing through the converging-diverging nozzle for an inlet temperature of 70 ℃. The nozzle has a 1.7 mm throat diameter and the mass flow rate is 30.6 $\frac{g}{s}$. Figure E.2 shows the results of the graphical solution of the flash inception for water with an inlet temperature of 70 ℃. It's observed that the Rayleigh and Rankine-Hugoniot lines do not intersect, and a solution failed to occur for the given flow conditions. It is currently not understood why a solution does not appear to exist for the water flow experiments but does exist for the R134a analysis. Perhaps it could be in some way related to the tiny temperature changes expected and observed in the water experiments. These small changes make the expressions used to represent the metastable fluid properties much more critical.

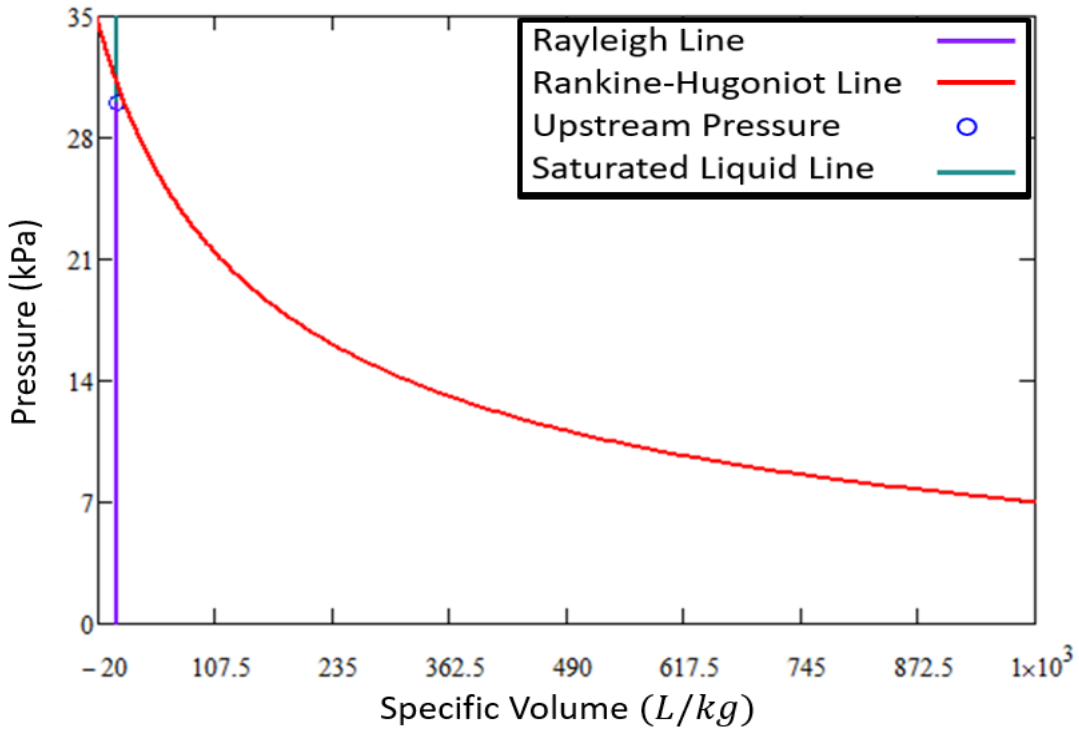

Figure E.3 A flash inception analysis for Water with an inlet temperature of 70 ℃

Refinement of the above analysis should be the subject for future studies into the application of the Rayleigh and Rankine-Hugoniot equations for different flow conditions in converging-diverging nozzles with different fluids.

Appendix F - Mathcad Codes

F.1 Water Saturation Values Calculations

Mathcad code for saturation values was developed by Dr. Beck and then was extended to include other properties

Linear Interpolation Algorithm for H2O Saturation Properties

ORIGIN := 1 TOL := 0.0000001 kJ := 1000·J μPa := 10^{-6}·Pa CTOL5 := 0.0000001

Input Matrix of Water Saturation Properties, T(C), p(MPa), ρ_f(kg/m^3), ρ_g(kg/m^3), h_f(kJ/kgK), h_g(kJ/kgK), s_f(kJ/kgK), s_g(kJ/kgK), C_{pf}(kJ/kgK), C_{pg}(kJ/kgK):

T(C) p_{sat}(MPa) ρ_f(kg/m^3) $\rho_g$kg/m^3) h_f(kJ/kg)

RP1 :=

	1	2	3	4	5
1	1	$6.571\cdot10^{-4}$	999.85	$5.196\cdot10^{-3}$	4.177
2	2	$7.06\cdot10^{-4}$	999.89	$5.563\cdot10^{-3}$	8.392
3	3	$7.581\cdot10^{-4}$	999.92	$5.952\cdot10^{-3}$	12.604
4	4	$8.136\cdot10^{-4}$	999.93	$6.365\cdot10^{-3}$	16.813
5	5	$8.726\cdot10^{-4}$	999.92	$6.802\cdot10^{-3}$	21.02
6	6	$9.354\cdot10^{-4}$	999.89	$7.266\cdot10^{-3}$	25.224
7	7	$1.002\cdot10^{-3}$	999.86	$7.757\cdot10^{-3}$	...

h_g(kJ/kg) s_f(kJ/kgK) s_g(kJ/kgK) C_{pf}(kJ/kgK)

RP2 :=

	1	2	3	4
1	$2.503\cdot10^3$	0.015	9.129	4.217
2	$2.505\cdot10^3$	0.031	9.103	4.213
3	$2.506\cdot10^3$	0.046	9.076	4.211
4	$2.508\cdot10^3$	0.061	9.05	4.208
5	$2.51\cdot10^3$	0.076	9.025	4.205
6	$2.512\cdot10^3$	0.091	8.999	4.203
7	$2.514\cdot10^3$	0.106	8.974	4.201
8	$2.516\cdot10^3$	0.121	8.949	...

a_f (m/s) a_g (m/s) μ_f (μPa-s) μ_g (μPa-s)

RP3 :=

	1	2	3	4
1	$1.407 \cdot 10^3$	409.72	$1.731 \cdot 10^3$	9.239
2	$1.412 \cdot 10^3$	410.44	$1.674 \cdot 10^3$	9.263
3	$1.417 \cdot 10^3$	411.16	$1.619 \cdot 10^3$	9.287
4	$1.421 \cdot 10^3$	411.88	$1.567 \cdot 10^3$	...

Extract Individual Properties from above Input Matrices, RP1 & RP2:

$\Delta T := 1 \Delta°C$ $i := 1..373$

T(C) p_{sat}(MPa) ρ_f(kg/m^3) $\rho_g$kg/m^3) h_f(kJ/kg)

$TT_i := RP1_{i,1} \cdot \Delta°C$ $PP_i := RP1_{i,2} \cdot MPa$ $\rho\rho f_i := RP1_{i,3} \cdot \frac{kg}{m^3}$ $\rho\rho g_i := RP1_{i,4} \cdot \frac{kg}{m^3}$ $HHf_i := RP1_{i,5} \cdot \frac{kJ}{kg}$

h_g(kJ/kg) s_f(kJ/kgK) s_g(kJ/kgK) C_{pf}(kJ/kgK) C_{pg}(kJ/kgK)

$HHg_i := RP2_{i,1} \cdot \frac{kJ}{kg}$ $SSf_i := RP2_{i,2} \cdot \frac{kJ}{kg \cdot K}$ $SSg_i := RP2_{i,3} \cdot \frac{kJ}{kg \cdot K}$ $Cpf_i := RP2_{i,4} \cdot \frac{kJ}{kg \cdot K}$ $Cpg_i := RP2_{i,5} \cdot \frac{kJ}{kg \cdot K}$

a_f (m/s) a_g (m/s) μ_f (μPa-s) μ_g (μPa-s)

$AA_{f_i} := RP3_{i,1} \cdot \frac{m}{s}$ $AA_{g_i} := RP3_{i,2} \cdot \frac{m}{s}$ $MM_{f_i} := RP3_{i,3} \cdot \mu Pa \cdot s$ $MM_{g_i} := RP3_{i,4} \cdot \mu Pa \cdot s$

(a) Saturation Pressure, p_{sat}(T):

$$p_{sat}(T) := \left| \begin{array}{l} T \leftarrow \frac{T}{\Delta°C} \\ j \leftarrow \text{floor}\left(\frac{T}{\frac{\Delta T}{\Delta°C}} \right) \\ Press \leftarrow PP_j + \left(\frac{PP_{j+1} - PP_j}{\frac{\Delta T}{\Delta°C}} \right) \cdot \left(T - \frac{TT_j}{\Delta°C} \right) \end{array} \right.$$

$$\text{floor}\left(\frac{30}{\frac{\Delta T}{\Delta°C}} \right) + 1 = 31$$

$p_{sat}(25.5 \cdot \Delta°C) = 3.2669 \times 10^{-3} \cdot MPa$

$p_{sat}(30 \cdot \Delta°C) = 4.2470 \times 10^{-3} \cdot MPa$

$T := 0.0 \cdot \Delta°C, 0.1 \cdot \Delta°C .. 373 \cdot \Delta°C$

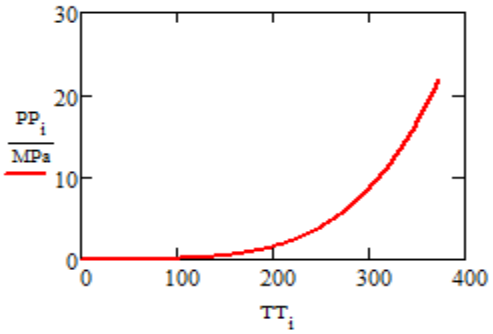

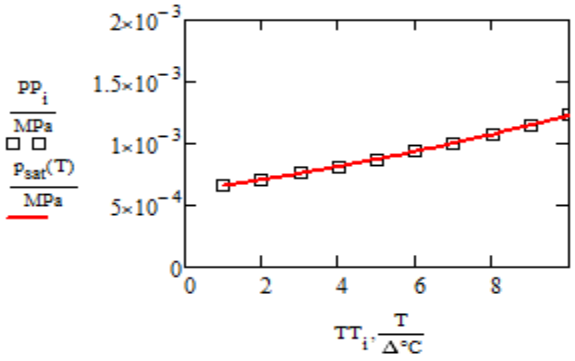

(b) Liquid Density, $\rho_f(T)$:

$$\rho_f(T) := \left| \begin{array}{l} T \leftarrow \frac{T}{\Delta^\circ C} \\ j \leftarrow \text{floor}\left(\frac{T}{\frac{\Delta T}{\Delta^\circ C}}\right) \\ dens_f \leftarrow \rho\rho f_j + \left(\frac{\rho\rho f_{j+1} - \rho\rho f_j}{\frac{\Delta T}{\Delta^\circ C}}\right) \cdot \left(T - \frac{TT_j}{\Delta^\circ C}\right) \end{array} \right.$$

$$\text{floor}\left(\frac{30}{\frac{\Delta T}{\Delta^\circ C}}\right) + 1 = 31$$

(c) Vapor Density, $\rho_g(T)$:

$$\rho_g(T) := \left| \begin{array}{l} T \leftarrow \frac{T}{\Delta^\circ C} \\ j \leftarrow \text{floor}\left(\frac{T}{\frac{\Delta T}{\Delta^\circ C}}\right) \\ dens_g \leftarrow \rho\rho g_j + \left(\frac{\rho\rho g_{j+1} - \rho\rho g_j}{\frac{\Delta T}{\Delta^\circ C}}\right) \cdot \left(T - \frac{TT_j}{\Delta^\circ C}\right) \end{array} \right.$$

$$\rho_g(30 \cdot \Delta^\circ C) = 0.03042 \cdot \frac{kg}{m^3}$$

(d) Liquid Enthalpy $h_f(T)$:

$$h_f(T) := \left| \begin{array}{l} T \leftarrow \frac{T}{\Delta^\circ C} \\ j \leftarrow \text{floor}\left(\frac{T}{\frac{\Delta T}{\Delta^\circ C}}\right) \\ hliq \leftarrow HHf_j + \left(\frac{HHf_{j+1} - HHf_j}{\frac{\Delta T}{\Delta^\circ C}}\right) \cdot \left(T - \frac{TT_j}{\Delta^\circ C}\right) \end{array} \right.$$

$$h_f(30 \cdot \Delta^\circ C) = 125.730 \cdot \frac{kJ}{kg}$$

(e) Vapor Enthalpy $h_g(T)$:

$$h_g(T) := \left| \begin{array}{l} T \leftarrow \frac{T}{\Delta^\circ C} \\ j \leftarrow \text{floor}\left(\frac{T}{\frac{\Delta T}{\Delta^\circ C}}\right) \\ hvap \leftarrow HHg_j + \left(\frac{HHg_{j+1} - HHg_j}{\frac{\Delta T}{\Delta^\circ C}}\right) \cdot \left(T - \frac{TT_j}{\Delta^\circ C}\right) \end{array} \right.$$

$$h_g(30 \cdot \Delta^\circ C) = 2555.5 \cdot \frac{kJ}{kg}$$

(f) Liquid Entropy $s_f(T)$:

$$s_f(T) := \left| \begin{array}{l} T \leftarrow \frac{T}{\Delta^\circ C} \\ j \leftarrow \text{floor}\left(\frac{T}{\frac{\Delta T}{\Delta^\circ C}}\right) \\ sliq \leftarrow SSf_j + \left(\frac{SSf_{j+1} - SSf_j}{\frac{\Delta T}{\Delta^\circ C}}\right) \cdot \left(T - \frac{TT_j}{\Delta^\circ C}\right) \end{array} \right.$$

$$s_f(30 \cdot \Delta^\circ C) = 0.4368 \cdot \frac{kJ}{kg \cdot K}$$

(g) Vapor Entropy $s_g(T)$:

$$s_g(T) := \left| \begin{array}{l} T \leftarrow \frac{T}{\Delta^\circ C} \\ j \leftarrow \text{floor}\left(\frac{T}{\frac{\Delta T}{\Delta^\circ C}}\right) \\ svap \leftarrow SSg_j + \left(\frac{SSg_{j+1} - SSg_j}{\frac{\Delta T}{\Delta^\circ C}}\right) \cdot \left(T - \frac{TT_j}{\Delta^\circ C}\right) \end{array} \right.$$

$$s_g(30 \cdot \Delta^\circ C) = 8.452 \cdot \frac{kJ}{kg \cdot K}$$

(h) Liquid Specific Heat, $C_{pf}(T)$:

$$C_{pf}(T) := \left| \begin{array}{l} T \leftarrow \frac{T}{\Delta^\circ C} \\ j \leftarrow \text{floor}\left(\frac{T}{\frac{\Delta T}{\Delta^\circ C}}\right) \\ Cpliq \leftarrow Cpf_j + \left(\frac{Cpf_{j+1} - Cpf_j}{\frac{\Delta T}{\Delta^\circ C}}\right) \cdot \left(T - \frac{TT_j}{\Delta^\circ C}\right) \end{array} \right.$$

$$C_{pf}(30 \cdot \Delta^\circ C) = 4.1801 \cdot \frac{kJ}{kg \cdot K}$$

(j) Define Vaporization Properties, $h_{fg}(T)$ and $s_{fg}(T)$:

$$h_{fg}(T) := h_g(T) - h_f(T) \qquad h_{fg}(30 \cdot \Delta^\circ C) = 2.4298 \times 10^3 \cdot \frac{kJ}{kg}$$

$$s_{fg}(T) := s_g(T) - s_f(T) \qquad s_{fg}(30 \cdot \Delta^\circ C) = 8.015 \cdot \frac{kJ}{kg \cdot K}$$

(k) Define Specific Volume of Liq and Vap:

$$v_f(T) := \frac{1}{\rho_f(T)} \qquad v_f(30 \cdot \Delta^\circ C) = 1.004 \times 10^{-3} \cdot \frac{m^3}{kg}$$

$$v_g(T) := \frac{1}{\rho_g(T)} \qquad v_g(30 \cdot \Delta^\circ C) = 32.879 \cdot \frac{m^3}{kg}$$

(l) Sound Speed Liquid, a_f (m/s):

$$a_f(T) := \left| \begin{array}{l} T \leftarrow \frac{T}{\Delta^\circ C} \\ j \leftarrow \text{floor}\left(\frac{T}{\frac{\Delta T}{\Delta^\circ C}}\right) \\ A_{liq} \leftarrow AA_{f_j} + \left(\frac{AA_{f_{j+1}} - AA_{f_j}}{\frac{\Delta T}{\Delta^\circ C}}\right) \cdot \left(T - \frac{TT_j}{\Delta^\circ C}\right) \end{array} \right.$$

$$a_f(30 \cdot \Delta^\circ C) = 1509.000 \cdot \frac{m}{s}$$

(m) Sound Speed Vapor a_g (m/s):

$$a_g(T) := \left| \begin{array}{l} T \leftarrow \frac{T}{\Delta^\circ C} \\ j \leftarrow \text{floor}\left(\frac{T}{\frac{\Delta T}{\Delta^\circ C}}\right) \\ A_{vap} \leftarrow AA_{g_j} + \left(\frac{AA_{g_{j+1}} - AA_{g_j}}{\frac{\Delta T}{\Delta^\circ C}}\right) \cdot \left(T - \frac{TT_j}{\Delta^\circ C}\right) \end{array} \right.$$

$$a_g(30 \cdot \Delta^\circ C) = 430.030 \frac{m}{s}$$

(o) Viscosity Vapor μ_g (μPa-s):

$$\mu_g(T) := \left| \begin{array}{l} T \leftarrow \frac{T}{\Delta^\circ C} \\ j \leftarrow \text{floor}\left(\frac{T}{\frac{\Delta T}{\Delta^\circ C}}\right) \\ \mu_{vap} \leftarrow MM_{g_j} + \left(\frac{MM_{g_{j+1}} - MM_{g_j}}{\frac{\Delta T}{\Delta^\circ C}}\right) \cdot \left(T - \frac{TT_j}{\Delta^\circ C}\right) \end{array} \right.$$

$$\mu_g(30 \cdot \Delta^\circ C) = 10.010 \cdot \mu Pa \cdot s$$

(n) Viscosity Liquid, μ_f (μPa-s):

$$\mu_f(T) := \left| \begin{array}{l} T \leftarrow \frac{T}{\Delta^\circ C} \\ j \leftarrow \text{floor}\left(\frac{T}{\frac{\Delta T}{\Delta^\circ C}}\right) \\ \mu_{liq} \leftarrow MM_{f_j} + \left(\frac{MM_{f_{j+1}} - MM_{f_j}}{\frac{\Delta T}{\Delta^\circ C}}\right) \cdot \left(T - \frac{TT_j}{\Delta^\circ C}\right) \end{array} \right.$$

$$\mu_f(30 \cdot \Delta^\circ C) = 797.360 \cdot \mu Pa \cdot s$$

(P) Surface Tension σ (N/m):

$$\sigma(T) := \left| \begin{array}{l} T \leftarrow \frac{T}{\Delta^\circ C} \\ j \leftarrow \text{floor}\left(\frac{T}{\frac{\Delta T}{\Delta^\circ C}}\right) \\ \mu_{vap} \leftarrow ST_j + \left(\frac{ST_{j+1} - ST_j}{\frac{\Delta T}{\Delta^\circ C}}\right) \cdot \left(T - \frac{TT_j}{\Delta^\circ C}\right) \end{array} \right.$$

$$\sigma(1 \cdot \Delta^\circ C) = 0.076 \frac{kg}{s^2}$$

F.2 Single-Phase Pressure Distribution

Single-phase pressure drop with and without friction

$T_1 := 70 \cdot \Delta°C$ $D_z(\xi) := 2 \cdot r_n(\xi) \cdot mm$ $m_1 := 0.0306 \cdot \frac{kg}{s}$ $A_z(\xi) := \pi \frac{\left[(D_z(\xi))^2\right]}{4}$

$\xi_i := -27.88$ $G_z(\xi) := \frac{m_1}{A_z(\xi)}$ $G_i(\xi_i) := \frac{m_1}{A_z(\xi_i)}$ $P_i := 102 kPa$

$V_z(\xi, T_1) := \frac{m_1}{A_z(\xi) \cdot \rho_f(T_1)}$ $Re_z(\xi, T_1) := \frac{\rho_f(T_1) \cdot V_z(\xi, T_1) \cdot D_z(\xi)}{\mu_f(T_1)}$

$f(\xi, T_1) := \frac{0.3164}{Re_z(\xi, T_1)^{0.25}}$ $\Delta P_f(\xi, T_1) := \int_{-27.88}^{\xi} \frac{1}{2}\left(\frac{f(\xi, T_1)}{2 \cdot r_n(\xi)}\right) \cdot \left(\rho_f(T_1) \cdot V_z(\xi, T_1)^2\right) d\xi$

Pressure drop without friction

$P_z(\xi, T_1) := P_i + \frac{G_i(\xi_i)^2}{2 \cdot \rho_f(T_1)} - \frac{G_z(\xi)^2}{2 \cdot \rho_f(T_1)}$

Pressure drop with friction

$Pf_z(\xi, T_1) := P_i + \frac{G_i(\xi_i)^2}{2 \cdot \rho_f(T_1)} - \frac{G_z(\xi)^2}{2 \cdot \rho_f(T_1)} - \Delta P_f(\xi, T_1)$

F.3 Modified Dynamic Flash Inception Line

Modified dynamic inception line code with 0.07 intensity

$$
\begin{aligned}
&CC(n) := \ \text{for } j \in 1..n-1 \\
&\quad \xi_{j+1} \leftarrow \xi_j + 0.5 \\
&\quad A_{j+1} \leftarrow A_x\left(\xi_{j+1}\right) \\
&\quad part_{j+1} \leftarrow \frac{m_T^{\,3}}{\rho_f(T_g)^2 \cdot \left(A_{j+1}\right)^4} \\
&\quad DADZ_{j+1} \leftarrow dAdZ_x\left(\xi_{j+1}\right) \\
&\quad \Sigma_{j+1} \leftarrow \frac{m_T^{\,3}}{\rho_f(T_g)^2 \cdot \left(A_{j+1}\right)^4} \cdot \left(-dAdZ_x\left(\xi_{j+1}\right)\right) \\
&\quad PFi_{j+1} \leftarrow 0.252 \cdot \frac{\sigma(T_g)^{\frac{3}{2}}}{(k \cdot T_{ab})^{0.5}} \cdot \frac{Tr(T_g)^{13.73} \cdot \left[1 + 14 \cdot \left(\frac{\Sigma_{j+1}}{\frac{Matm}{s}}\right)^{0.8}\right]^{0.5}}{\left(1 - \frac{v_f(T_g)}{v_g(T_g)}\right)} - 27(0.07)^2 \left[\frac{\left(\frac{m_T}{A_{j+1}}\right)^2}{2\rho_f(T_g)}\right] \cdot \left(\frac{A_{j+1}}{A0}\right)^{1.4} \\
&\quad PF1_{j+1} \leftarrow 0.252 \cdot \frac{\sigma(T_g)^{\frac{3}{2}}}{(k \cdot T_{ab})^{0.5}} \\
&\quad PF2_{j+1} \leftarrow \frac{Tr(T_g)^{13.73} \cdot \left[1 + 14 \cdot \left(\frac{\Sigma_{j+1}}{\frac{Matm}{s}}\right)^{0.8}\right]^{0.5}}{1 - \frac{v_f(T_g)}{v_g(T_g)}} \cdot \left[0.252 \cdot \frac{\sigma(T_g)^{\frac{3}{2}}}{(k \cdot T_{ab})^{0.5}}\right]
\end{aligned}
$$

$$PF3_{j+1} \leftarrow 27(0.15)^2 \left[\frac{\left(\frac{m_T}{A_{j+1}}\right)^2}{2\rho_f(T_g)}\right] \cdot \left(\frac{A_{j+1}}{A0}\right)^{1.4}$$

$$Y_{j+1,1} \leftarrow \xi_{j+1}$$

$$Y_{j+1,2} \leftarrow \frac{A_{j+1}}{mm^2}$$

$$Y_{j+1,3} \leftarrow \frac{part_{j+1}}{\frac{Pa}{m \cdot s}}$$

$$Y_{j+1,4} \leftarrow \frac{DADZ_{j+1}}{mm}$$

$$Y_{j+1,5} \leftarrow \frac{\Sigma_{j+1}}{\frac{Pa}{s}}$$

$$Y_{j+1,6} \leftarrow \frac{PFi_{j+1}}{Pa \cdot 10^5}$$

$$Y_{j+1,7} \leftarrow \frac{PF1_{j+1}}{Pa \cdot 10^5}$$

$$Y_{j+1,8} \leftarrow \frac{PF2_{j+1}}{Pa \cdot 10^5}$$

$$Y_{j+1,9} \leftarrow \frac{PF3_{j+1}}{Pa \cdot 10^5}$$

Y

Y

F.4 Flash "Cavitation Wave"

Flash inception point calculation for 70 degrees Celsius

$m_{dot} := 0.0304 \cdot \frac{kg}{s}$ $A := 2.746 \cdot mm^2$ $hfg(T) := h_g(T) - h_f(T)$

$$a(\alpha, T_{sat}, P, s_i, T_{abs}, \rho) := \frac{1}{\sqrt{\rho \cdot \left[\left[\frac{\alpha}{\rho a_g(P)} + \frac{(1-\alpha)}{\rho a_f(P)} + \frac{\left[(1-\alpha) \cdot \rho_f(T_{sat}) \cdot T_{abs} \cdot C_{pf}(T_{sat}) \right]}{\left[\left(\rho_g(T_{sat}) \cdot hfg(T_{sat}) \right)^2 \right]} \right] \right]}}$$

$F_1(P, v) :=$

$T_{sat} \leftarrow T_{sat}(P)$

$\rho \leftarrow \frac{1}{v}$

$U \leftarrow \frac{m_{dot}}{\rho \cdot A}$

$\alpha \leftarrow \frac{\rho - \rho_f(T_{sat})}{\rho_g(T_{sat}) - \rho_f(T_{sat})}$

$Q \leftarrow \frac{\rho_g(T_{sat}) \cdot \alpha}{\rho_f(T_{sat}) \cdot (1-\alpha) + \rho_g(T_{sat}) \cdot \alpha}$

$s_i \leftarrow Q \cdot s_g(T_{sat}) + (1-Q) \cdot s_f(T_{sat})$

$T_{abs} \leftarrow T_{sat} + 273.15K$

$a \leftarrow a(\alpha, T_{sat}, P, s_i, T_{abs}, \rho)$

$M \leftarrow \frac{U}{a}$

$\psi \leftarrow \frac{m_{dot}}{A}$

$h \leftarrow Q \cdot h_g(T_{sat}) + (1-Q) \cdot h_f(T_{sat})$

$Y_1 \leftarrow \frac{T_{sat}}{K}$

$Y_2 \leftarrow \frac{\rho}{\frac{kg}{m^3}}$

$Y_3 \leftarrow \frac{U}{\frac{m}{s}}$

$Y_4 \leftarrow \alpha$

$Y_5 \leftarrow Q$

$Y_6 \leftarrow \frac{s_i}{\left(\frac{kJ}{kg \cdot K}\right)}$

$Y_7 \leftarrow \frac{T_{abs}}{K}$

$Y_8 \leftarrow \frac{a}{\frac{m}{s}}$

$Y_9 \leftarrow M$

$Y_{10} \leftarrow \frac{\psi}{\left(\frac{kg}{m^2 \cdot s}\right)}$

$Y_{11} \leftarrow \frac{h}{\left(\frac{kJ}{kg}\right)}$

Y

Downstream of the flash calculation "Cavitation Wave"

Initial values for marching procedure

$\rho := Y_2 \cdot \frac{kg}{m^3}$ $U := Y_3 \cdot \frac{m}{s}$ $\alpha := Y_4$ $Q := Y_5$ $s_i := Y_6 \cdot \left(\frac{kJ}{kg \cdot K}\right)$ $M := Y_9$

$\psi := Y_{10} \cdot \frac{kg}{m^2 \cdot s}$ $T := Y_1 \cdot \Delta°C$ $T_{abs} := Y_7 \cdot (K) = 343.112K$ $\rho_4 := 977.74 \frac{kg}{m^3}$

Marching procedure initial equations

$dPdA(\rho, A, M, U) := \frac{\rho \cdot U^2}{A \cdot (1 - M^2)}$ $dUdA(A, M, U) := \frac{U}{A \cdot (1 - M^2)}$ $\Delta A := 0.25 \cdot mm^2$ $\xi := 4.62$ $\eta := 0.75$

$$a(\alpha_{new}, T_{new}, P_{new}, s_i, T_{abs}, \rho_{new}) := \frac{1}{\sqrt{\rho_{new}\left[\left[\frac{\alpha_{new}}{\rho a_g(P_{new})} + \frac{(1 - \alpha_{new})}{\rho a_f(P_{new})} + \frac{\left[(1 - \alpha_{new}) \cdot \rho_f(T_{new}) \cdot T_{abs} \cdot C_{pf}(T_{new})\right]}{\left[\rho_g(T_{new}) \cdot hfg(T_{new})\right]^2}\right]\right]}}$$

$d(A) := \left(\frac{A}{\frac{\pi}{4}}\right)^{0.5}$ $\mu_{fg}(T_n) := Q \cdot \mu_g(T_n) + (1 - Q) \cdot \mu_f(T_n)$ $Re(T_n, \psi) := \frac{\psi \cdot d(A)}{\mu_{fg}(T_n)}$ $z_i(\xi) := \xi \cdot mm$

$f_{fo}(T_n, \psi, A) := 0.079 \cdot \left[\frac{1}{\left(\frac{\psi \cdot d(A)}{\mu_f(T_n)}\right)^{0.25}}\right]$ $f_{go}(T_n, \psi, A) := 0.079 \cdot \left[\frac{1}{\left(\frac{\psi \cdot d(A)}{\mu_g(T_n)}\right)^{0.25}}\right]$ $\Delta z_i(\xi) := \Delta\xi(\xi, \Delta A) \cdot mm$

$KK(A, As, \eta) := (1 - \eta) \cdot \left[1 - \left(\frac{As}{A}\right)^2\right]$ $ff(A, As, \xi, \eta) := \frac{KK(A, As, \eta) \cdot d(A)}{\Delta z_i(\xi)}$

$dPdZG(T_n, \xi, \psi, A, Q, As) := \frac{2 \cdot ff(A, As, \xi, \eta) \cdot \psi^2 \cdot v_g(T_n) \cdot Q^2}{d(A)}$ $dPdZF(T_n, \xi, \psi, A, Q, As) := \frac{2 \cdot ff(A, As, \xi, \eta) \cdot \psi^2 \cdot v_f(T_n) \cdot (1 - Q)^2}{d(A)}$

$\rho_h(T_n, Q) := \frac{1}{Q \cdot v_g(T_n) + (1 - Q) \cdot v_f(T_n)}$ $XX(T_n, \xi, \psi, A, Q, As) := \left(\frac{dPdZF(T_n, \xi, \psi, A, Q, As)}{dPdZG(T_n, \xi, \psi, A, Q, As)}\right)^{0.5}$

$\Phi_{fo}(T_n, \xi, \psi, A, Q, As) := 1 + \frac{10}{XX(T_n, \xi, \psi, A, Q, As)} + \frac{1}{XX(T_n, \xi, \psi, A, Q, As)^2}$

$\Phi_{go}(T_n, \xi, \psi, A, Q, As) := 1 + 10 \cdot XX(T_n, \xi, \psi, A, Q, As) + XX(T_n, \xi, \psi, A, Q, As)^2$

$P_{drop}(T_n, \xi, \psi, A, Q, As) := \left(\frac{2 \cdot ff(A, As, \xi, \eta) \cdot \psi^2 \cdot v_f(T_n)}{d(A)}\right) \cdot \Phi_{fo}(T_n, \xi, \psi, A, Q, As) \cdot \Delta z_i(\xi)$

$$dPdZ(T_n,\xi,\psi,A,Q,As) := \frac{2\cdot ff(A,As,\xi,\eta)\cdot\psi^2\cdot v_f(T_n)\cdot(1-Q)^2}{d(A)}\cdot\Phi_{fb}(T_n,\xi,\psi,A,Q,As)$$

$$dAd\xi(\xi) := \frac{d}{d\xi}A_z(\xi) \qquad dAdZ(\xi) := dAd\xi(\xi)\cdot mm^{-1} \qquad dPdA_f(T_n,\xi,\psi,A,Q,As) := \frac{dPdZ(T_n,\xi,\psi,A,Q,As)}{dAdZ(\xi)}$$

$$s_{exit}(s_i,T,Q,z_i,\xi) := \frac{P_{drop}(T,\xi,\psi,A,Q,As)\cdot\left[\left(\frac{Q}{\rho_g(T)}\right)+(1-X)\cdot\left(\frac{1}{\rho_f(T)}\right)\right]}{T_{abs}} + s_i$$

Marching procedure initial values

$$A_1 := A \qquad P_1 := P \qquad U_1 := QQ_3\cdot\frac{m}{s} \qquad M_1 := QQ_9 \qquad \rho_1 := QQ_2\cdot\frac{kg}{m^3}$$

$$Q_1 := QQ_5 \qquad T_1 := QQ_1\cdot\Delta°C \qquad ss_1 := QQ_6\cdot\left(\frac{kJ}{kg\cdot K}\right) \qquad \xi_1 := (\xi) \qquad \psi_1 := QQ_{10}\cdot\frac{kg}{m^2\cdot s}$$

Marching procedure

$$F(n) := \text{for } j \in 1..n-1$$

$$A_{j+1} \leftarrow A_j + \Delta A$$

$$\xi_{j+1} \leftarrow \xi_j + \Delta\xi(\xi_j, \Delta A)$$

$$KK_{j+1} \leftarrow (1-\eta)\cdot\left[1-\left(\frac{A_j}{A_{j+1}}\right)^2\right]$$

$$ff_{j+1} \leftarrow \frac{KK_{j+1}\cdot d(A_j)}{\Delta z_i(\xi_{j+1})}$$

$$dPdZ_{j+1} \leftarrow \frac{2\cdot ff_{j+1}\cdot(\psi_j)^2\cdot v_f(T_j)}{d(A_j)}\cdot\Phi_{fo}(T_j, Q_j, \psi_j, A_j)$$

$$dPdAF_{j+1} \leftarrow \frac{dPdZ_{j+1}}{dAdZ(\xi_{j+1})}$$

$$P_{j+1} \leftarrow \left(P_j + dPdA(\rho_j, A_j, M_j, U_j)\cdot\Delta A\right) - \left[\frac{1}{\left[1-(M_j)^2\right]}\right]dPdAF_{j+1}\cdot\Delta A$$

$$T_{j+1} \leftarrow T_{sat}(P_{j+1})$$

$$T_{abs} \leftarrow T_{j+1} + 273K$$

$$ss_{j+1} \leftarrow \frac{P_{drop}(T_j, \xi_j, \psi_j, A_{j+1}, Q_j, A_j)\cdot\left[\left(\frac{Q_j}{\rho_g(T_j)}\right)+(1-Q_j)\cdot\left(\frac{1}{\rho_f(T_j)}\right)\right]}{T_{abs}} + ss_j$$

$$Q_{j+1} \leftarrow \frac{ss_{j+1} - s_f(T_{j+1})}{s_g(T_{j+1}) - s_f(T_{j+1})}$$

$$\alpha_{j+1} \leftarrow \frac{\rho_f(T_{j+1})\cdot Q_{j+1}}{\rho_g(T_{j+1})\cdot(1-Q_{j+1}) + \rho_f(T_{j+1})\cdot Q_{j+1}}$$

$$\rho_{j+1} \leftarrow \rho_f(T_{j+1})\cdot(1-\alpha_{j+1}) + \rho_g(T_{j+1})\cdot\alpha_{j+1}$$

$$a_{j+1} \leftarrow \frac{1}{\sqrt{\rho_{j+1}\left[\left[\frac{\alpha_{j+1}}{\rho a_g\left(P_{j+1}\right)}+\frac{\left(1-\alpha_{j+1}\right)}{\rho a_f\left(P_{j+1}\right)}+\frac{\left[\left(1-\alpha_{j+1}\right)\cdot\rho_f\left(T_{j+1}\right)\cdot T_{abs}\cdot C_{pf}\left(T_{j+1}\right)\right]}{\left[\left(\rho_g\left(T_{j+1}\right)\cdot hfg\left(T_{j+1}\right)\right)^2\right]}\right]\right]}}$$

$$U_{j+1} \leftarrow \frac{m_{dot}}{\rho_{j+1}\cdot A_{j+1}}$$

$$M_{j+1} \leftarrow \frac{U_{j+1}}{a_{j+1}}$$

$$\psi_{j+1} \leftarrow \frac{m_{dot}}{A_{j+1}}$$

$$h_{j+1} \leftarrow Q_{j+1}\cdot h_g\left(T_{j+1}\right)+\left(1-Q_{j+1}\right)\cdot h_f\left(T_{j+1}\right)$$

$$\Phi_{j+1} \leftarrow A_1\left(T_j, Q_j, \psi_j, A_j\right)+\frac{3.24\cdot A_2\left(Q_j\right)\cdot A_3\left(T_j\right)}{Fr\left(T_j, \psi_j, A_j, Q_j\right)^{0.045}\cdot We\left(T_j, \psi_j, A_j, Q_j\right)^{0.035}}$$

$$U4_{j+1} \leftarrow \frac{m_{dot}}{\rho_4\cdot A_{j+1}}$$

$$p4_{j+1} \leftarrow P_{j+1}+\rho_{j+1}\cdot\left(U_{j+1}\right)^2-\rho_4\cdot\left(U4_{j+1}\right)^2$$

$$SP_{j+1} \leftarrow \frac{2\cdot ff_{j+1}\cdot\left(\psi_j\right)^2\cdot v_f\left(T_j\right)}{d\left(A_j\right)}$$

$$SPZ_{j+1} \leftarrow \frac{2\cdot ff_{j+1}\cdot\left(\psi_j\right)^2\cdot v_f\left(T_j\right)\cdot\Delta z_i\left(\xi_j\right)}{d\left(A_j\right)}$$

$$Y_{j,1} \leftarrow \frac{A_{j+1}}{mm^2}$$

$$Y_{j,2} \leftarrow \xi_{j+1}$$

$$Y_{j,3} \leftarrow KK_{j+1}$$

$$Y_{j,4} \leftarrow ff_{j+1}$$

$$Y_{j,5} \leftarrow \frac{dPdZ_{j+1}}{\frac{kPa}{m}}$$

$$Y_{j,6} \leftarrow \frac{dPdAF_{j+1}}{\frac{kPa}{m^2}}$$

$$Y_{j,7} \leftarrow \frac{P_{j+1}}{kPa}$$

$$Y_{j,8} \leftarrow \frac{T_{j+1}}{K}$$

$$Y_{j,9} \leftarrow \frac{T_{abs}}{K}$$

$$Y_{j,10} \leftarrow \frac{ss_{j+1}}{\frac{kJ}{kg\cdot K}}$$

$$Y_{j,11} \leftarrow Q_{j+1}$$

$$Y_{j,12} \leftarrow \alpha_{j+1}$$

$$Y_{j,13} \leftarrow \frac{\rho_{j+1}}{\frac{kg}{m^3}}$$

$$Y_{j,14} \leftarrow \frac{a_{j+1}}{\frac{m}{s}}$$

$$Y_{j,15} \leftarrow \frac{U_{j+1}}{\frac{m}{s}}$$

$$Y_{j,16} \leftarrow M_{j+1}$$

$$Y_{j,17} \leftarrow \frac{\psi_{j+1}}{\frac{kg}{m^2\cdot s}}$$

$$Y_{j,18} \leftarrow \frac{h_{j+1}}{\frac{kJ}{kg}}$$

$$Y_{j,19} \leftarrow \Phi_{j+1}$$

$$Y_{j,20} \leftarrow \frac{U4_{j+1}}{\frac{m}{s}}$$

$$Y_{j,21} \leftarrow \frac{p4_{j+1}}{kPa}$$

$$Y_{j,22} \leftarrow \frac{SP_{j+1}}{\frac{kPa}{mm}}$$

$$\left(Y_{j,23} \leftarrow \frac{SPZ_{j+1}}{kPa}\right)$$

$$Y$$

F.5 Condensation Shock

Condensation shock backward calculation

Initial values for marching procedure

$m_{dot} := 0.0306 \cdot \frac{kg}{s}$ $A_1 := 63.62 \cdot mm^2$ $P_1 := 67 kPa$ $G_1 := \frac{m_{dot}}{A_1}$ $\xi_1 := 58.75$ $T_1 := 70K$

$v := v_f\left(T_{sat}\left(P_1\right)\right) = 1.035 \times 10^{-3} \frac{m^3}{kg}$ $\rho := 977 \frac{kg}{m^3}$ $T_{sat}\left(P_1\right) = 88.78K$ $\Delta A := 0.1 mm^2$ $\eta := 0.75$

$D_1 := 9mm$ $\rho_f\left(T_1\right) = 977.73 \frac{kg}{m^3}$

$V_1 := \frac{m_{dot}}{A_1 \cdot \rho_f\left(T_1\right)} = 0.492 \frac{m}{s}$ $\mu_f\left(T_1\right) = 4.039 \times 10^{-4} \frac{kg}{s \cdot m}$ $A_s := 63.62 \cdot mm^2 + (\Delta A)$

$Re_1 := \frac{\rho_f\left(T_1\right) \cdot V_1 \cdot D_1}{\mu_f\left(T_1\right)}$ $\mu := 4.037 \times 10^{-4} \frac{kg}{m \cdot s}$ $\Delta z_i(\xi) := \Delta\xi(\xi, \Delta A) \cdot mm$ $z_i(\xi) := \xi \cdot mm$

$KK_1 := (1 - \eta) \cdot \left[1 - \left(\frac{A_1}{A_s}\right)^2\right]$ $f_1 := \frac{KK_1 \cdot D_1}{\Delta z_i\left(\xi_1\right)}$ $\Delta A = 0.1 \cdot mm^2$

$\Delta Pf_1 := \frac{1}{2}\left(\frac{f_1}{D_1}\right) \cdot \left[\rho_f\left(T_1\right) \cdot \left(V_1\right)^2\right] \cdot \Delta z_i\left(\xi_1\right) = 9.276 \times 10^{-5} \cdot kPa$

Marching procedure

$$
\begin{aligned}
&F(m_{dot}, \rho, \mu, A_s) := \\
&\quad \text{for } j \in 1..n-1 \\
&\quad\quad A_{j+1} \leftarrow A_j - (\Delta A) \\
&\quad\quad D_{j+1} \leftarrow \left(\frac{4 \cdot A_{j+1}}{\pi}\right)^{0.5} \\
&\quad\quad \xi_{j+1} \leftarrow \xi_j - \Delta\xi\left(\xi_j, \Delta A\right) \\
&\quad\quad V_{j+1} \leftarrow \frac{m_{dot}}{A_{j+1} \cdot \rho} \\
&\quad\quad KK_{j+1} \leftarrow (1-\eta) \cdot \left[1 - \left(\frac{A_{j+1}}{A_j}\right)^2\right] \\
&\quad\quad f_{j+1} \leftarrow \frac{KK_{j+1} \cdot D_{j+1}}{\Delta z_i(\xi_1)} \\
&\quad\quad G_{j+1} \leftarrow \frac{m_{dot}}{A_{j+1}} \\
&\quad\quad \Delta Pf_{j+1} \leftarrow \frac{1}{2}\left(\frac{f_{j+1}}{D_{j+1}}\right) \cdot \left[\rho \cdot \left(V_{j+1}\right)^2\right] \cdot \Delta z_i\left(\xi_{j+1}\right) \\
&\quad\quad P_{j+1} \leftarrow P_j + \frac{\left(G_j\right)^2 - \left[\left(G_{j+1}\right)^2\right]}{2 \cdot \rho} - \Delta Pf_{j+1} \\
&\quad\quad T_{j+1} \leftarrow T_{sat}\left(P_{j+1}\right) \\
&\quad\quad Y_{j+1,1} \leftarrow \frac{A_{j+1}}{mm^2} \\
&\quad\quad Y_{j+1,2} \leftarrow \frac{D_{j+1}}{mm} \\
&\quad\quad Y_{j+1,3} \leftarrow \xi_{j+1} \\
&\quad\quad Y_{j+1,4} \leftarrow \frac{V_{j+1}}{\frac{m}{s}} \\
&\quad\quad Y_{j+1,5} \leftarrow KK_{j+1} \\
&\quad\quad Y_{j+1,6} \leftarrow f_{j+1} \\
&\quad\quad Y_{j+1,7} \leftarrow \frac{G_{j+1}}{\frac{kg}{cm^2 \cdot s}} \\
&\quad\quad Y_{j+1,8} \leftarrow \frac{\Delta Pf_{j+1}}{kPa} \\
&\quad\quad Y_{j+1,9} \leftarrow \frac{P_{j+1}}{kPa} \\
&\quad\quad Y_{j+1,10} \leftarrow \frac{T_{j+1}}{K} \\
&\quad Y
\end{aligned}
$$

Appendix G - Water Saturation Table

Temp	Temp	Pressure	volume (m^3/kg)		volume (m^3/mol)		volume Ratio		density Ratio		Pr	Tr
°C	K	Pa	vf	vg	vf	vg	Vf/Vc	Vg/Vc	ρf/ρc	ρg/ρc	P/Pc	T/Tc
150	423.15	4.76E+05	0.0010905	0.3928	1.97E-05	7.08E-03	0.351	126.397	2.850	0.008	0.02	0.653715
160	433.15	6.18E+05	0.001102	0.3071	1.99E-05	5.53E-03	0.355	98.820	2.820	0.010	0.03	0.669164
170	443.15	7.92E+05	0.0011143	0.2428	2.01E-05	4.38E-03	0.359	78.130	2.789	0.013	0.04	0.684613
180	453.15	1.00E+06	0.0011274	0.1941	2.03E-05	3.50E-03	0.363	62.459	2.756	0.016	0.05	0.700062
190	463.15	1.25E+06	0.0011415	0.1565	2.06E-05	2.82E-03	0.367	50.359	2.722	0.020	0.06	0.715511
200	473.15	1.55E+06	0.0011565	0.1274	2.08E-05	2.30E-03	0.372	40.996	2.687	0.024	0.07	0.730959
210	483.15	1.91E+06	0.0011726	0.1044	2.11E-05	1.88E-03	0.377	33.594	2.650	0.030	0.09	0.746408
220	493.15	2.32E+06	0.00119	0.08619	2.14E-05	1.55E-03	0.383	27.735	2.611	0.036	0.10	0.761857
230	503.15	2.80E+06	0.0012088	0.07158	2.18E-05	1.29E-03	0.389	23.033	2.571	0.043	0.13	0.777306
240	513.15	3.34E+06	0.0012291	0.05976	2.21E-05	1.08E-03	0.396	19.230	2.528	0.052	0.15	0.792755
250	523.15	3.97E+06	0.0012512	0.05013	2.25E-05	9.03E-04	0.403	16.131	2.484	0.062	0.18	0.808203
260	533.15	4.69E+06	0.0012755	0.04221	2.30E-05	7.61E-04	0.410	13.583	2.436	0.074	0.21	0.823652
270	543.15	5.50E+06	0.0013023	0.03564	2.35E-05	6.42E-04	0.419	11.468	2.386	0.087	0.25	0.839101
280	553.15	6.41E+06	0.0013321	0.03017	2.40E-05	5.44E-04	0.429	9.708	2.333	0.103	0.29	0.85455
290	563.15	7.44E+06	0.0013656	0.02557	2.46E-05	4.61E-04	0.439	8.228	2.276	0.122	0.34	0.869998
300	573.15	8.58E+06	0.0014036	0.02167	2.53E-05	3.90E-04	0.452	6.973	2.214	0.143	0.39	0.885447
310	583.15	9.86E+06	0.001448	0.01834	2.61E-05	3.30E-04	0.466	5.900	2.146	0.169	0.45	0.900896
320	593.15	1.13E+07	0.001499	0.01549	2.70E-05	2.79E-04	0.482	4.984	2.073	0.201	0.51	0.916345
330	603.15	1.29E+07	0.001561	0.01298	2.81E-05	2.34E-04	0.502	4.176	1.991	0.239	0.58	0.931794
340	613.15	1.46E+07	0.001638	0.01080	2.95E-05	1.95E-04	0.527	3.475	1.897	0.288	0.66	0.947242
350	623.15	1.65E+07	0.001740	0.008802	3.14E-05	1.59E-04	0.560	2.832	1.786	0.353	0.75	0.962691
360	633.15	1.87E+07	0.001893	0.006945	3.41E-05	1.25E-04	0.609	2.235	1.642	0.447	0.84	0.97814
370	643.15	2.10E+07	0.002215	0.004954	3.99E-05	8.93E-05	0.713	1.594	1.403	0.627	0.95	0.993589
374.14	647.29	2.21E+07	0.003155	0.003155	5.69E-05	5.69E-05	1.015	1.015	0.985	0.985	1.00	0.999985

Tables imported from Refprop which is published by NIST, the program uses thermodynamics equations to solve for the saturation properties of a fluid. Tables were then modified by adding volume and density ratios. [31]